Jet Modification in Strongly Coupled Quark-Gluon Plasma

Chanwook Park

Department of Physics

McGill University, Montréal

June, 2020

A thesis submitted to McGill University in partial fulfillment of the requirements of the degree of Doctor of Philosophy

Table of Contents

List of Figures

List of Tables

Abstract

A deconfined plasma of quarks and gluons, known as quark-gluon plasma (QGP), is produced in relativistic heavy-ion collisions. This new state of strongly coupled matter is characterized by collective behaviour and may provide an opportunity to study Quantum Chromodynamics (QCD) under extreme temperatures and densities. One of the most remarkable experimental signatures of QGP formation is the suppression of high transverse momentum (p_T) jets created in initial inelastic scattering with high momentum transfer. Measurements have demonstrated that high p_T jet production in heavy-ion collisions is strongly suppressed when compared to proton-proton collisions. Interestingly, experiments of proton-lead collisions have discovered a signal of collectivity comparable to that in lead-lead collisions while no significant suppression of jet yield was observed.

This thesis presents the study of jet modification in large (Pb+Pb) and small (p+Pb) colliding systems using MARTINI, a sophisticated Monte-Carlo event generator for jet evolution in heavy-ion collisions. MARTINI incorporates the AMY radiative energy loss formalism and the leading-order elastic collisional energy loss formulations. Realistic simulations at the LHC energy scales are aided by new developments in MARTINI, including the QCD running coupling, a formation time of radiation, and a thermal recoil implementation.

We demonstrate that the QCD running coupling and the formation time of radiation capture the characteristics of jet quenching at the LHC energy scales. The importance of thermal recoil in describing integrated and differential jet observables is investigated. We obtain a simultaneous description of the jet nuclear modification factor R_{pPb} and the

elliptic flow coefficients for high-energy jets in p+Pb collisions using the jet quenching model within the uncertainties. This study provides a comprehensive understanding of jet quenching in heavy-ion collisions and shows an indication of quark-gluon plasma in small systems.

Résumé

Un plasma déconfiné de quarks et de gluons, appelé plasma quark-gluon (QGP), est produit lors de collisions d'ions lourds relativistes. Ce nouvel état de matière fortement couplée est caractérise par un comportement collectif et peut fournir une occasion d'étudier la chromodynamique quantique (QCD) sous des températures et des densités extrêmes. L'une des signatures expérimentales les plus remarquables de la formation de QGP est la suppression des jets à impulsion transversale élevée (p_T), créés lors de la diffusion inélastique initiale avec un transfert d'impulsion élevé. Les mesures ont démontré que la production élevée de jets de p_T dans les collisions d'ions lourds est fortement supprimée par rapport aux collisions proton-proton. Fait intéressant, des expériences de collisions proton-plomb ont découvert un signal de collectivité comparable à celui des collisions plomb-plomb, alors qu'aucune suppression significative du rendement du jet n'a été observée.

Cette thèse présente l'étude de la modification des jets dans les grands systémes (Pb+Pb) et les petits (p+Pb) en collision à l'aide de MARTINI, un générateur d'événements Monte-Carlo sophistiqué pour l'évolution des jets dans les collisions d'ions lourds. MARTINI incorpore le formalisme de perte d'énergie radiative AMY et les formulations de perte d'énergie collisionnelle élastique de premier ordre. Les simulations réalistes aux échelles énergétiques du LHC sont facilitées par les nouveaux développements de MARTINI, y compris le couplage de course QCD, un temps de formation de rayonnement et une implémentation de recul thermique.

Nous démontrons que le couplage courant QCD et le temps de formation du rayonnement capturent les caractéristiques de la trempe au jet aux échelles d'énergie du LHC. On étudie l'importance du recul thermique dans la description des observables à jet intégrés et différentiels. Nous obtenons une description simultanée du facteur de modification nucléaire du jet R_{pPb} et des coefficients de flux elliptique pour les jets à haute énergie dans les collisions p+Pb en utilisant le modèle de trempe au jet dans les incertitudes. Cette étude fournit une compréhension complète de la trempe au jet dans les collisions d'ions lourds et montre une indication du plasma quark-gluon dans les petits systèmes.

Acknowledgements

I would like to express a deep sense of gratitude to my supervisor, Professor Sangyong Jeon, who has consistently and patiently guided me throughout the four-and-a-half years of my Ph.D. study. Sangyong has dedicated his time for valuable advice and countless discussions on my research and provided me with opportunities to attend conferences, workshops, and summer schools for my education. His support and encouragement have made it possible to complete this thesis.

I am highly indebted to Professor Charles Gale for the enlightening advice and positive feedback he has generously offered. As a physicist, his deep insight and wisdom have inspired me in many ways. I have had the great pleasure of working with him during my graduate studies at McGill.

My doctoral research was significantly influenced by substantial help from Professor Chun Shen, who was a former Postdoc at McGill. The majority of the jet quenching study on small systems has been accomplished in close collaboration with him over the years. I would also like to thank my collaborators and my office mates, Scott McDonald and Mayank Singh, for providing me with various input for my analysis and sharing interesting suggestions and comments on my research. I appreciate and acknowledge Dr. Björn Schenke, who has developed MARTINI, for his assistance in utilizing MARTINI in my analysis.

I take this opportunity to thank my colleagues in the Theoretical Nuclear Physics Group at McGill, Dr. Shuzhe Shi, Sigtryggur Hauksson, Jessica Churchill, Matthew Heffernan, Rouz Modarresi-Yazdi, and Melissa Mendes for numerous discussions and con-

versations from which I was able to enjoy my graduate life. I wish to especially thank Matthew Heffernan for proofreading this thesis. I would also thank the former group members at McGill, Dr. Jean-François Paquet, Dr. Gojko Vujanovic, Dr. Sangwook Ryu, and Dr. Daniel Pablos for enlightening discussions on my research.

As a member of the JETSCAPE collaboration, I would like to extend my special note of thanks to Professor Abhijit Majumder, who is the spokesperson of JETSCAPE and kindly allowed me to collaborate with many brilliant physicists. Especially I am grateful to my colleagues in JETSCAPE, Dr. Shanshan Cao, Dr. Yasuki Tachibana, Amit Kumar, and Chathuranga Sirimanna who have worked closely with me for various major projects in JETSCAPE.

Statement of originality

The research presented in this thesis contains an original contribution to knowledge in the field of heavy-ion physics. The originality of my research is represented by i) the systematic study of jet quenching in Pb+Pb collisions using the MARTINI framework, and ii) the investigation of the signature of quark-gluon plasma in small systems using the jet quenching mechanism.

Sec. 5.1 presents a description of the MARTINI framework, developed by Björn Schenke, Charles Gale, and Sangyong Jeon [1]. The formation time in the AMY radiative energy loss formalism shown in Sec. 5.2.1 was implemented by my supervisor, Sanyong Jeon, and demonstrated by myself. Sec. 5.3 describes my original work to improve the MARTINI framework, including the QCD running coupling scheme and the implementation of thermal recoils. The idea of estimating the renormalization scale μ_R for radiative processes is taken from the work by Clint Young, Björn Schenke, Sangyong Jeon, and Charles Gale [2].

The main results presented in Ch. 6 and Ch. 7 are my original work. The groundwork for the research includes constraining the parameters in PYTHIA and our quenching models to fit the results to data. The initial energy density profiles for Pb+Pb and p+Pb collisions shown in Sec. 6.1 and Sec. 7.2 were obtained by Scott McDonald based on [3]. The hydrodynamic simulations were performed by Mayank Singh for Pb+Pb and Chun Shen [4] for p+Pb collisions to produce the QGP evolution profiles. Using these inputs, I performed the MARTINI simulations for jet evolution with the quenching models to produce the results presented in Ch. 6 and Ch. 7 and deliver the conclusion of this study.

Dedicated to my parents.

Part I

Overview of heavy-ion collisions

Chapter 1

Introduction

The first few microseconds of the Universe were too hot and dense to allow strongly interacting quarks and gluons to form hadronic matter. Until 1 μs after the Big Bang, it took the form of a thermalized plasma of quarks, gluons, and leptons without structure - a quark-gluon plasma (QGP). After this short period of the violently expanding QGP, the Universe progressed through different epochs from the formation of nuclear matter to primordial nucleosynthesis to stars and galaxies [5–11]. The current knowledge of the deconfined phase of matter is described by Quantum Chromodynamics (QCD), the quantum field theory describing the interaction among the quarks and gluons. Colour confinement, a unique phenomenon of QCD stating that quarks and gluons have to be confined within a bound state, explains why free quarks and gluons have never been observed outside of ordinary matter such as protons and neutrons. Meanwhile, asymptotic freedom, the interaction between quarks and gluons weakens at a higher energy scale, predicts the deconfined phase of QCD matter at very high temperatures or densities. QCD solved on the lattice estimated that the condition for a QCD phase transition is a temperature of $T_c \sim 100$ MeV or an energy density of $\epsilon \sim 1$ GeV/fm^3 [12–15]. In units in daily life, these values are about 10^{12} K and 10^{15} g/cm^3, which are 10^5 times hotter than the core of the sun and 10^{15} times denser than the earth.

An ideal way to achieve such extreme conditions in the laboratory is to accelerate heavy nuclei to as high energies as possible and collide them. Relativistic collisions of heavy nuclei (ions) compress and heat the nucleons, allowing the colliding zone to reach the conditions of the QCD phase transition. In the year 2005, the Relativistic Heavy Ion Collider (RHIC) at Brookhaven National Laboratory (BNL) announced a long-awaited discovery of a QGP from relativistic Au+Au collisions [16–19]. The fireball created in the laboratory rapidly expanded and cooled to the temperature of the QCD phase transition, allowing protons and neutrons (and unstable hadrons to decay into lighter species) to form. Despite the much smaller size and lower energy scale of the QGP created in heavy-ion collisions as compared to that after the Big Bang, it was sufficient to recreate the evolution of the Early Universe crossing the QCD phase boundary.

In the past 20 years, heavy-ion programs at the RHIC at BNL or the Large Hadron Collider (LHC) at CERN have produced an immense volume of data by which the properties of a QGP is characterized. One of the astonishing observations from experiments is the strongly-interacting properties of the QGP, contrasting with the predicted view of a weakly-coupled ideal gas based on the idea of asymptotic freedom. The fireball expands hydrodynamically with small viscosity, rapidly reaching thermal equilibrium. The large anisotropy coefficients measured in experiments confirm the collective motion of a strongly-interacting QGP.

Modification of any coloured objects traversing the fireball is an ineluctable consequence of the strongly coupled property of the QGP. This property, commonly referred to as colour opacity, is another important experimental signature of a deconfined QCD matter created in heavy-ion collisions. In high-energy collisions of two nucleons, hard scattering events, involving high momentum exchange, between constituent partons (quarks and gluons) create a pair of fast-moving partons. Jet are characteristics of parton showers initiated from hard scatterings. Since hard scatterings occur at the very early stage of the collisions, jets are ideal candidates to probe the strongly-interacting QCD matter. The substantial suppression of high energy hadron production in heavy-ion collisions com-

pared with that in proton-proton collisions observed in experiments is clear evidence of deconfinement.

In this dissertation, I focus on the phenomenon of jet quenching in Pb+Pb and p+Pb colliding systems. The main purposes of this dissertation are

- to provide theoretical descriptions to characterize jet modification in heavy-ion collisions, and
- to address collective behaviour observed in small systems (p+Pb collisions) and explore a signature of a QGP in the system using hard probes.

Ch. 2 provides a general description of Quantum Chromodynamics, the cornerstone of the field of heavy-ion collisions. In Ch. 3, jet production in inelastic scattering processes, including the parton model and the DGLAP equations, is discussed. Ch. 4 covers a phenomenological review of heavy-ion collisions and the evolution of a QGP. Two distinct aspects that characterize the deconfined state of matter created in a laboratory are also discussed in detail. To conduct this research, I utilized a Monte-Carlo event generator for heavy-ion collisions, MARTINI, with advanced features for realistic simulations. The full model descriptions and improvements upon previous work are provided in Ch. 5. Ch. 6 presents the comprehensive analysis of jet quenching in Pb+Pb collisions and theory-model comparisons. The importance of medium response in investigating jet-substructure modification is highlighted. Ch. 7 explores a signature of QGP creation in small colliding systems (p+Pb) by quantifying the influences of cold nuclear matter (CNM) and the hot QGP effect. Finally, Ch. 8 summarizes the results presented in this thesis and discusses the implications of collectivity in heavy-ion collisions.

In this thesis, we adopt a unit system in which $\hbar = c = k_B = 1$. The temporal and spatial scales are expressed in units of fermi (1 fm = 10^{-15} m), while the units of energies and momenta are 1 GeV ($= 10^9$ eV) or 1 TeV ($= 10^{12}$ eV). The metric tensor is taken to be $g_{\mu\nu} = \text{diag}(+1, -1, -1, -1)$ in Cartesian coordinates. Jets in this research refer to as a collimated shower of particles, either partons or hadrons, that are created by initial

hard scatterings in relativistic particle collisions. However, a reconstructed jet that will be discussed in Ch. 5.3.2, Ch. 6 and Ch. 7 denotes a clustered object of hadrons that originate from the parton jet. The reconstructed jet is a proxy for the primary jet parton and is therefore widely used for jet studies in the heavy-ion community.

Chapter 2

Hot QCD matter under extreme conditions

Quantum Chromodynamics (QCD) is the accepted theory of the strong interactions between quarks and gluons. Its complex properties have made quantitative estimations for QCD matter notoriously difficult. Nevertheless, it allows us to make predictions about the QCD phase transition at extreme conditions. Owing to this pioneering prediction, the relativistic high-energy collision program has been intensely pursued and successfully created the new state of deconfined QCD matter.

This chapter is outlined as follows. Sec. 2.1 introduces the Lagrangian of QCD and its unique properties, including asymptotic freedom and colour confinement. In Sec. 2.2, the phase diagram for QCD matter and the characteristics of the phase space relevant to the high-energy collision experiments are discussed. Sec. 2.3 contains a brief discussion of the thermodynamic properties of an ideal gas of deconfined QCD matter followed by typical examples of numerical estimations. Sec. 2.4 summarizes this chapter.

2.1 Quantum chromodynamics

In the Standard Model, Quantum Chromodynamics (QCD) is the theory of strong interaction between elementary constituents of matter, quarks and gluons, that form hadrons (mesons and baryons). The strong interaction is extremely short-ranged and its strength is ~ 100 times stronger than that of the electromagnetic interaction. QCD is the non-Abelian quantum field theory of the $SU(3)$ symmetry group. This encodes that quarks, carrying one of 3 types of colours, form a fundamental representation of $SU(3)$ while their interaction is mediated through gluons, the adjoint representation. The non-Abelian nature of QCD allows gluons i) to carry their own colour charge, i.e., a pair of colour and anti-colour charge, and ii) to have three- and four-gluon self-interactions. These unique features distinguish QCD from other theories of fundamental interactions, e.g., Quantum Electrodynamics (QED).

Let us consider the QCD Lagrangian[1]

$$\mathcal{L}_{QCD} = \bar{\psi}(i\not{D} - m_q)\psi - \frac{1}{2}\,\mathrm{tr}[G^{\mu\nu}G_{\mu\nu}]. \tag{2.1}$$

The quark fields $\psi = \psi_{\alpha,f,i}(x)$ are Dirac spinors with four components $\alpha = 1, \cdots, 4$ and the six flavour states labelled as $f = 1, \cdots, N_f$. The additional index i denotes the three types of quark colour. Since quarks were proposed independently by Gell-Mann and Zweig [20–22], a number of high-energy experiments have discovered six flavors of the quarks: up (u), down (d), charm (c), strange (s), top (t), and bottom (b). The quark field transforms under the fundamental representation of the colour group $SU(3)$,

$$\psi \to \psi'(x) = U\psi(x), \tag{2.2}$$

[1]We use the Einstein summation convention for the flavour index f, $\sum_f \bar{\psi}_f(i\not{D} - m_q)\psi_f$.

where U is a 3×3 unitary matrix acting on the colour index, i. With Einstein summation over a, the matrix U can be represented as

$$U \equiv U(x) = e^{i\theta^a(x)t_a}, \tag{2.3}$$

where $\theta^a(x)$ is the local gauge transformation parameter that can be chosen arbitrarily. The colour group generator $t_a = \lambda_a/2$ has a colour index in the adjoint representation of $SU(3)$ from 1 to 8, corresponding to eight gluon fields $A^a_\mu(x)$. The explicit forms of the eight Gell-Mann matrices λ_a are

$$\begin{aligned}
\lambda_1 &= \begin{pmatrix} 0 & 1 & 0 \\ 1 & 0 & 0 \\ 0 & 0 & 0 \end{pmatrix} \quad \lambda_2 = \begin{pmatrix} 0 & -i & 0 \\ i & 0 & 0 \\ 0 & 0 & 0 \end{pmatrix} \quad \lambda_3 = \begin{pmatrix} 1 & 0 & 0 \\ 0 & -1 & 0 \\ 0 & 0 & 0 \end{pmatrix} \\
\lambda_4 &= \begin{pmatrix} 0 & 0 & 1 \\ 0 & 0 & 0 \\ 1 & 0 & 0 \end{pmatrix} \quad \lambda_5 = \begin{pmatrix} 0 & 0 & -i \\ 0 & 0 & 0 \\ i & 0 & 0 \end{pmatrix} \quad \lambda_6 = \begin{pmatrix} 0 & 0 & 0 \\ 0 & 0 & 1 \\ 0 & 1 & 0 \end{pmatrix} \\
\lambda_7 &= \begin{pmatrix} 0 & 0 & 0 \\ 0 & 0 & -i \\ 0 & i & 0 \end{pmatrix} \quad \lambda_8 = \frac{1}{\sqrt{3}} \begin{pmatrix} 1 & 0 & 0 \\ 0 & 1 & 0 \\ 0 & 0 & -2 \end{pmatrix}.
\end{aligned} \tag{2.4}$$

The covariant derivative D_μ, defined as

$$D_\mu = \partial_\mu - igA_\mu, \tag{2.5}$$

where g is the strong coupling constant $g = \sqrt{4\pi\alpha_s}$ and $A_\mu = A^a_\mu(x)t_a$, is introduced to ensure gauge invariance of the QCD Lagrangian under the local gauge transformation of $SU(3)$. With the covariant derivative D_μ, the gluon fields transform according to

$$A_\mu \to A'_\mu = U\left(A_\mu - \frac{i}{g}U^\dagger \partial_\mu U\right)U^\dagger. \tag{2.6}$$

The gluon kinetic term in Eq. (2.1) is represented by the gluon field strength tensor $G_{\mu\nu}$, defined as

$$G_{\mu\nu}(x) = \frac{i}{g}[D_\mu, D_\nu] = \partial_\mu A_\nu - \partial_\nu A_\mu - ig[A_\mu, A_\nu], \tag{2.7}$$

with colour component $G^a_{\mu\nu}$

$$\begin{aligned} G_{\mu\nu} = G^a_{\mu\nu} t_a &= \partial_\mu A^a_\nu t_a - \partial_\nu A^a_\mu t_a - ig A^a_\mu A^b_\nu [t_a, t_b] \\ &= (\partial_\mu A^a_\nu - \partial_\nu A^a_\mu + g f^{abc} A_{\mu,b} A_{\nu,c}) t_a \end{aligned} \tag{2.8}$$

In the last relation, we have used $[t_a, t_b] = i f_{abc} t^c$, where f_{abc} is the totally anti-symmetric group structure constant of $SU(3)$. The non-Abelian property of QCD originates from the non-vanishing structure constant f_{abc}. Apart from the standard partial derivative terms in Eq. (2.8), there is an additional term containing f_{abc}, which vanishes in QED but survives in QCD. This term induces gluon self-interactions, making QCD more complex than QED. A gluon mass term $m_g^2 A^a_\mu A^\mu_a$ is forbidden by gauge invariance in QCD, which constrains gluons to be massless.

Although the contraction of the two gluon field strength tensors is not gauge-invariant under the transformation $G_{\mu\nu} \to G'_{\mu\nu} = U G_{\mu\nu} U^\dagger$, the cyclic property of the trace operator cancels U in the trace, ensuring the second term in Eq. (2.1) to be gauge invariant,

$$\mathrm{tr}[G_{\mu\nu} G^{\mu\nu}] \to \mathrm{tr}\big[G'_{\mu\nu} G'^{\mu\nu}\big] = \mathrm{tr}\big[U G_{\mu\nu} U^\dagger U G^{\mu\nu} U^\dagger\big] = \mathrm{tr}[G_{\mu\nu} G^{\mu\nu}]. \tag{2.9}$$

Using the identity of the colour group generator, $\mathrm{tr}\big[t^a t^b\big] = \frac{1}{2}\delta^{ab}$, this term can be rewritten as

$$-\frac{1}{2}\,\mathrm{tr}[G_{\mu\nu} G^{\mu\nu}] = -\frac{1}{2}\,\mathrm{tr}\big[G^a_{\mu\nu} t_a G^{\mu\nu}_b t^b\big] = -\frac{1}{2} G^a_{\mu\nu} G^{\mu\nu}_b\,\mathrm{tr}\big[t_a t^b\big] = -\frac{1}{4} G^a_{\mu\nu} G^{\mu\nu}_a, \tag{2.10}$$

that can be further expanded using Eq. (2.8):

$$\begin{aligned}
-\frac{1}{4}G^a_{\mu\nu}G^{\mu\nu}_a =& -\frac{1}{4}(\partial_\mu A^a_\nu - \partial_\nu A^a_\mu + g f_{abc} A^b_\mu A^c_\nu) \\
& \times (\partial^\mu A^\nu_a - \partial^\nu A^\mu_a + g f^{abc} A^\mu_b A^\nu_c) \\
=& -\frac{1}{4}(\partial_\mu A^a_\nu - \partial_\nu A^a_\mu)(\partial^\mu A^\nu_a - \partial^\nu A^\mu_a) \\
& -\frac{1}{2}g(\partial_\mu A^a_\nu - \partial_\nu A^a_\mu) f^{abc} A^\mu_b A^\nu_c \\
& -\frac{1}{4}g^2 f_{abc} A^b_\mu A^c_\nu f^{ade} A^\mu_d A^\nu_e .
\end{aligned} \tag{2.11}$$

Inserting Eq. (2.11) and Eq. (2.5) into Eq. (2.1), we obtain the expanded expression of the QCD Lagrangian[2]

$$\mathcal{L}_{QCD} = \bar{\psi}(i\not{D} - m_q)\psi - \frac{1}{4}G^a_{\mu\nu}G^{\mu\nu}_a \tag{2.12}$$

$$\begin{aligned}
=& \bar{\psi}(i\not{\partial} - m_q)\psi - g\psi\gamma^\mu A^a_\mu t_a \psi - \frac{1}{4}(\partial_\mu A^a_\nu - \partial_\nu A^a_\mu)(\partial^\mu A^\nu_a - \partial^\nu A^\mu_a) \\
& -\frac{1}{2}g(\partial_\mu A^a_\nu - \partial_\nu A^a_\mu) f_{abc} A^{\mu,b} A^{\nu,c} - \frac{1}{4}g^2 f^{abc} A_{\mu,b} A_{\nu,c} f_{ade} A^{\mu,d} A^{\nu,e}.
\end{aligned} \tag{2.13}$$

The first term in Eq. (2.13) is the same Lagrangian as a free Dirac field, representing the quark kinetic term in QCD. The second term is the interaction term between quarks and gluons while the third term describes the kinetic term of the gluon fields. There is a noticeable analogy between the form of the QED and QCD Lagrangian; a photon in QED is replaced by a gluon in QCD as a mediator of the interaction. The last two terms appearing in Eq. (2.13) indicate that gluons can interact with themselves, e.g., three-gluon and four-gluon interactions. The gluon self-interaction plays an important role in QCD since it is responsible for many features of QCD, such as asymptotic freedom and colour confinement.

Asymptotic freedom states that the strength of the strong interaction between quarks and gluons becomes weaker as the energy scale of the interaction increases. This implies

[2]Non-Abelian gauge theories require anti-commuting scalar fields, called Faddeev-Popov ghost fields, to enforce unitarity in non-physical gauges. As we will not need the ghost field explicitly, they will not be discussed further in this thesis.

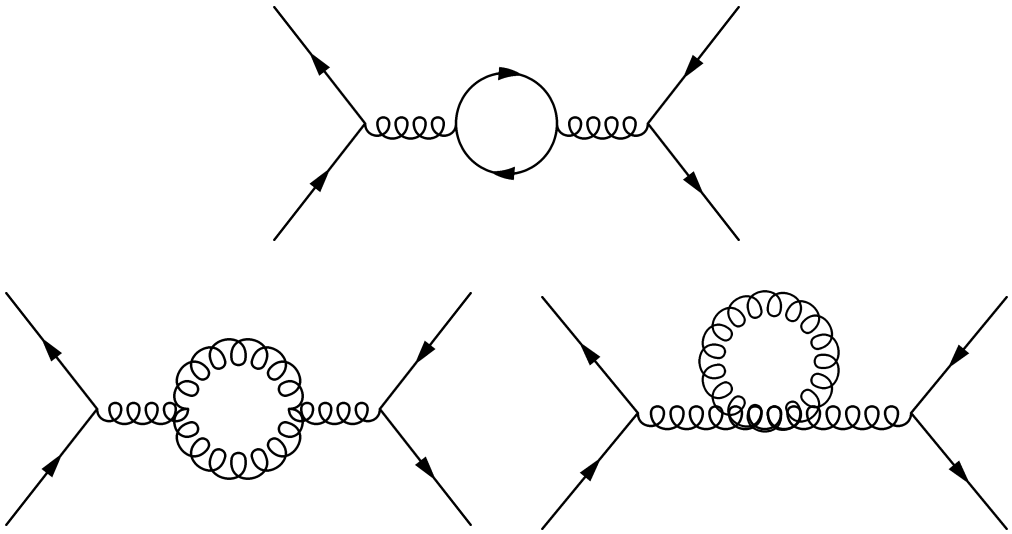

Figure 2.1: (Top panel) Quark-loop correction to the gluon propagator mediating quark-quark scattering. This diagram appears in both QED and QCD. In QED, the gluon propagator is replaced by a photon propagator. (Bottom panel) Gluon-loop corrections to the same scattering, which emerges only in non-Abelian gauge theory. This diagram contributes to the decreasing running coupling as the scale increases.

that quarks and gluons behave as nearly free particles at a large energy scale because the coupling constant is highly suppressed. The scale dependence of the strong coupling is controlled by the renormalization group equation [23–26]. In perturbation theory, the corresponding β-function takes the form

$$\mu_R^2 \frac{d\alpha_s}{d\mu_R^2} = \beta(\alpha_s) = -\alpha_s^2(\beta_0 + \beta_1\alpha_s + \beta_2\alpha_s^2 \cdots), \tag{2.14}$$

where μ_R^2 is a renormalization scale. At leading order in the perturbative expansion, the solution of Eq. (2.14) is given by

$$\alpha_s(\mu_R^2) = \frac{1}{\beta_0 \ln\left(\mu_R^2/\Lambda_{QCD}^2\right)}, \tag{2.15}$$

where

$$\Lambda_{QCD} = \mu_0^2 \exp\left[-\frac{1}{\beta_0}\frac{1}{\alpha_s(\mu_0^2)}\right] \tag{2.16}$$

$$\sim 200 \text{ MeV} \tag{2.17}$$

is a QCD scale at which perturbation theory definitely breaks down. The renormalization scale μ_R is chosen to represent the scale where the interaction occurs. The one-loop β-function coefficient β_0 is given by [27–30]

$$\beta_0 = \frac{1}{4\pi}\left(11 - \frac{2}{3}n_f\right), \tag{2.18}$$

where n_f is the number of quark flavours. The second term in Eq. (2.18) comes from the quark-loop corrections to the gluon propagator as shown in Fig. 2.1 (Top). The first term is contributed by the gluon self-interaction terms in Fig. 2.1 (Bottom), making the overall sign of β_0 positive, as long as $n_f < 33/2$. QCD with six quark flavours satisfies this condition. Consequently, the running coupling $\alpha_s(\mu_R^2)$ asymptotically approaches zero in the limit $\mu_R^2 \to \infty$.

Owing to asymptotic freedom, the strong interactions at high energy can be calculated using perturbation theory, i.e., higher-order terms can be neglected in a perturbative expansion in the strong coupling constant α_s. Many high-energy nuclear reaction experiments are in the regime of perturbative QCD (pQCD), where the asymptotic behaviour of the strong coupling constant has been well tested as shown in Fig. 2.2.

Another interesting phenomenon in QCD emerging at a low energy domain is colour confinement: only colour-singlet states can appear at microscopic scales. At low energy, interactions between quarks and gluons become stronger, making it harder to isolate coloured quarks or gluons from their bound states. As a consequence, quarks and gluons always form bound states of a pair of quark and anti-quark (mesons) or those of three

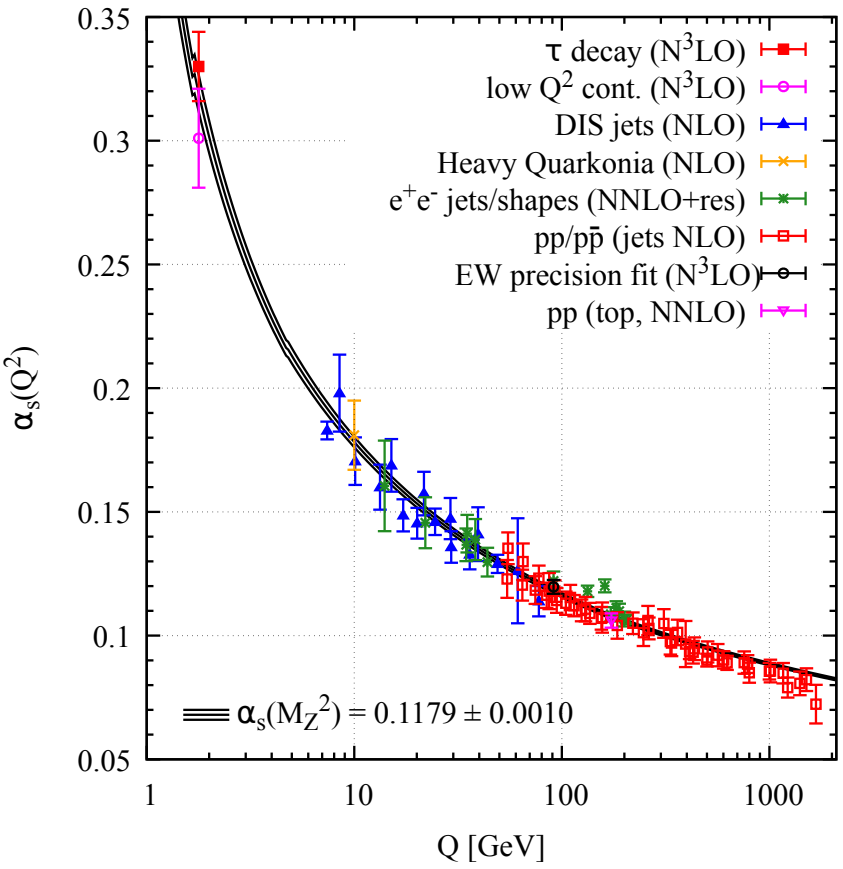

Figure 2.2: Summary of various experimental measurements of the strong coupling constant α_s as a function of the interaction energy scale Q. Comparison to theoretical prediction is present [31].

quarks (baryons)[3]. Although an analytic derivation from first principles is still challenging, numerical simulations of lattice QCD support the presence of colour confinement.

Asymptotic freedom and colour confinement are the basic ideas behind the different phases of the QCD matter. In the following section, we discuss the QCD phase diagram that describes the QCD matter under different conditions and the phase transitions.

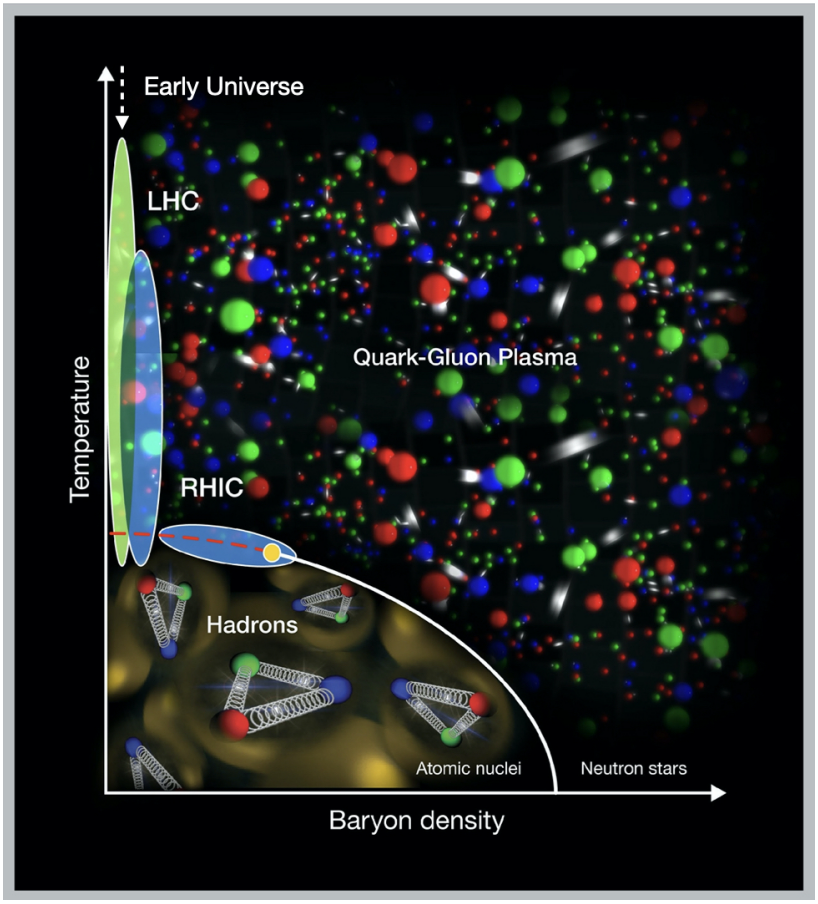

Figure 2.3: Schematic QCD phase diagram in the temperature versus baryon chemical potential plane. The hadronic phase is located at the bottom-left corner of the diagram and the rest of the area in the diagram represents the deconfined phase. The border between the partonic and the hadronic phases is represented as a solid white line for first-order phase transition at large baryon densities and a dashed red line for cross-over at low densities. The yellow bulb connecting the two lines indicates the predicted location of the critical point of QCD matter. LHC experiments correspond to the high temperature and the small baryon density region shown as light green. The Beam Energy Scan (BES) experimental program at the RHIC covers a wider range of baryon densities in search of a first-order phase transition and the possible critical point. The figure and the relevant article can be found in the webpage of BNL.

2.2 QCD phase diagram

In Sec. 2.1, we discussed how asymptotic freedom emerges from the QCD Lagrangian. Asymptotic freedom allows quarks and gluons confined within hadrons to have additional degrees of freedom and form a deconfined state of matter. The QCD phase diagram shown in Fig. 2.3 illustrates various states of QCD matter under different conditions displayed in the plane of temperature T and baryon chemical potential μ_B. When two relativistically accelerated nuclei collide, the system can reach high enough temperatures to undergo a phase transition from the hadronic phase to the partonic phase, i.e., quark-gluon plasma. The centre-of-mass energy per nucleon-nucleon pair $\sqrt{s_{NN}}$ is a parameter in high-energy collisions that controls the temperature and the density of the colliding system. With increasing collision energy, the temperature increases and the baryon chemical potential decreases [41]. At the top RHIC energy (200 GeV) and the LHC energies (2.76 to 13 TeV), the number of quarks in the colliding system is comparable to that of anti-quarks, resulting in low net baryon densities. The phase space in the QCD phase diagram corresponding to relativistic heavy-ion collisions overlaps with the path along which the early Universe evolved. Neutron stars are known to be extremely compact and dense such that the densities exceed the critical value for the phase transition. At such high densities, hadrons interpenetrate each other, destroying boundaries where quarks and gluons are confined.

At nearly zero baryon density, lattice QCD calculations predicted that the transition is a smooth cross-over at a certain range of temperatures [12, 13]. This means that the transition temperature T_c is not uniquely defined, but it is estimated to $T_c \sim 150$ MeV with an uncertainty band of $\sim \pm 15$ MeV [12–15, 42]. At finite baryon chemical potential μ_B and low temperature, the phase transition was suggested to be of first order [43, 44]. The Beam Energy Scan (BES) program at the RHIC is designed to search for the first-order phase transition of the QCD matter and a critical point that connects the cross-over

[3]Note that 4- (tetraquark) and 5-quark (pentaquark) states have been observed [32–40] in the past decades and searching for evidence of multiquark state is still a great interest in particle physics.

and first-order phase transition line in the QCD phase diagram [45]. To study baryon-rich systems, the BES program proposed the colliding energy down to 7.7 GeV at Phase 1 and 3.3 GeV at Phase 2 [46]. The Compressed Baryonic Matter (CBM) experiment at the Facility for Antiproton and Ion Research (FAIR) will conduct a similar study at even higher baryon density with centre-of-mass energy $\sqrt{s_{NN}}$ down to 2 GeV [47].

2.3 Quark-gluon plasma

As mentioned in Sec. 2.2, relativistic heavy-ion collisions produce a quark-gluon plasma (QGP). Plasma is a state in which charged particles interact via long-range massless gauge fields [48]. This distinguishes plasma from ordinary neutral states where the inter-particle interactions are short-range. Deconfined colour charges in the QGP are analogous to electric charges in electrodynamic plasma.

A QGP created in heavy-ion (such as gold and lead ions) collision experiments consists of a large number of partons – on the order of thousands for head-on colliding events. Moreover, the mean free time of parton scatterings is much shorter than the lifetime of the QGP, driving the fireball to local equilibrium quickly. These conditions allow us to treat the QGP as a macroscopic system characterized by an equation of state (EoS). At an asymptotically high-temperature limit where the strong coupling vanishes, one can assume that the partons in the plasma behave as an ideal gas. The partition function for the ideal gas reads

$$\ln Z = d_i V \int \frac{d^3p}{(2\pi)^3} \ln\left(1 \pm e^{-\beta(\omega-\mu)}\right)^{\pm 1}, \tag{2.19}$$

where d_i is the number of degrees of freedom for the particle i and V the total volume of the system. The chemical potential μ is for a conserved charge associated with the particle (net baryon density μ_B in this case). The $+$ $(-)$ sign refers to Fermi-Dirac (Bose-Einstein) distributions. In a massless and zero net baryon density limit, the pressure p is obtained

by the thermodynamic relationship

$$p = \frac{1}{\beta}\frac{\partial \ln Z}{\partial V} = d_i \frac{\pi^2}{90} T^4 \times \begin{cases} 1 & : \text{bosons,} \\ 7/8 & : \text{fermions.} \end{cases} \tag{2.20}$$

Gluons have $N_C^2 - 1$ colours with two spin states where $N_C = 3$ for QCD. The degeneracy factor for gluons d_g is 16. For massless quarks, there are N_c colours with two spin states and an additional factor of 2 for counting quarks and anti-quarks. While quarks come in six flavours with different masses, N_f light quarks are assumed to be massless and thus degenerate. The degeneracy factor for the massless quarks d_q is $12N_f$. With the total degeneracy factor for a QGP $d_{QGP} = d_g + d_q$, the Stefan-Boltzmann (SB) limit of the QGP pressure reads

$$p = \left(16 + \frac{21}{2} N_f\right) \frac{\pi^2}{90} T^4. \tag{2.21}$$

Similarly, the energy density ϵ, the entropy density s, and the speed of sound c_s for the ideal gas of the QGP in the SB limit are calculated straightforwardly:

$$\epsilon = -\frac{1}{V}\frac{\partial \ln Z}{\partial \beta} = 3p, \tag{2.22}$$

$$s = \frac{\partial p}{\partial T} = \frac{4p}{T}, \tag{2.23}$$

$$c_s = \sqrt{\frac{\partial p}{\partial e}} = \sqrt{\frac{1}{3}}. \tag{2.24}$$

The Wuppertal-Budapest (WB) [49] and HotQCD [50] collaborations have performed numerical simulations of QCD on the lattice to estimate the equation of state in the finite temperature and zero chemical potential limit. The results from the two collaborations shown in Fig. 2.4 are consistent with each other, presenting the pressure and the scaled entropy density of a QGP approaching the SB limits. They also agree with the Hadron Resonance Gas (HRG) model [54, 55] predictions [51] at the low temperatures, which assumes a system of non-interacting free hadrons and resonances [50]. Fig. 2.5 shows a Bayesian analysis [53] to estimate the speed of sound in the QGP phase. The posterior

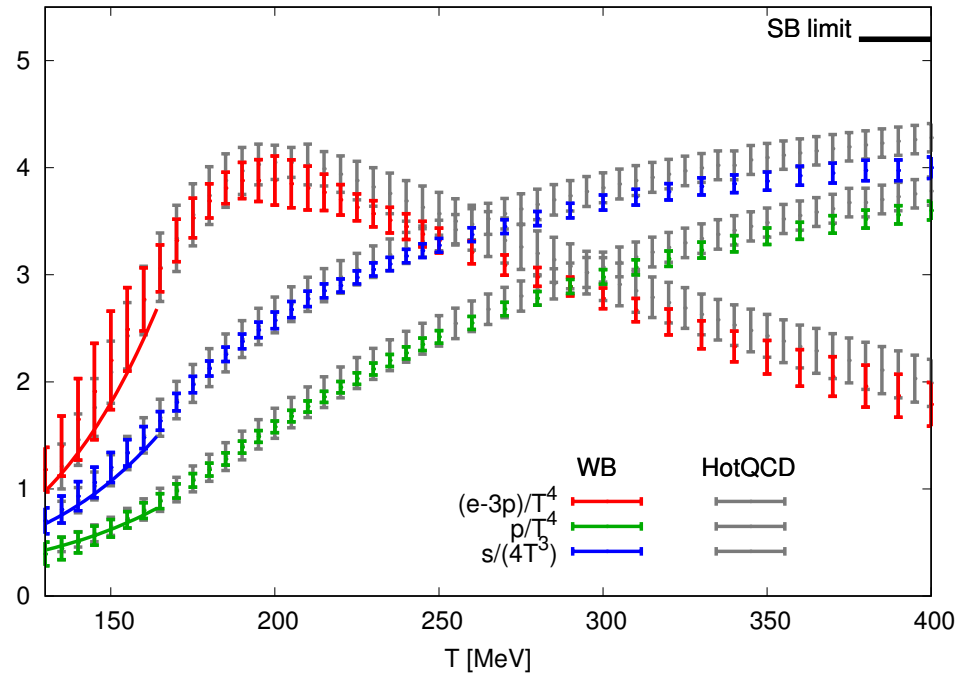

Figure 2.4: Lattice QCD calculations for the trace anomaly, pressure, and scaled entropy density obtained from the WB [49] (coloured) and HotQCD [50] (grey) collaborations. The two independent results are consistent with each other. The pressure and scaled entropy density approach the SB limit at high temperatures. The solid lines on the left show the results from the Hadron Resonance Gas (HRG) model [51]. This figure is reproduced from [52].

distributions based on a comparison of data to models are remarkably consistent with the results from lattice QCD simulations and smoothly connect to the HRG results.

2.4 Summary

In this chapter, we have introduced the $SU(3)$ non-Abelian QCD Lagrangian for interactions between quarks and gluons. It is noteworthy that the non-Abelian gauge field requires the gluon self-interaction terms, resulting in a vanishing running coupling constant $\alpha_s(\mu_R^2)$ in the high energy limit. This behaviour of the QCD running coupling $\alpha_s(\mu_R^2)$ is the origin of asymptotic freedom and colour confinement. We have also discussed that

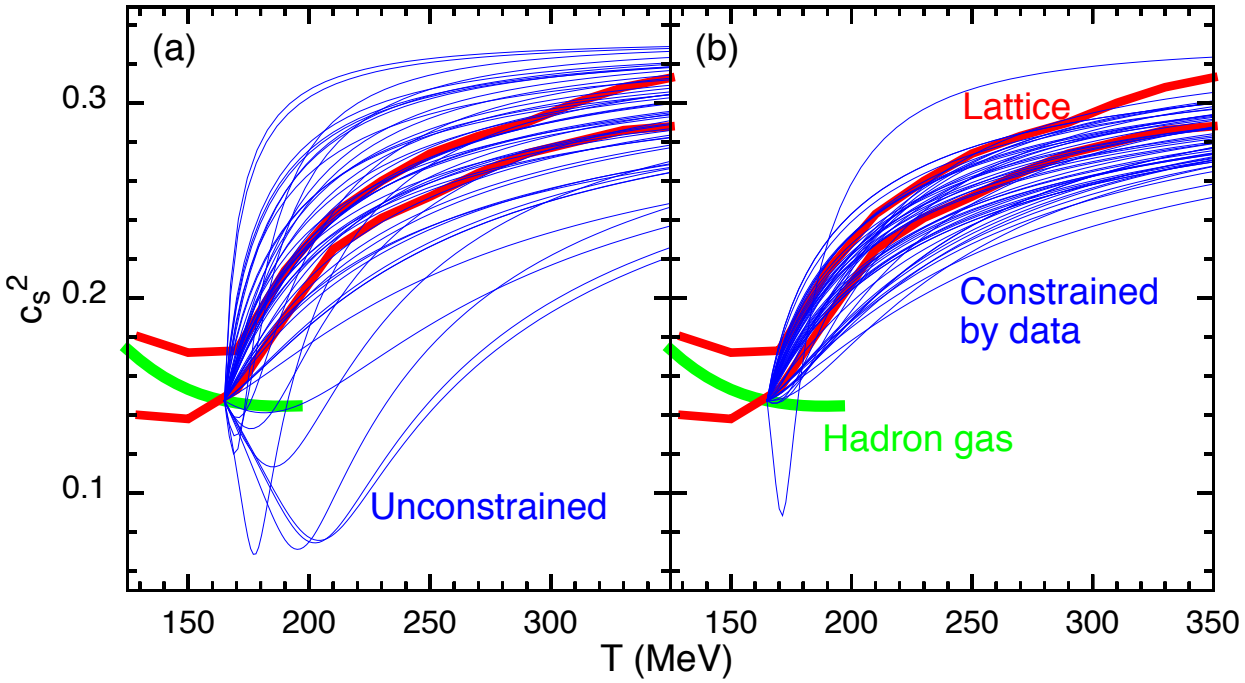

Figure 2.5: Constraints on the QCD sound of speed as a function of temperature obtained from Bayesian analysis [53]. (a) Fifty equations of state were produced by choosing the parameters from the prior distribution randomly and (b) weighted by the posterior likelihood distribution. The RHIC and the LHC experimental data were used to determine the likelihood distribution. The two red curves in each figure represent the lattice QCD calculations [50] and the green line shows the result from the Hadron Resonance Gas (HRG) model. This figure is reproduced from [52].

QCD has been well tested via experimentally measurable quantities, such as running strong coupling $\alpha_s(\mu_R^2)$. High-energy heavy-ion programs in the RHIC and the LHC are important applications of QCD which allow us to access the new state of deconfined QCD matter. In the QCD phase diagram, the phase space for heavy-ion collisions corresponds to the high temperature and low net baryon density sector through which the early Universe has evolved. Lattice QCD has estimated QCD equations of state with thermal pressure approaching the SB limit of the ideal gas at high temperatures.

In the next chapter, we shall provide a theoretical description of jet production in particle collisions. We will cover the QCD-improved parton model and the DGLAP evolution functions that explain the parton density inside a nucleon.

Chapter 3

Jet production

Jets produced in heavy-ion collisions are the main object of study in this dissertation. They are produced by inelastic scattering between two incoming nucleons in high-energy collisions. QCD, together with perturbation theory, provides a theoretical description of jet evolution in the high energy limit. Meanwhile, the distributions of partons within nucleons are encoded in parton distribution functions (PDFs). A precise knowledge of PDFs is essential in predicting all QCD processes such as jet production. Although the inherent non-perturbative nature of PDFs makes first principles calculations difficult, their scale dependence can be described perturbatively.

In Sec. 3.1, we discuss the deep-inelastic scattering (DIS) process [56–67] and evaluate the DIS cross-section using the corresponding Feynman diagram. Sec. 3.2 explains the cross-section for deep-inelastic scattering using the parton model [68, 69] with parton distribution functions (PDFs) at tree level. In Sec. 3.3, the parton model is extended to QCD corrections including the Altarelli-Parisi splitting function [70]. We also derive the DGLAP evolution equation [70–72] using the QCD-improved parton model and discuss how PDFs evolve based on the DGLAP equation. Sec. 3.4 discusses hadron-hadron collisions as an application of the QCD-improved parton model. This chapter is summarized in Sec. 3.5.

3.1 Deep-inelastic scattering

Deep-inelastic scattering (DIS) offers an opportunity to investigate the structure of a nucleon. A series of deep-inelastic electron-proton scattering experiments in the 1960's at the Stanford Linear Accelerator Center (SLAC) discovered that the protons were not point-like objects [56,57]. Instead, the electrons scattered off point-like constituent quarks inside the nucleons. In deep-inelastic electron-proton scattering, the reaction is expressed as

$$e^- + p \to e^- + X, \tag{3.1}$$

where X is two or more final state hadrons, consisting of a quark jet and the outgoing beam remnant. Assuming the scattering is mediated by a single photon, the square of the four-momentum transfer Q^2 of the exchanged photon determines the unique hard scale of the process. When the squared momentum transfer Q^2 is small compared to the mass of the colliding proton ($M_p^2 \sim 1$ GeV^2), the electron scatters off elastically, resulting in a simple $e^- p \to e^- p$ reaction. For large $Q^2 \gg 1$ GeV^2, the virtual photon probes the constituents of the proton, provoking deeply inelastic scatterings.

Fig. 3.1 illustrates the reaction in Eq. (3.1), where k and k' are momenta of the incoming and outgoing electron and P the proton momentum. With the initial kinematic constraints, the squared momentum transfer Q^2 is defined as

$$Q^2 = -q^2 = -(k - k')^2, \tag{3.2}$$

where the negative sign indicates that the momentum transfer q is space-like. For a fixed centre-of-mass energy $s = (P + k)^2$, we can define the Lorentz-invariant scaling variable x and relative energy loss in the lab frame y

$$x = \frac{Q^2}{2P \cdot q}, \tag{3.3}$$

$$y = \frac{P \cdot q}{P \cdot k}, \tag{3.4}$$

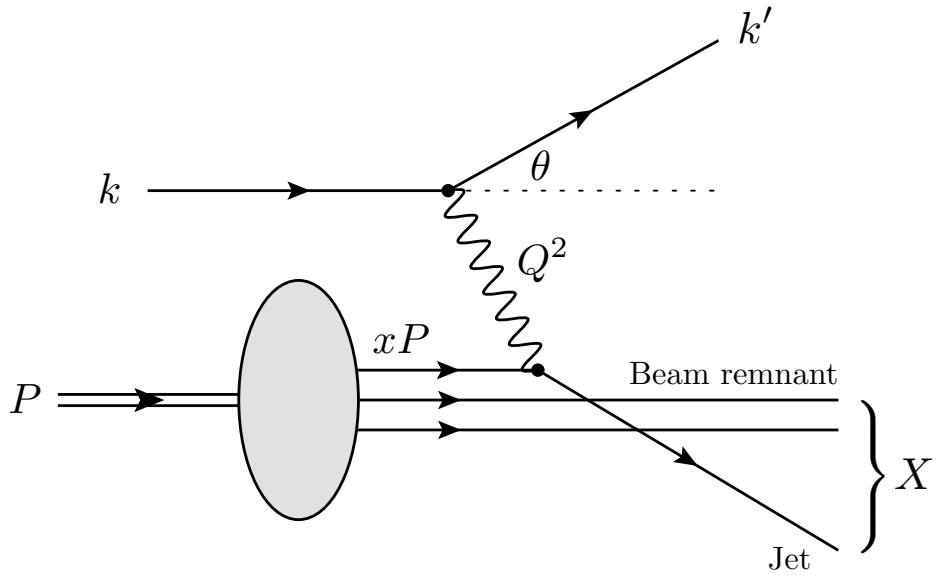

Figure 3.1: Schematic view of deep-inelastic electron-proton scattering.

which satisfy

$$0 \leq x \leq 1, \tag{3.5}$$

$$0 \leq y \leq 1. \tag{3.6}$$

One can obtain $Q^2 = xys$ in the large Q^2 limit where the masses of the electron and proton are ignored. The scaling variable x, together with Q^2, sets the kinematic limits

$$\frac{Q^2}{x} < s. \tag{3.7}$$

The coverage of x and Q^2 by various deep-inelastic scattering experiments are shown in Fig. 3.2.

The unpolarized cross-section for the process in Eq. (3.1) can be written as

$$d\sigma = \sum_X \frac{1}{4kM_p} |\overline{\mathcal{M}}|^2 d\Phi, \tag{3.8}$$

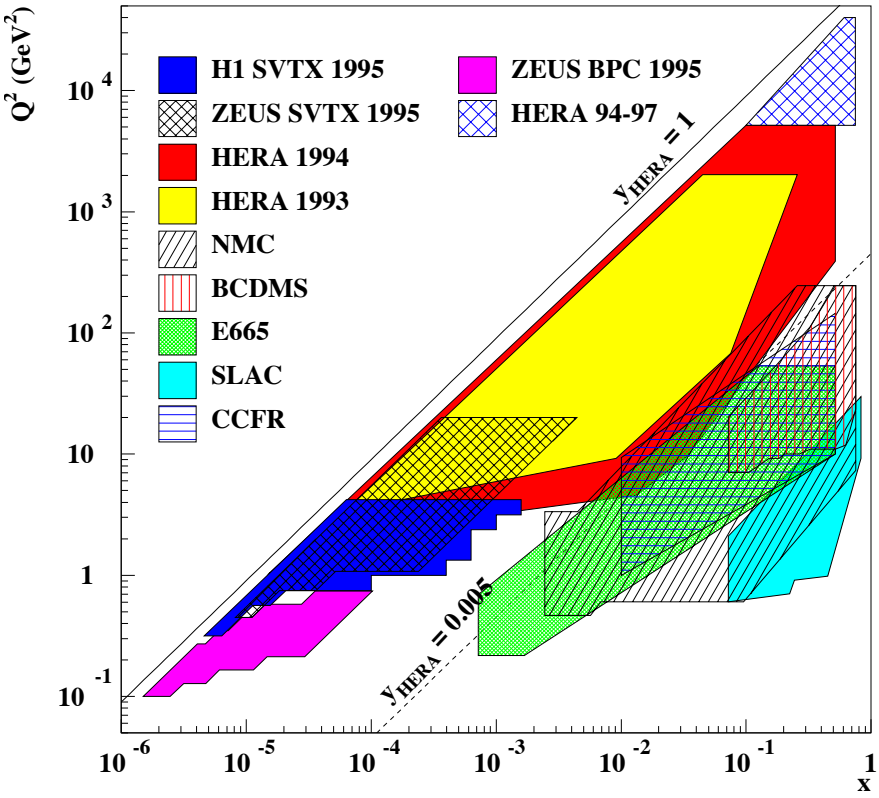

Figure 3.2: Kinematic domains in x and Q^2 for various deep-inelastic scattering experiments [73].

where $|\overline{\mathcal{M}}|^2$ is summed over the spin states of the final particles. From Fig. 3.1, the scattering amplitude $\mathcal{M}$ reads

$$i\mathcal{M} = (-ie)^2 \left(\frac{-ig_{\mu\nu}}{q^2} \right) \langle k' | \, j_l^\mu(0) \, | k \rangle \, \langle X | \, j_h^\nu(0) \, | p \rangle \, , \tag{3.9}$$

where j_l^μ and j_h^μ are the leptonic and hadronic electromagnetic currents. The phase space and the squared matrix element in Eq. (3.8) can be factorized into the leptonic and the

hadronic part

$$d\Phi = \frac{ykM_p}{8\pi^2} dx dy d\Phi_X, \tag{3.10}$$

$$|\overline{\mathcal{M}}|^2 = \frac{e^4}{Q^4} L_{\mu\nu} H^{\mu\nu}, \tag{3.11}$$

where the leptonic tensor $L_{\mu\nu}$ is

$$\begin{aligned} L_{\mu\nu} &= \frac{1}{2} \operatorname{tr} \left[\not{k} \gamma_\mu \not{k}' \gamma_\nu \right] \\ &= \left[k'_\mu k_\nu + k_\mu k'_\nu - k \cdot k' g_{\mu\nu} \right]. \end{aligned} \tag{3.12}$$

Let us define a dimensionless Lorentz tensor $W^{\mu\nu}$

$$W^{\mu\nu} = \sum_X \int d\Phi_X H^{\mu\nu}, \tag{3.13}$$

which describes the hadronic part of the DIS cross-section. Since all phase spaces of possible X are integrated in $W^{\mu\nu}$, it should only depend on the four-vectors P and q. $H^{\mu\nu}$ is constructed out of the current j_h for the proton and follows the current conservation law [74]

$$q_\mu W^{\mu\nu} = q_\nu W^{\nu\mu} = 0. \tag{3.14}$$

Using these constraints, one can find two non-vanishing terms to construct a parity invariant Lorentz tensor[1]. Conventionally these linear combinations are expressed as [75]

$$W^{\mu\nu} = \left[-g^{\mu\nu} + \frac{q^\mu q^\nu}{q^2} \right] F_1(x, Q^2) + \frac{\hat{P}^\mu \hat{P}^\nu}{P \cdot q} F_2(x, Q^2), \tag{3.15}$$

where

$$\hat{P}^\mu = P^\mu - \frac{P \cdot q}{q^2} q^\mu \tag{3.16}$$

[1]QED and QCD conserve parity. Here we consider unpolarized virtual photon exchange. Since weak interaction violates parity, W^- and Z boson exchange introduces an additional combination.

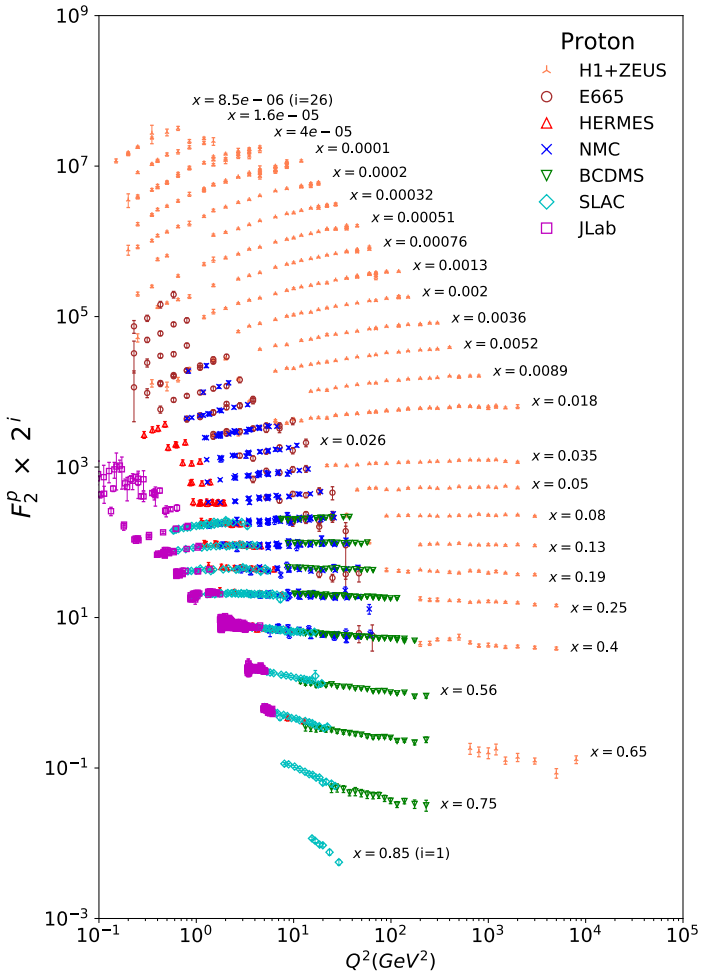

Figure 3.3: The structure function F_2 for a proton measured in an electromagnetic scattering of electrons/positrons and protons from various experiments. This figure is reproduced from the Particle Data Group (PDG) [76].

is the component of P^μ that is transverse to q^μ. The contraction of Eq. (3.12) with Eq. (3.15) yields

$$\frac{d^2\sigma}{dxdy} = \frac{4\pi\alpha^2}{xyQ^2}\left[xy^2F_1(x,Q^2) + \left(1 - y - x^2y\frac{M_p^2}{Q^2}\right)F_2(x,Q^2)\right]. \tag{3.17}$$

The function $F_1(x,Q^2)$ and $F_2(x,Q^2)$ are called the structure functions.

In the scaling limit, where $Q^2 \to \infty$ with x fixed, we can neglect the proton mass term M_p^2/Q^2 and Eq. (3.17) can be reorganized

$$\frac{d^2\sigma}{dxdy} = \frac{2\pi\alpha^2}{xyQ^2}\left[\{1 + (1-y)^2\}F_2(x,Q^2) - y^2F_L(x,Q^2)\right], \tag{3.18}$$

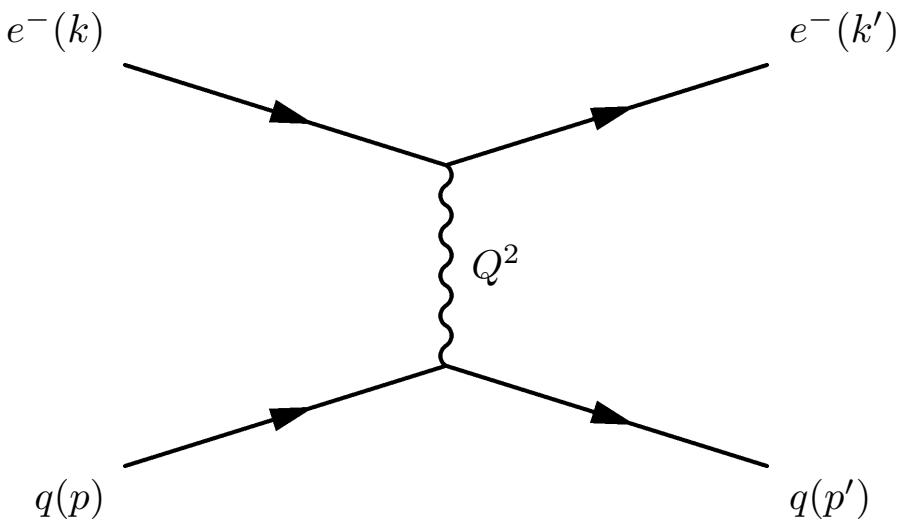

Figure 3.4: Feynman diagram for elastic electron-parton scattering at tree level.

where $F_L = F_2 - 2xF_1$ is the longitudinal structure function [61–67], which is related to the absorption of a longitudinally polarized virtual photon. Interestingly, in the scaling limit, $F_L(x, Q^2)$ vanishes and $F_2(x, Q^2)$ becomes independent of Q^2 [77]. The latter, often referred to as Bjorken scaling, approximately agrees with the measurements over a broad range of Q^2 as shown in Fig. 3.3. Bjorken scaling is valid up to the first-order approximation in perturbation theory. Higher-order corrections to the strong coupling α_s, which come with gluons, violate Bjorken scaling as we will discuss later in this chapter.

3.2 Parton model

The parton model assumes that a proton consists of point-like partons bound by strong interactions. Under this assumption, deep-inelastic electron-proton scattering can be viewed as an elastic scattering of the electron and one of the constituent partons in the proton as depicted in Fig. 3.4. This assumes the premise that only partons carrying an electric charge can be involved the interaction. The corresponding partonic cross-section

is

$$d\hat{\sigma} = \frac{1}{2\hat{s}}|\overline{\mathcal{M}}|^2 d\hat{\Phi}, \tag{3.19}$$

where the hat notation denotes a partonic interaction. Again, the squared matrix element can be decomposed into the leptonic tensor in Eq. (3.12) and the partonic tensor $Q^{\mu\nu}$

$$Q^{\mu\nu} = \frac{1}{2}\,\mathrm{tr}\left[\not{p}\gamma^{\mu}\not{p}'\gamma^{\nu}\right]. \tag{3.20}$$

Assuming that the struck parton (a quark in this case) carries a fractional momentum $p = \xi P$ of the proton momentum P, the resulting differential cross-section reads

$$\frac{d^2\hat{\sigma}}{dxdy} = \frac{2\pi\alpha^2}{xyQ^2}\left[\{1 + (1-y)^2\}\right] xe_q^2\delta(x-\xi). \tag{3.21}$$

The total cross-section for all possible species of partons q and values of ξ is

$$\frac{d^2\sigma}{dxdy} = \frac{2\pi\alpha^2}{xyQ^2}\sum_q \int_0^1 d\xi f_q(\xi)\left[1 + (1-y)^2\right] xe_q^2\delta(x-\xi), \tag{3.22}$$

where the parton distribution function $f_q(\xi)$ is defined as the probability of finding a parton of flavour q carrying a momentum fraction ξ of the proton.

Comparing Eq. (3.18) and Eq. (3.22), we find the structure function predicted by the parton model

$$F_2(x) = \sum_i \int_0^1 d\xi f_i(\xi) xe_q^2\delta(x-\xi) = x\sum_i e_q^2 f_i(x) \tag{3.23}$$

$$F_L(x) = F_2(x) - 2xF_1(x) = 0. \tag{3.24}$$

Note that $F_2(x)$ in the parton model has no Q^2 dependence. Eq. (3.24) is known as the Callan-Gross relation [79]. Recalling that a proton consists of two u quarks and one d

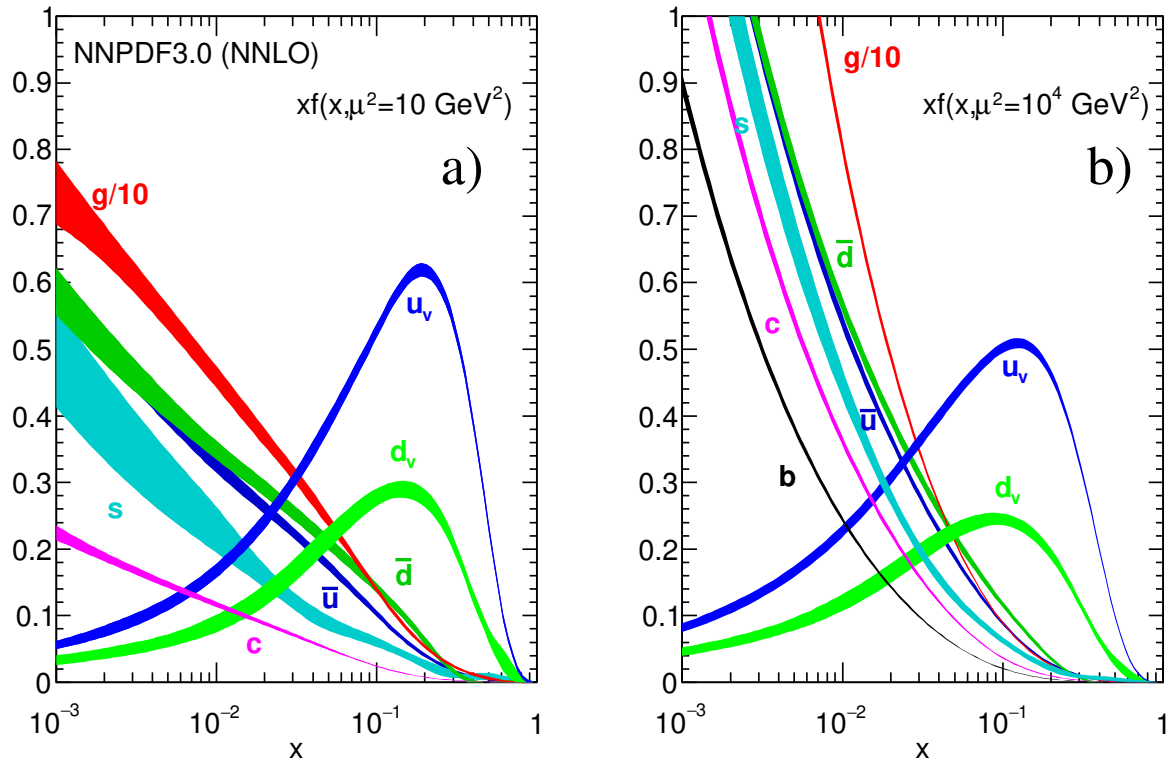

Figure 3.5: Scaled unpolarized parton distribution function $xf(x)$ for u_v, $\bar{u}$, d_v, $\bar{d}$, $s \simeq \bar{s}$, $c = \bar{c}$, $b = \bar{b}$, and g obtained in the NNLO NNPDF3.0 global fit at the energy scales $\mu^2 = 10$ GeV^2 (left) and $\mu^2 = 10^4$ GeV^2 (right) [78]. This figure is reproduced from the Particle Data Group (PDG) [76].

quark, the flavour sum rules [80] for a proton are

$$\int_0^1 dx\,[u(x) - \bar{u}(x)] = \int_0^1 dx\,u_v(x) = 2 \tag{3.25}$$

$$\int_0^1 dx\,[d(x) - \bar{d}(x)] = \int_0^1 dx\,d_v(x) = 1 \tag{3.26}$$

$$\int_0^1 dx\,[s(x) - \bar{s}(x)] = 0 \tag{3.27}$$

$$\int_0^1 dx\,x\left[\sum_i [q_i(x) + \bar{q}_i(x)] + g(x)\right] = 1. \tag{3.28}$$

where $u(x)$, $d(x)$, and $s(x)$ are a shortened notation for the u, d, and s quark distribution function respectively and the subscript v indicates the valance quarks. Eq. (3.28)

stems from the physical constraints that the proton momentum must be carried by its constituent partons. The gluon PDF $g(x)$ will be discussed later. Fig. 3.5 illustrates the parton distribution functions for quarks and gluons in a proton obtained by a global analysis [78]. The PDFs have a weak dependence on the energy scale of $\mu^2 = Q^2$. While valance quarks are dominant at large x, more sea quarks are probed in the proton at smaller x and larger Q^2.

Using $dy = dQ^2/\hat{s}$ and $\delta(x-\xi) = \frac{1}{\xi}\delta(1-\frac{x}{\xi})$, we write the cross-section for deep-inelastic scattering as a combination of the PDFs and the cross-section for each parton

$$\frac{d^2\sigma}{dxdQ^2} = \sum_q \int_x^1 \frac{d\xi}{\xi} f_q(\xi) \frac{d^2\hat{\sigma}}{dxdQ^2}\left(\frac{x}{\xi}, Q^2\right). \tag{3.29}$$

According to the factorization theorem, the hadronic process in deep-inelastic scattering can be factorized into a hard and a soft part separated by an arbitrary factorization scale. In Eq. (3.29), the differential cross-section for electron-parton scattering is treated perturbatively and is calculable from first principles. On the other hand, the PDFs in the proton lie in the domain of non-perturbative QCD, which has to be modelled and fitted to data. However, the universality of the PDFs, i.e. independent of scattering processes, makes it much easier to estimate the inelastic cross-section in colliding experiments.

3.2.1 Scaling violations

The global fit analysis for the proton PDFs shown in Fig. 3.5 shows that at small x, the majority of the proton momentum is carried by gluons[2]. Roughly speaking, the proton momentum carried by quarks is only 50% [60]

$$\int_0^1 dx\, x \sum_{q,\bar{q}} q(x) \simeq 0.5. \tag{3.30}$$

[2]Note that the gluon distribution function $g(x)$ is reduced by a factor of 10 in Fig. 3.5.

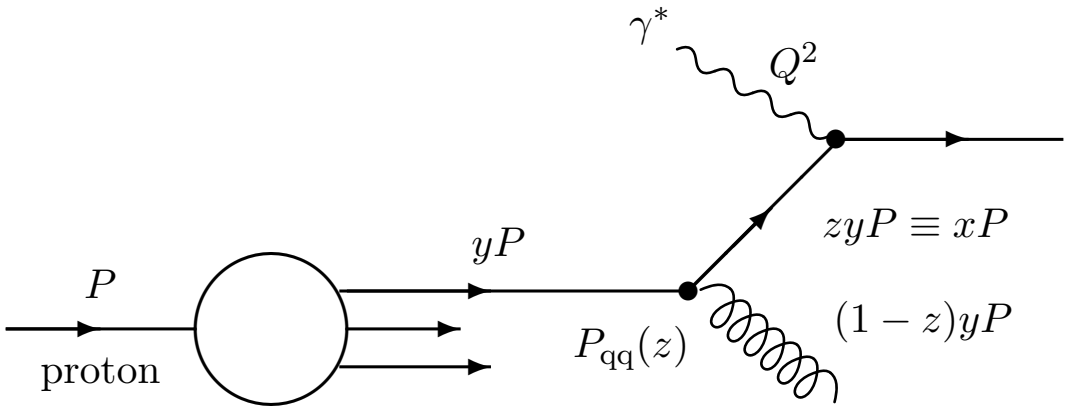

Figure 3.6: The schematic diagram for deep-inelastic scattering with gluon splitting.

This is the first indirect evidence of an electrically neutral parton inside a proton, which has been identified as a gluon.

So far we have considered deep-inelastic electron-quark scattering at leading order. Although Bjorken scaling is a good approximation, we have already seen the Q^2 dependence of $F_2(x, Q^2)$ in Fig. 3.3. The structure function $F_2(x, Q^2)$ increases with larger Q^2 for small $x \sim 0$ and decreases for large $x \sim 1$ [81]. To understand scaling violations, the perturbative calculation for the partonic cross-section in Eq. (3.19) has to be extended to higher-order in the strong coupling α_s. For instance, a quark may radiate a gluon before or after interacting with the virtual photon. These contributions can be computed from the QCD Lagrangian and, owing to the renormalization group equation, the PDFs $f_i(x)$ are no longer independent of Q^2, but they evolve with Q^2.

The next section will discuss the QCD-improved parton model that includes fully-corrected gluon radiation. It also covers the DGLAP equations, which describe the evolution of the PDFs on energy scales.

3.3 QCD-improved parton model

The QCD-improved parton model begins with incorporating gluon corrections to the cross-section of deep-inelastic scattering. Let us consider a quark originating from a proton radiates a gluon and interacts with virtual photon as shown in Fig. 3.6. The quark carries a fraction y of the proton momentum and radiates a gluon with a fraction $1-z$ of its momentum. We define the quark momentum scattering off the virtual photon as $zyP \equiv xP$, meaning that $z = x/y$. Summing over all real gluon radiation diagrams contributing to deep-inelastic scattering, we obtain

$$\frac{F_2(x,Q^2)}{x} = \sum_q \int_x^1 \frac{dy}{y} f_q(y) e_q^2 \left[\delta(1-z) + \frac{\alpha_s}{2\pi}\left(P_{qq}(z)\ln\left(\frac{Q^2}{\mu_0^2}\right) + C_q(z)\right)\right], \tag{3.31}$$

where $P_{ab}(z) = P_{a\to bc}(z)$[3] is the Altarelli-Parisi splitting function, defined as the probability that a parton a radiating a parton c and becomes a parton b carrying a momentum fraction z of the original parton a. The known function $C(z)$ is the process-dependent coefficient function. The $\delta(1-z)$ term appearing in Eq. (3.31) indicates the zeroth-order contribution that we have discussed earlier in Eq. (3.23). The arbitrary cut-off μ_0^2 regulates the colinear divergence, which occurs in the limit when the transverse momentum of the gluon goes to zero.

The complete set of the Altarelli-Parisi splitting functions and the corresponding shortened notations are summarized in Table. 3.1. The plus prescription in $P_{qq}(z)$ and $P_{gg}(z)$, defined by

$$\int_0^1 dz \frac{f(z)}{(1-z)_+} = \int_0^1 \frac{f(z)-f(1)}{(1-z)}, \tag{3.32}$$

where $(1-z)_+ = (1-z)$ for $z < 1$, is introduced to avoid the singularities showing up at $(1-z) \to 0$. The splitting functions $P(z)$ comply with the momentum conservation law in Eq. (3.28).

[3]In this process, the radiated parton c is uniquely defined by the conservation law and the available QCD Feynman diagrams. Thus c in $P_{a\to bc}(z)$ can be omitted and this process can be expressed as $P_{ab}(z)$.

Process	Splitting function
$q \to qg$	$P_{qq}(z) = \frac{4}{3}\left[\frac{1+z^2}{(1-z)_+} + \frac{3}{2}\delta(1-z)\right]$
$q \to gq$	$P_{qg}(z) = \frac{1}{2}\left[z^2 + (1-z)^2\right]$
$g \to q\bar{q}$	$P_{gq}(z) = \frac{4}{3}\left[\frac{1+(1-z)^2}{z}\right]$
$g \to gg$	$P_{gg}(z) = 6\left[\frac{z}{(1-z)_+} + \frac{1-z}{z} + z(1-z) + \left(\frac{11}{12} - \frac{n_f}{18}\delta(1-z)\right)\right]$

Table 3.1: The Altarelli-Parisi splitting functions for each QCD splitting process with the shortened notation.

3.3.1 DGLAP equation

Regarding $f(x)$ as an unmeasurable bare parton density at tree level, one can define the renormalized PDF $f(x, \mu_F^2)$ at the factorization scale $\mu_F = \mu$

$$f(x,\mu^2) = f(x) + \int_x^1 \frac{dy}{y} f(y) \frac{\alpha_s}{2\pi}\left[P(z)\ln\left(\frac{\mu^2}{\mu_0^2}\right) + C_1\right], \tag{3.33}$$

which absorbs the unphysical cut-off μ_0. Then the quark structure function in Eq. (3.31) becomes

$$\frac{F_2(x,Q^2)}{x} = \sum_q \int_x^1 \frac{dy}{y} f_q(y,\mu^2) e_q^2 \left[\delta(1-z) + \frac{\alpha_s}{2\pi}\left\{P(z)\ln\left(\frac{Q^2}{\mu^2}\right) + C_2\right\}\right], \tag{3.34}$$

where C_1 and C_2 are determined by the choice of the factorization scheme.

The structure function $F_2(x, Q^2)$ should not depend on the factorization scale μ^2. The renormalization group equation extends to $F_2(x, Q^2)$, leading to

$$\frac{\partial F_2(x,Q^2)}{\partial \ln \mu^2} = 0, \tag{3.35}$$

at leading order in α_s. Substituting Eq. (3.34) into Eq. (3.35) yields

$$\frac{\partial f(x,\mu^2)}{\partial \ln \mu^2} = \frac{\alpha_s}{2\pi}\int_x^1 \frac{dy}{y} f(y,\mu^2)P(z) + \mathcal{O}(\alpha_s^2). \tag{3.36}$$

Eq. (3.36) is called Dokshitzer–Gribov–Lipatov–Altarelli–Parisi (DGLAP) equation. More generally, we can construct a set of $2n_f + 1$ coupled DGLAP equations using the splitting functions shown in Table. 3.1

$$\frac{\partial f_j(x,\mu^2)}{\partial \ln \mu^2} = \sum_i \frac{\alpha_s}{2\pi}\int_x^1 \frac{dy}{y} f_i(y,\mu^2)P_{ij}(z) + \mathcal{O}(\alpha_s^2), \tag{3.37}$$

where i and j denote the parton originating from the proton and the struck parton with virtual photon after splitting, respectively. Eq. (3.36) and Eq. (3.37) are valid at leading order in α_s, but it can be generalized to higher order in perturbative QCD using the generalized splitting functions

$$P_{ij}(z) = P_{ij}^0(x) + \frac{\alpha_s}{2\pi}P_{ij}^{(1)}(z) + \cdots . \tag{3.38}$$

The DGLAP equation in Eq. (3.36) and Eq. (3.37) describes the evolution of the running parton density with the factorization scale μ^2. A convenient choice of the factorization scale is to set $\mu^2 = Q^2$ and now Eq. (3.33) becomes

$$f(x,Q^2) = f(x) + \int_x^1 \frac{dy}{y} f(y)\frac{\alpha_s}{2\pi}\left[P(z)\ln\left(\frac{Q^2}{\mu_0^2}\right) + C_1(z)\right]. \tag{3.39}$$

Although the renormalized parton density in Eq. (3.39) is not calculable because of the arbitrary cut-off μ_0, the DGLAP equations allow us to calculate its dependence on Q^2 based on perturbative QCD. That is, when the x-dependent PDFs are measured at some scale Q^2, we can solve the DGLAP equations to estimate the PDF at different Q^2.

The explicit Q^2 dependence of the parton density in Eq. (3.39) states the scaling violations we discussed in Sec. 3.2.1. The quark density function is modified by the con-

volution of the splitting functions $P(z)$ and logarithmic Q^2 dependence. Physically, the resolution scale of a photon with virtuality Q^2 is proportional to $1/Q$. At higher Q^2, the photon probes more low-x quarks that have experienced splitting processes. The resulting cross-section is characterized by the scaling violation patterns shown in Fig. 3.3.

3.4 Hadron-hadron collisions

An application of the QCD-improved parton model is hadron-hadron collisions, e.g., proton-proton and heavy-ion collisions at the RHIC and the LHC. Let us consider a proton-proton collision illustrated in Fig. 3.7 as an example. Two partons from the colliding protons whose momenta are P_1 and P_2 strongly interact based on QCD, producing jets and the beam remnants

$$p(P_1) + p(P_2) \to \text{jet} + X. \tag{3.40}$$

The produced jets are often back-to-back di-jets because of energy-momentum conservation and their virtualities are proportional to the momentum exchange Q^2. The corresponding inclusive cross-section is

$$\begin{aligned} d\sigma(P_1, P_2) = \sum_{i,j} \int dx_1 dx_2 f_i(x_1, \mu_F^2, \alpha_s(\mu_R^2)) f_j(x_2, \mu_F^2, \alpha_s(\mu_R^2)) \\ \times d\hat{\sigma}_{ij}\left(x_1 P_1, x_2 P_2, \alpha_s(\mu_R^2), \frac{Q^2}{\mu_F^2}, \frac{Q^2}{\mu_R^2}\right) + \mathcal{O}\left(\frac{\Lambda_{QCD}}{Q}\right)^p. \end{aligned} \tag{3.41}$$

The PDFs $f_i(x, \mu_F^2)$ with the factorization scale μ_F defined in Eq. (3.33) have the $\alpha_s(\mu_R^2)$ dependence as in Eq. (3.33). The renormalization scale μ_R and the QCD parameter Λ_{QCD} are introduced in Eq. (2.15). Note that the PDFs are universal in any processes. The similar factorization scheme applies to the inclusive parton-parton cross-section $\hat{\sigma}_{ij}$ with two PDFs. Factorization is valid up to power corrections of order $\left(\frac{\Lambda_{QCD}}{Q}\right)^p$, where p is positive and process-dependent.

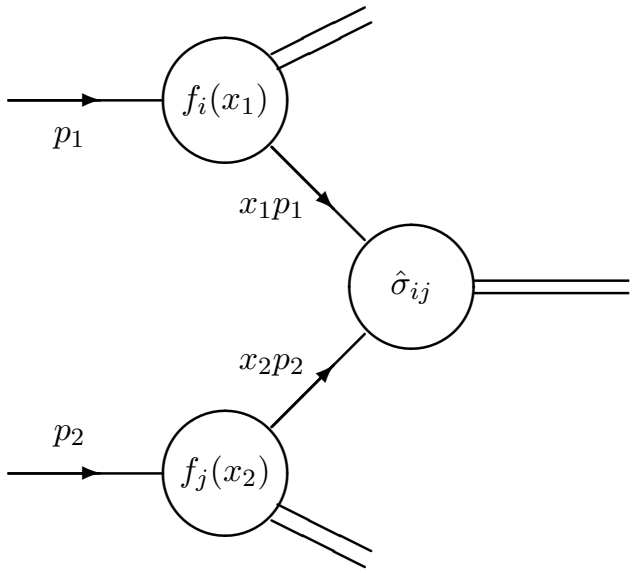

Figure 3.7: The schematic diagram for hadron-hadron inelastic scattering.

3.5 Summary

In this chapter, we have discussed the theoretical framework for jet production. In deep-inelastic electron-proton scattering, a highly virtual photon has strong resolution power to probe partons inside the proton. The parton model introduces the parton distribution functions to account for the non-perturbative structure functions of nucleons. In the high Q^2 limit with fixed x, deep-inelastic scattering features Bjorken scaling, which is violated at higher-order in $\alpha_s(\mu_R^2)$ because of the QCD corrections involving gluon radiation. The Altarelli-Parisi splitting functions describe these QCD processes and can be evaluated perturbatively using QCD Feynman diagrams. The scale evolution of the renormalized PDFs, which contain the bare PDFs and the higher-order corrections, can be described by a set of the DGLAP equations. The factorization theorem allows us to separate the hard partonic sector and the PDFs when calculating the deep-inelastic scattering cross-section. Not only that, but this can also be applied to any collision processes that involve perturbative and non-perturbative physics.

The last part of this chapter briefly mentioned the study of hadron-hadron collisions at the RHIC and the LHC as an application of deep-inelastic scattering. Owing to the uni-

versality of the PDFs and the DGLAP evolution equations, we can easily apply these concepts to study jet production in heavy-ion collisions. In the next chapter, we will provide a phenomenological description of heavy-ion collisions and discuss some highlighted measurements that support the creation of a strongly coupled QGP in the collisions.

Chapter 4

Relativistic Heavy-ion collisions

Relativistic heavy-ion collisions provide a unique opportunity to study QCD at high energy scales. One of the biggest achievements of the experimental heavy-ion program is the discovery of the QGP. This has demonstrated the accessibility of the colour-deconfined state at extreme temperatures and densities. For the last few decades, the study of the QGP has been a promising aspect of heavy-ion programs at the RHIC at BNL and LHC at CERN. The relativistic heavy-ion programs have fostered our understanding of how matter emerges from the early universe to the present day. Similar to the evolution of the early universe, the QGP produced in a laboratory undergoes a phase transition to the hadronic state and chemical freeze-out before measurement by a detector.

This chapter is dedicated to an overview of heavy-ion collisions at RHIC and the LHC. Sec. 4.1 provides a phenomenological description of the heavy-ion collisions. Then we discuss the two important topics: collectivity in Sec. 4.2 and hard probes in Sec. 4.3 of the strongly coupled QGP observed at the collision experiments. Sec. 4.4 provides a summary of this chapter.

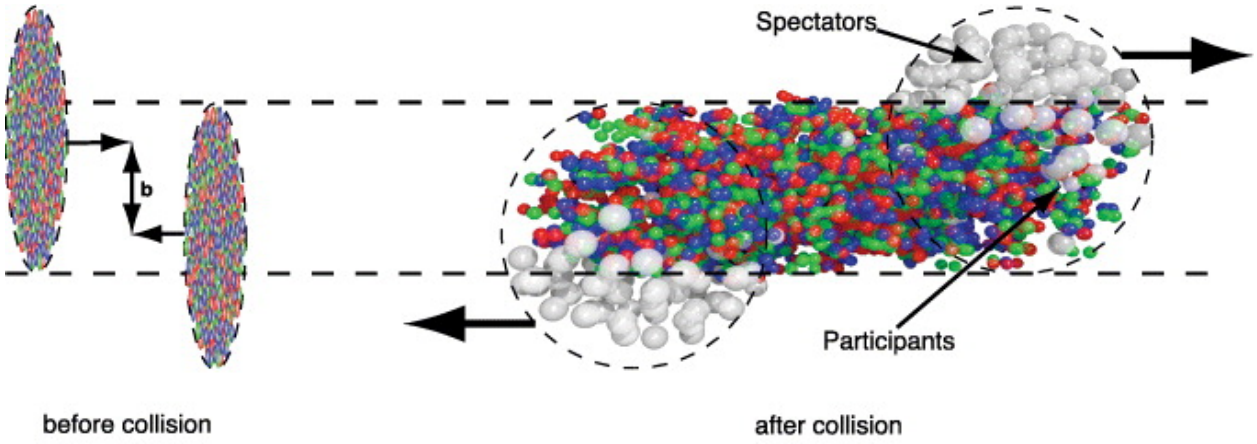

Figure 4.1: Schematic view of relativistic heavy-ion collisions in the longitudinal plane. The two black-dashed lines indicate the overlap (colliding) zone. (Left) Two Lorentz-contracted nuclei before the collision with impact parameter b. (Right) The two nuclei after the collision. The spectators shown as white balls outside of the overlap zone pass by each other while their paths remain nearly unaffected by the collisions. The participants inside the overlap zone interact strongly with each other, producing a hot and dense plasma of quarks and gluons. This figure is reproduced from [82].

4.1 Phenomenology of heavy-ion collisions

When a nucleus is accelerated to relativistic velocities, the thickness of the nucleus is Lorentz contracted to $2R/\gamma$, where R is the radius of the nucleus and γ is the Lorentz factor. At the top RHIC energy of $\sqrt{s_{NN}} = 200$ GeV and the LHC energy of $\sqrt{s_{NN}} = 2.76$ TeV, the γ are approximately 110 and 1500, respectively. Because these energy scales are large enough to have inelastic scattering processes, quarks and gluons inside the nucleons can participate in strong interactions with those in the counterpart nucleons at the moment they pass through each other.

The impact parameter b is defined by the transverse distance between the centre-of-masses of the two colliding heavy-ions. For non-central collisions, $b > 0$, nucleons outside of the overlap zone are referred to as spectators, which keep moving in the beam direction without any major interactions. Participants are those inside the overlap zone, colliding with at least one nucleon from the counterpart and producing the QGP. This involves

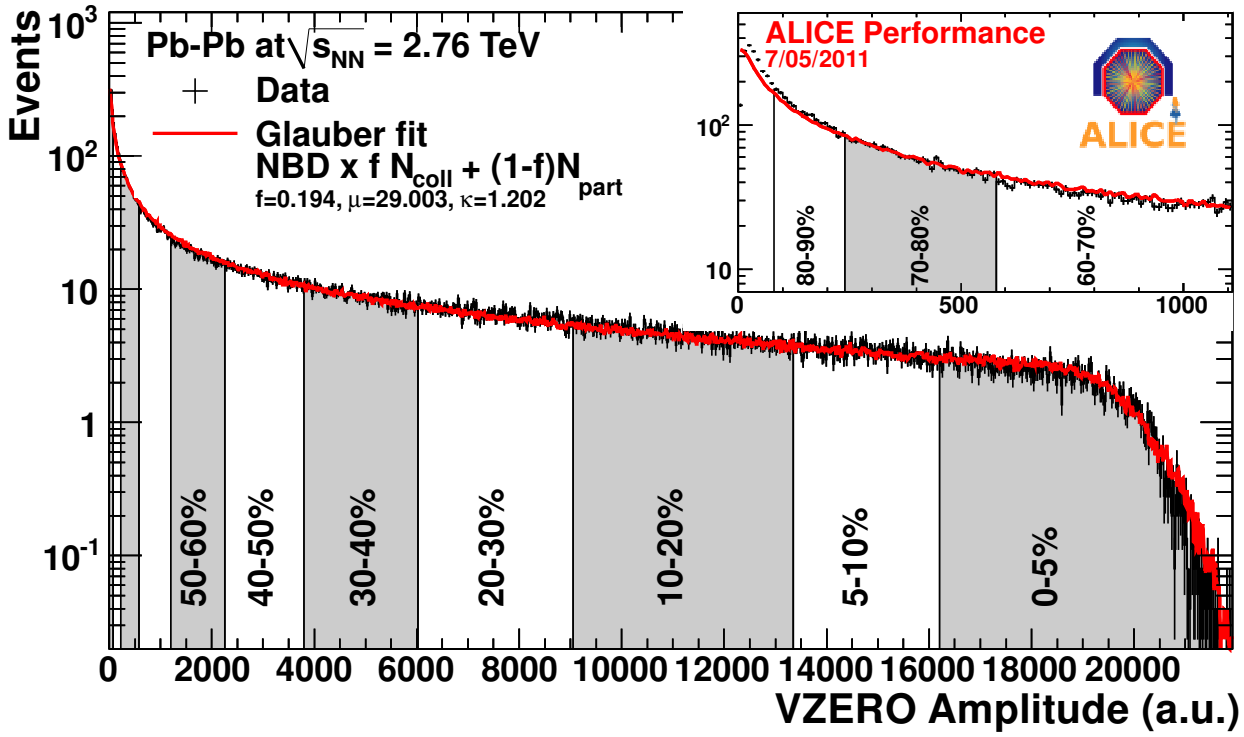

Figure 4.2: The centrality determination at $\sqrt{s_{NN}} = 2.76$ Pb+Pb collisions performed by the ALICE collaboration. The distribution of the amplitudes measured at the VZERO detector is divided by several centrality bins. The Glauber fit using a combination of N_{coll} and N_{part} together with a negative binomial distribution is compared to the distribution. This amplitude distribution is used to estimate the particle multiplicity for a given centrality bin [83].

strong interactions between valence and sea quarks as well as gluons inside the participants. A schematic diagram of two colliding nuclei with non-zero impact parameter is shown in Fig 4.1.

The size of the QGP produced by a collision and the number of particles measured at detectors depend on the impact parameter b or the number of participants N_{part} of the collision. Unfortunately, none of these are measurable quantities because experiments have no control of the exact location of ions. Instead, centrality – the measure of how central the collision is – is determined by measurable quantities such as charged hadron multiplicity. For example, events with the 5% highest charged particle multiplicity correspond to the 0-5% most central collisions. Fig. 4.2 shows how the detector amplitudes, which

	Parameters		
Nuclear	R	a	w
^{1}p	1	1	0
^{16}O	2.608	0.513	-0.051
^{63}Cu	4.218	0.596	0
^{197}Au	6.38	0.535	0
^{208}Pb	6.62	0.546	0

Table 4.1: List of the parameter sets to fit the charge density distributions for nuclei of interest. The values are taken from [84].

are further estimated to particle multiplicity, can be represented as the bins in centrality. The results shown in Fig. 4.2 are measured at $\sqrt{s_{NN}} = 2.76$ TeV Pb+Pb collisions by the ALICE collaboration.

4.1.1 Glauber model

The Glauber model [85–87] is a semi-classical approach to describe heavy-ion collisions in the impact parameter space b[1]. This model calculates the number of participants N_{part} and the number of nucleon-nucleon binary collisions N_{coll} in A+B collisions, where A and B refer to the number of nucleons in the two colliding nuclei. The nuclear charge density $\rho(r)$ and inelastic nucleon-nucleon cross-section σ_{inel}^{NN}, which is measurable from experiments, are used as inputs to the Glauber calculations. The nuclear charge density is parameterized by a Fermi distribution with additional parameters [87],

$$\rho(r) = \rho_0 \frac{1 + w\left(\frac{r}{R}\right)^2}{1 + \exp\left(\frac{r-R}{a}\right)}, \tag{4.1}$$

where ρ_0 is the nuclear charge density at the centre of the nucleus and R is the radius of the nucleus. The additional parameter w characterizes how the shape of the nucleus deviates

[1]Bold minuscule letters are taken to be the notation for two- or three-vectors depending on the dimension of the quantities, $\mathbf{x} \equiv \vec{x}$. The norm of the three-vector will be often defined as $x \equiv |\mathbf{x}|$

Centrality	$dN_{ch}/d\eta$	$\langle N_{part}\rangle$	$(N_{ch}/d\eta)/(\langle N_{part}\rangle/2)$
0-5%	1601 ± 60	382.8 ± 3.1	8.4 ± 0.3
10-20%	966 ± 37	260.5 ± 4.4	7.4 ± 0.3
40-50%	261 ± 9	85.0 ± 2.6	6.1 ± 0.3
70-80%	35 ± 2	15.8 ± 0.6	4.4 ± 0.4

Table 4.2: Selected centrality bins and corresponding charged particle multiplicity at mid-rapidity, the averaged number of participants N_{part}, and multiplicity per participant pair in $\sqrt{s_{NN}} = 2.76$ TeV Pb+Pb collisions. The values are taken from [88]. The charged-particle multiplicity is estimated from the detector amplitude and the averaged N_{part} is obtained by the Glauber calculations. The last column indicates that the particle production rate per binary collision is higher at central collisions. The table for entire centrality bins is available in [88].

from the Wood-Saxon shape and a correspond to the skin depth. For specific nuclei of interest, the corresponding parameters are listed in Table. 4.1. With given parameter sets, ρ_0 is determined by normalization of the charge density distribution,

$$\int d^3r\rho(r) = Ze, \tag{4.2}$$

where Z corresponds to the proton number of the nucleus. In the Glauber model, the charge density is used to represent the nuclear density by adjusting ρ_0 so that

$$\int d^3r\rho_A(r) = A. \tag{4.3}$$

With the two inputs, one can analytically express N_{part} and N_{coll} as a function of impact parameter $\mathbf{b}$ [89],

$$N_{part}(\mathbf{b}) = \int d\mathbf{s}\, T_A(\mathbf{s}) \left(1 - e^{-T_B(\mathbf{s})\sigma_{inel}^{NN}}\right) + \int d\mathbf{s}\, T_B(\mathbf{s}-\mathbf{b}) \left(1 - e^{-T_A(\mathbf{s})\sigma_{inel}^{NN}}\right), \tag{4.4}$$

$$N_{coll}(\mathbf{b}) = \int d\mathbf{s}\, T_A(\mathbf{s}) T_B(\mathbf{b}-\mathbf{s})\, \sigma_{inel}^{NN} = T_{AB}(\mathbf{b})\, \sigma_{inel}^{NN}, \tag{4.5}$$

where the nuclear thickness function $T_A(\mathbf{b})$ and the nuclear overlap function $T_{AB}(\mathbf{b})$ are defined as

$$T_A(\mathbf{b}) = \int dz\, \rho_A(z, \mathbf{b}), \tag{4.6}$$

$$T_{AB}(\mathbf{b}) = \int d\mathbf{s}\, T_A(\mathbf{s}) T_B(\mathbf{b} - \mathbf{s}). \tag{4.7}$$

The resulting N_{part} and N_{coll} can then be used to estimate measurable quantities, e.g., charged hadron multiplicity. Fig. 4.2 shows the Glauber fit for particle multiplicity estimation, which uses a combination of N_{coll} and N_{part} together with a negative binomial distribution. The ALICE measurement is well-described by the Glauber fitting function. In Table 4.2, charged particle multiplicity at mid-rapidity $|\eta| < 0.5$, averaged N_{part}, and multiplicity per participant pair are listed for four centrality bins.

4.1.2 Time evolution of heavy-ion collisions

The illustration of different stages of heavy-ion collisions is shown in Fig. 4.3 in time versus beam-direction coordinates. The time evolution of heavy-ion collisions can be broadly decomposed into three distinct stages; the initial stage, the QGP phase, and the hadron gas phase. Detailed descriptions of each stage are provided as follows:

- **Initial stage of the collisions**

  While the two nuclei penetrate through each other, the participants undergo nucleon-nucleon inelastic scattering and initial-state radiation, creating a large number of highly excited partons. As a consequence, a large amount of energy is deposited into the colliding zone. The newly created medium is in a pre-equilibrium stage and approaches local thermal equilibrium through frequent collisions among the constituents of the medium. Highly energetic particles, referred to as jets, are also produced at this stage through large-x scatterings. The random impact parameter b of the collisions produce fluctuating eccentricities in the transverse plane of the

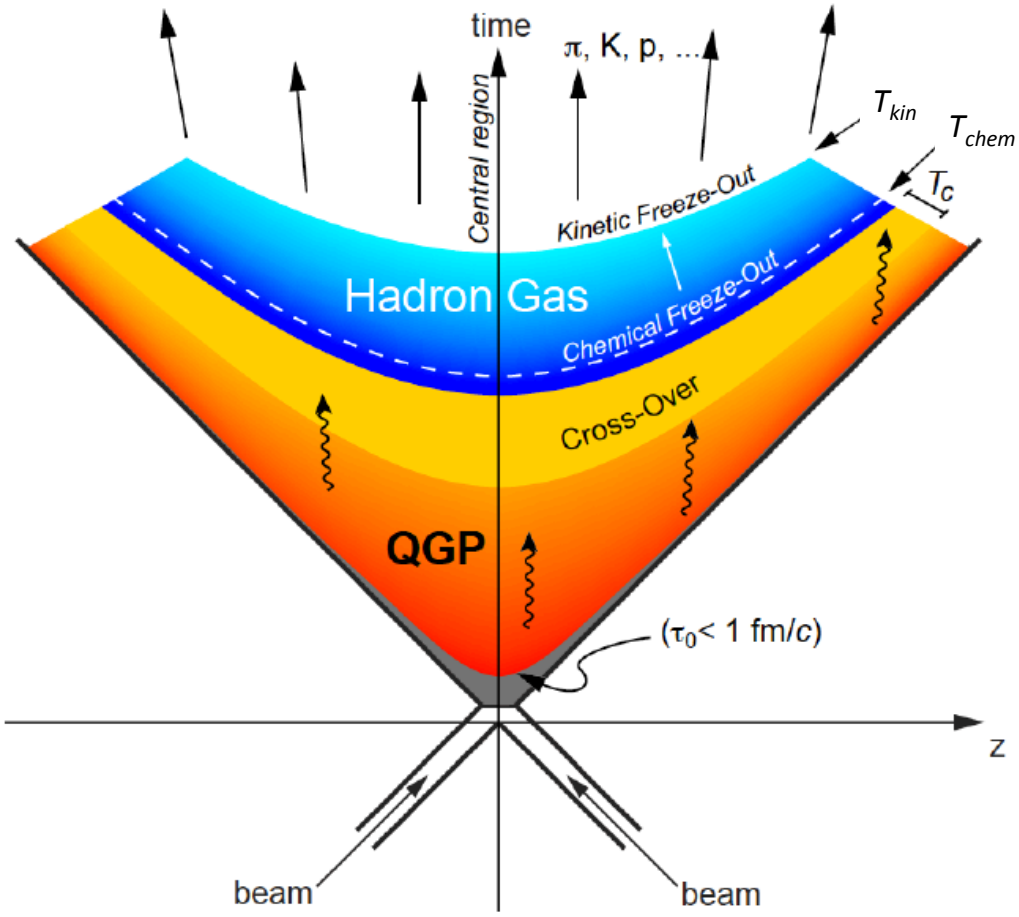

Figure 4.3: Schematic diagram of different stages of heavy-ion collisions in time versus beam-direction coordinates. This illustrates two relativistic heavy-ions colliding and undergoing the pre-equilibrium phase (grey), the QGP phase (red), and the hadron gas phase (blue). The phase transition temperature T_c with broad cross-over is represented as a yellow area. The chemical freeze-out and kinetic freeze-out at the hadronic phase are also shown. This figure is reproduced from [90].

overlap zone. Understanding the initial geometry is necessary to interpret the experimental results from the collisions. The actual overlap time of the two Lorentz contracted nuclei is $\tau = 2R/\gamma$, but the thermalization time τ_0 widely used for modelling heavy-ion collisions is a few tenths of fm, e.g., $\tau_0 \sim 0.6$ fm for $\sqrt{s_{NN}} = 2.76$ TeV Pb+Pb collisions, because of the size of the mean free path λ_{mfp}.

- **QGP in thermal equilibrium**

  The temperature of the system is sufficiently high that the nucleons are decomposed into colour-deconfined quarks and gluons. Moreover, due to the high density of the medium and small mean free path λ_{mfp} compared to the size of the system, partons in the medium quickly establish thermal equilibrium and exhibit collective behaviour. Collective motion of the QGP is well described by relativistic hydrodynamics, which uses the QCD equation of state as an input of the calculations. Because the QGP is colour opaque, coloured hard probes created at the early stage such as jets experience energy loss while penetrating the QGP – jet quenching. Measurements of the survived jets allow us to constrain the properties of the QGP. As the system evolves, thermal pressure toward the surrounding vacuum forces the QGP to undergo collective expansion and cooling.

- **Freeze-out in hadronic phase**

  When the system cools down below the transition temperature T_c, the thermalized partons start to form colour-neutral hadrons. Even after the QGP turns into hadronic matter, the constituent hadrons continue to collide with each other, keeping the local equilibrium of the system. Meanwhile, unstable hadrons in excited states decay into stable hadrons – resonance decay. Once all hadrons are in a stable state, the production yields of the particles are frozen, while elastic collisions may still occur. The corresponding temperature is called the chemical freeze-out temperature. Hadronic re-scattering persists until kinetic freeze-out. The species and energy-momentum after kinetic freeze-out remain unchanged until they are detected in detectors.

Notably, the QGP created in heavy-ion collisions is substantially dense and strongly interacting so that the system is quickly thermalized. The thermodynamic pressure generated by the QGP leads to collective expansion of the system. The collective behaviours observed in heavy-ion collisions are thus a signature of the QGP created in the collisions.

Another important tool to probe the creation of the QGP is energetic particles created at the initial stage of the collisions. Hard probes are created before the formation of the QGP and possess a full history of interactions with the QGP. The suppression of high transverse momentum (p_T) hadrons is a well-known phenomenon in heavy-ion collisions to be used to study the QGP.

In the following sections, we will discuss the two phenomenological signatures of the QGP created in heavy-ion collisions. In Sec. 4.2, collectivity observed in heavy-ion collisions and supporting observables will be presented. Also, we will briefly introduce relativistic hydrodynamics that provides theoretical descriptions of the thermalized QCD matter. Sec. 4.3 will talk about the production of hard probes and their suppression observed in heavy-ion collisions.

4.2 Collectivity

The QGP droplets produced at the RHIC and the LHC reach temperatures $T/T_c \sim 3$. The running coupling constant α_s at this scale is still large enough $\sim \mathcal{O}(1)$ that the created QGP behaves like an almost perfect fluid, so-called strongly coupled QGP (sQGP). As a consequence, the system is quickly thermalized after the collisions. The thermalized system feels the thermodynamic pressure, causing collective expansion of the system. The collective behaviour observed at non-central collisions is one of the key findings supporting the hypothesis that the strongly-interacting QGP is created in the colliding systems. This arises from the pressure gradient due to the spatial anisotropy of the colliding area in the transverse plane. The resulting anisotropic flow is highly correlated with the initial geometry of the collisions and has a large influence on the final-state particle production.

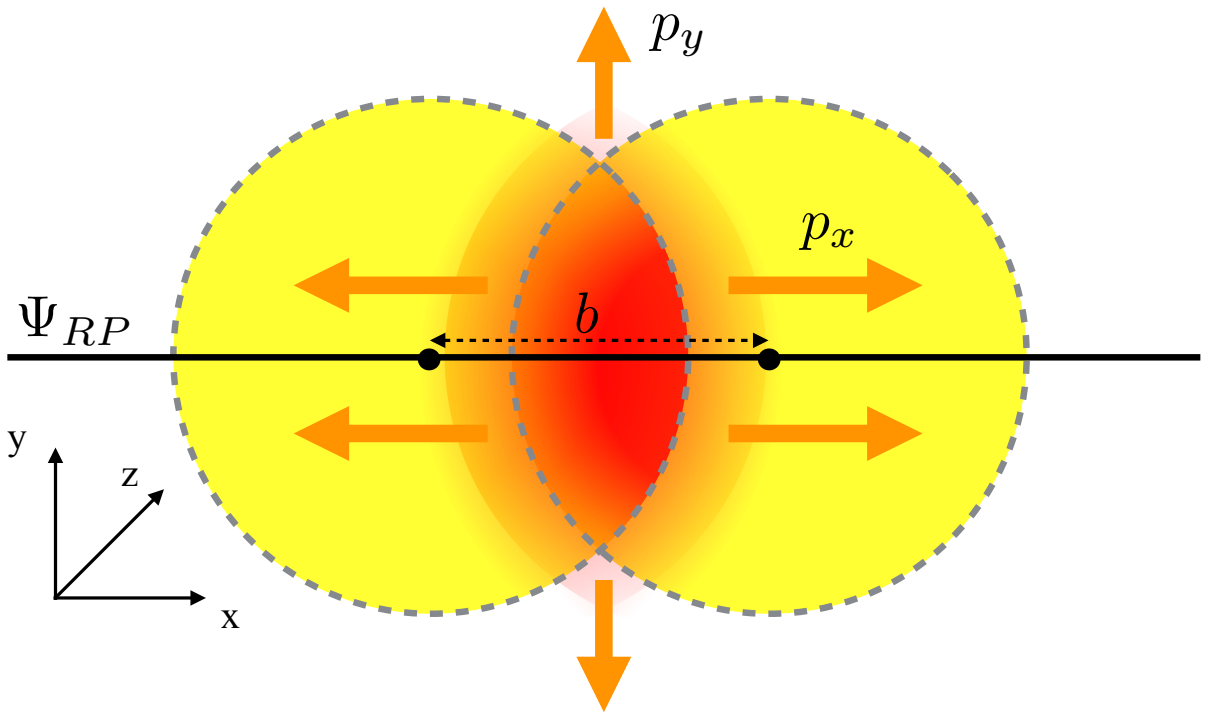

Figure 4.4: A cross-sectional view of two heavy ions colliding with a non-zero impact parameter b. The anisotropic shape of the overlap zone with respect to the reaction plane produces pressure gradients in momentum space and momentum anisotropy of particle production.

A convenient way of characterizing anisotropic flow is to use a Fourier expansion of the differential distribution of the invariant particle yield[2],

$$E\frac{d^3N(p_T,\phi)}{d^3\mathbf{p}} = \frac{d^2N(p_T,\phi)}{2\pi p_T dp_T dy}\left(1+2\sum_{n=1}^{\infty}\left[x_n\cos(n\phi)+y_n\sin(n\phi)\right]\right), \tag{4.8}$$

[2]The factor d^3p/E is a Lorentz invariant quantity. The proof of this can be found, for example, in [91].

where E and $\mathbf{p}$ are the energy and 3-momentum of the particle. The rapidity[3] y is defined by

$$y = \frac{1}{2} \ln \frac{E + p_z}{E - p_z}, \tag{4.10}$$

and ϕ is the azimuthal angle of the particle. With the following replacements,

$$x_n = v_n \cos(n\Psi_{RP}), \tag{4.11}$$

$$y_n = v_n \sin(n\Psi_{RP}), \tag{4.12}$$

Eq. (4.8) becomes

$$E\frac{d^3N(p_T,\phi)}{d^3\mathbf{p}} = \frac{d^2N(p_T,\phi)}{2\pi p_T dp_T dy}\left(1 + 2\sum_{n=1}^{\infty} v_n \cos\left[n(\phi - \Psi_{RP})\right]\right), \tag{4.13}$$

where Ψ_{PR} is defined as the reaction plane angle containing the impact parameter $\mathbf{b}$ and the beam axis. The azimuthal anisotropy is usually quantified by the coefficients of the Fourier expansion v_n in Eq. (4.13),

$$v_n(p_T, y) = \langle \cos\left[n(\phi - \Psi_{RP})\right] \rangle, \tag{4.14}$$

where the angular brackets denote an average of all particles in a event and all events in a given p_T and y bin. Since the reaction plane angle Ψ_{RP} is not experimentally measurable, the coefficients of anisotropic flow are estimated from azimuthal correlations between the measured particles [92].

The anisotropic flow coefficients v_n, especially the elliptic flow coefficient v_2, have centrality dependence since the initial geometry influences the pressure gradients. An

[3] In experiments, it is convenient to use pseudorapidity,

$$\eta = -\log\left[\tan\left(\frac{\theta}{2}\right)\right], \tag{4.9}$$

since it only requires the polar angle θ in momentum space relative to the beam direction. In the limit, $p \gg m$, pseudorapidity is often a standard proxy for rapidity.

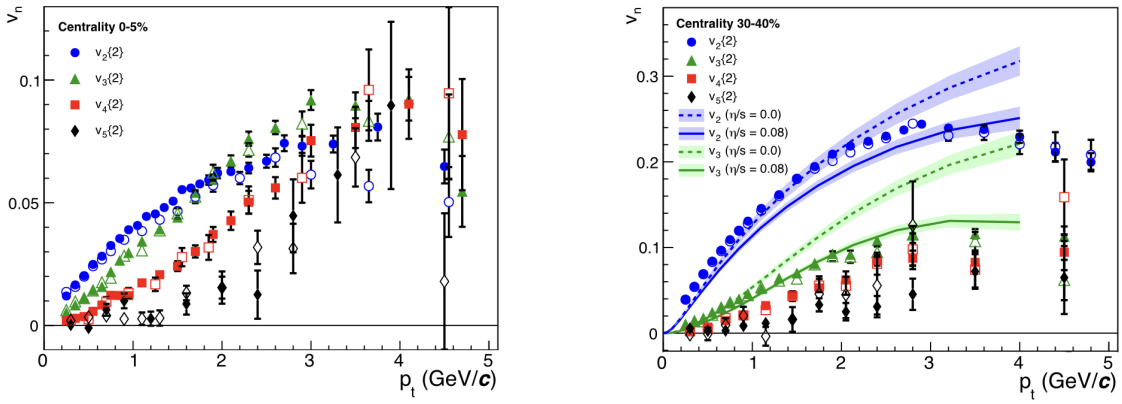

Figure 4.5: ALICE measurements of the p_T differential anisotropic flow coefficients v_n obtained from the two-particle correlation method measured in $\sqrt{s_{NN}} = 2.76$ TeV Pb+Pb collisions in the 0-5% (left panel) and 30-40% (right panel) centrality bins [93]. The full and open symbols represent the minimum distance between a pair of particles in a unit of the rapidity of $\Delta y > 0.2$ and $\Delta y > 1.0$, respectively. Theoretical calculations using hydrodynamics [94] are compared on the right. The hydrodynamic calculations are in fairly good agreement with the measurements.

example of a non-central collision is shown in Fig. 4.4. The anisotropic almond shape of the overlap zone with respect to the reaction plane develops a large elliptic flow coefficient v_2. Fig. 4.5 shows the p_T differential anisotropic flow coefficients v_n with $n = 1, 2, 3,$ and 4 obtained from the two-particle azimuthal correlation method in $\sqrt{s_{NN}} = 2.76$ TeV Pb+Pb collisions measured by ALICE. The magnitude of the elliptic flow coefficient v_2 measured in the 30-40% centrality bin (right panel) is greater than that measured in the 0-5% centrality bin (left panel) due to the large anisotropy in the initial geometry. However, the higher-order anisotropic flow coefficients show a weak dependence on centrality. The theoretical results shown in the right panel were provided by hydrodynamic simulations of the QGP [94], which agree fairly well with the measurements. In the following subsection, we will briefly discuss hydrodynamic modelling of the thermalized system and its success in describing the QGP.

4.2.1 Hydrodynamics

The illustration of a system with many degrees of freedom is, in general, a challenging problem in theoretical physics. However, it is possible to describe many-body systems using an effective macroscopic picture. Relativistic hydrodynamics [95–97] provides a theoretical tool to describe the system in which quarks and gluons are thermalized. This alternative prescription of the QGP has been successful in explaining collective phenomena arising in heavy-ion collisions [98–104].

The applicability of hydrodynamics can be quantified by the Knudsen number $K_N \sim l/L$ [105], the ratio of the relevant microscopic scale l to the macroscopic scale L. In the case of heavy-ion collisions, the microscopic scale l is the mean free path λ_{mfp} of the scatterings between deconfined quarks and gluons and the macroscopic scale L is the size of the QGP. Generally, hydrodynamics becomes applicable when the Knudsen number is sufficiently smaller than unity, $K_N \ll 1$.

Hydrodynamic modelling assumes that the system is in local thermal equilibrium. Although in the hydrodynamic approach, detailed microscopic dynamics are not necessary, it indeed requires the QCD equation of state of the given system relating pressure p, energy density ϵ, and baryon density n. The basic hydrodynamic equations describe conservation of current and energy-momentum,

$$\partial_\mu N^\mu = 0, \tag{4.15}$$

$$\partial_\mu T^{\mu\nu} = 0. \tag{4.16}$$

In Eq. (4.15), N^μ is the four-vector currents of the baryon, which is equal to nu^μ in the ideal fluid case. For viscous hydrodynamics, it is necessary to include an additional term for the diffusion currents nq^μ. With the fluid velocity $\mathbf{v}$, the four-velocity $u^\mu(u^0, \mathbf{u})$ is defined

by

$$u^0 = \frac{1}{\sqrt{1-\mathbf{v}^2}}, \tag{4.17}$$

$$\mathbf{u} = \frac{\mathbf{v}}{\sqrt{1-\mathbf{v}^2}}, \tag{4.18}$$

which satisfies $u^\mu u_\mu = 1$. The energy-momentum tensor $T^{\mu\nu}$ shown in Eq. (4.16) is decomposed into the 4-momentum and the associated current as follows:

- T^{00} is the energy density
- T^{i0} is the energy flux along axis i.
- T^{0j} is the density of the j^{th} component of momentum with $j = 1, 2, 3$.
- T^{ij} is the flux along axis i of the j^{th} component of momentum.

For ideal fluids, $T^{\mu\nu}$ in the local rest frame can be expressed as

$$T^{\mu\nu} = (\epsilon + p)u^\mu u^\nu - pg^{\mu\nu}, \tag{4.19}$$

where $u^\mu = (1, 0, 0, 0)$ in the local rest frame of the fluid and $g^{\mu\nu} = \text{diag}(1, -1, -1, -1)$ is the Minkowski metric tensor.

Ideal hydrodynamics assumes that each fluid element is homogeneous and local equilibrium is always maintained during the evolution. Although it is natural to employ ideal hydrodynamics as an application to the QGP, almost all fluid in nature involves dissipative effects. The Müller-Israel-Stewart (MIS) [106–108] and Denicol-Niemi-Molnar-Rischke (DNMR) [109–111] theories provide a proper description of second-order viscous hydrodynamics in a gradient expansion. Since the plasma is no longer assumed isotropic, one needs to include corrections proportional to gradients such as the shear viscosity η and the bulk viscosity ζ. It turned out that the magnitudes of the anisotropic flow v_n are quite sensitive to the viscosity of the plasma as shown in Fig. 4.5. Thus, estimating the values of shear and bulk viscosity has been an important aspect of the hydrodynamic

modelling of the QGP. Throughout this thesis, we will employ the results of second-order viscous hydrodynamic simulations obtained by MUSIC [100] to study jet energy loss in the QGP created in heavy-ion collisions.

4.3 Hard probes

As mentioned in the previous chapter and Sec. 4.1, energetic particles created at the first moment of heavy-ion collisions are commonly referred to as jets. Since they propagate through the droplet of QGP produced in the same collision, they are considered as key probes of the QGP. They are created via hard processes involving large momentum exchanges. According to the QCD factorization theorem, those processes can be described as the convolution of different contributions to the cross-section. For example, the cross-section for final state single hadron production at proton-proton collisions is formulated as [112]

$$d\sigma_{pp\to hX} \approx \sum_{abj} \int dx_a \int dx_b \int dz_j f_{a/p}(x_a, \mu_f) \otimes f_{b/p}(x_b, \mu_f) \otimes d\sigma_{ab\to jX}(\mu_f, \mu_R) \otimes D_{j\to h}(z_j, \mu_F), \tag{4.20}$$

where $f_{a/p}(x_a, \mu_f)$ are the parton distribution functions of the parton a with momentum fraction of x_a from the colliding proton. Similarly, $f_{b/p}(x_b, \mu_f)$ is the PDF of the parton b with x_b from the other proton. $d\sigma_{ab\to jX}(\mu_f, \mu_R)$ is the cross-section of a $2 \to 2$ scattering between parton a and b, producing a parton j and residual X. $D_{j\to h}(z_j, \mu_F)$ is the fragmentation function for the parton j to the final-state hadron h with momentum fraction z_j. The factorization scale μ_f, μ_F and the renormalization scale μ_R are typically taken to be a relevant energy scale Q such as the hadron p_T. The PDFs can be obtained by a global fit of data measured by multiple experiments, e.g., deep inelastic scatterings (DIS) and proton-proton collisions. As an example, Fig. 4.6 shows an overview of CTEQ6 [113] PDFs at interaction scale $Q = 2$ GeV and $Q = 100$ GeV.

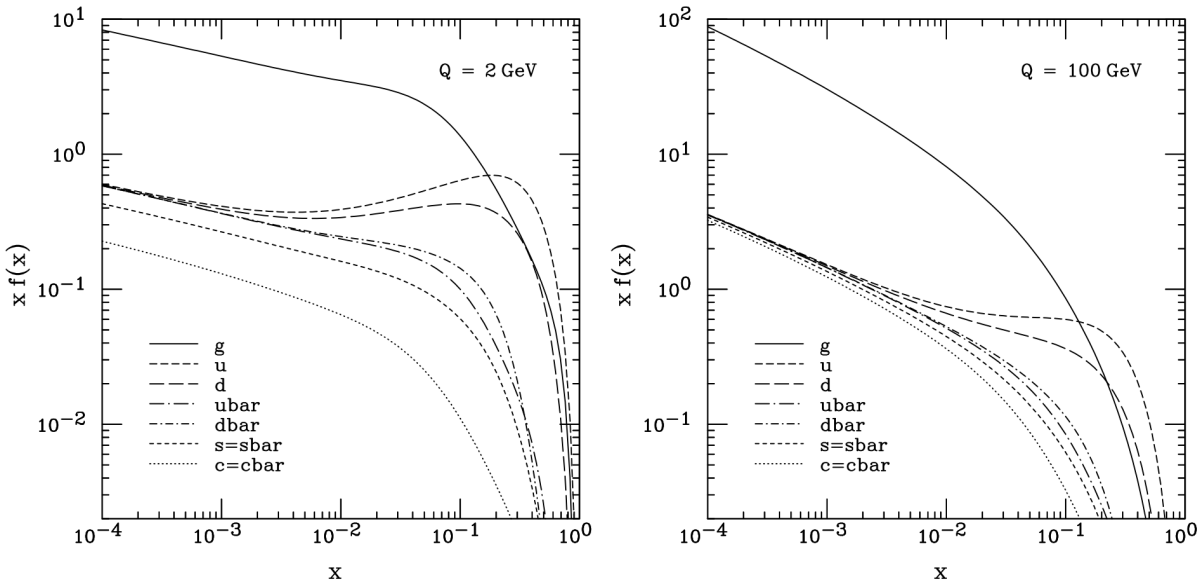

Figure 4.6: CTEQ6 parton distribution function (PDFs) as a function of momentum fraction x at $Q = 2$ GeV (left) and $Q = 100$ GeV (right) [113].

The initial hard scattering encoded in $d\sigma_{ab\to jX}$ is a $2 \to 2$ partonic elastic scattering process at leading order in strong coupling constant α_s. The scattered partons are energetic and highly virtual, i.e., squared momentum transfer Q^2 is large. Since high-virtuality particles are unstable, they reduce their virtuality by parton branching processes. The parton splittings are described by the Altarelli-Parisi splitting functions shown in Table. 3.1. The partons produced by multiple splitting are then hadronized around the transition temperature T_c.

Proton-proton collisions provide a clean environment in which the parton evolution is well-described by the DGLAP equations and the underlying events (UE) produced by subordinate interactions are negligible. In heavy-ion collisions, however, the creation of the QGP extensively modifies the evolution of jets, resulting in suppression of high-energy hadron production. In the following subsection, we will address the theoretical approaches to the jet quenching phenomenon and available data measured by experiments.

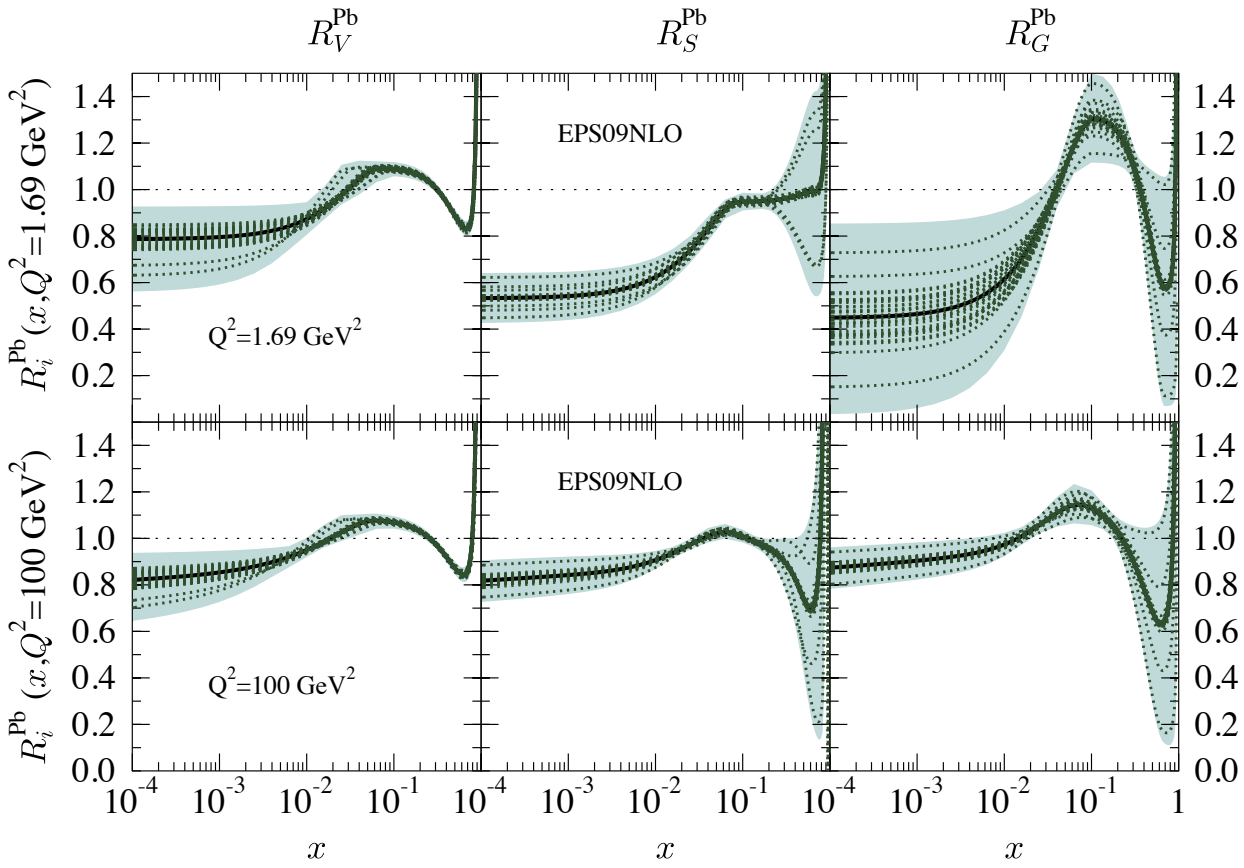

Figure 4.7: The modification factors R_a^A for Pb nuclei. From left to right, R_a^A of valence quarks, sea quarks, and gluons are presented at the scale $Q^2 = 1.69$ GeV^2 (top panel) and $Q^2 = 100$ GeV^2 (bottom panel). Experimental data from deep inelastic l+A scattering, Drell-Yan dileption production in p+A collisions and pion production in d+Au and p+p collisions at RHIC were used for the global parameter fitting [121]. The black lines represent the best-fit results, while the dotted green curves indicate the error sets. The shaded green bands are uncertainties.

4.3.1 Jet quenching

Jet quenching in heavy-ion collisions is a well-established phenomenon for coloured hard probes such as light quarks and gluons. This has been extensively measured experimentally [114–116] and calculated theoretically [1, 117–120]. The purpose of the jet quenching study is to provide evidence of QGP creation in the colliding system and to understand mechanisms of jet-medium interactions.

When studying jet quenching in heavy-ion collisions, one needs to consider two nuclear effects which lead to the modification of final-state hadron production. One is the nuclear PDFs (nPDF) [122, 123]; the nuclear structure in nuclei are different from the superposition of their constituent nucleons due to initial state nuclear effects. This is often referred to as the cold nuclear matter (CNM) effect or nuclear PDF effects. The modification of the PDFs in a nucleus A is represented by $R_a^A(x, Q^2)$, the ratio of the density function of a parton a in a nucleus A $f_{a/A}(x, Q^2)$ to that in a proton $f_{a/p}(x, Q^2)$

$$R_a^A(x, Q^2) = \frac{f_{a/A}(x, Q^2)}{f_{a/p}(x, Q^2)}. \tag{4.21}$$

Similar to PDFs, the nuclear PDFs are obtained by the global fit analyses using collision experiments such as DIS, p+A, and d+A collisions [124–133]. Several parameter fitting analyses of the nuclear PDFs are currently available [121, 134, 135]. Fig. 4.7 shows the EPS09 [121] nPDF for valence quarks, sea quarks, and gluons for Pb nuclei at $Q^2 = 1.69$ GeV^2 and $Q^2 = 100$ GeV^2. The behaviour of $R_a^A(x, Q^2)$ shown in Fig. 4.7 can be divided into four regions [136],

- $R_a^A > 1$ for $x \lesssim 0.8$: Fermi motion effects [137, 138]
- $R_a^A < 1$ for $0.2 \lesssim x \lesssim 0.8$: the European Muon Collaboration (EMC) effects [125, 139–141]
- $R_a^A > 1$ for $0.04 \lesssim x \lesssim 0.2$: the anti-shadowing region
- $R_a^A < 1$ for $x \lesssim 0.04$: the shadowing region

Detailed discussion on shadowing and anti-shadown can be found in [142–167].

Another important effect is due to the colour opacity of the QGP created in heavy-ion collisions. This leads to significant suppression of final-state hadron production via jet-medium interactions. While energetic partons propagate through the QGP medium, they interact with the constituents of the medium elastically and inelastically, transporting their energy to the surrounding background. Multiple $2 \to 2$ scatterings between a hard

parton and a constituent parton in the QGP cause the exchange of momentum, increasing virtuality for each parton. Then virtual partons tend to reduce their virtuality by radiating additional partons. These processes modify the vacuum splitting functions in Table 3.1, resulting in energy loss of energetic partons. There are a number of parton energy loss approaches developed and studied, namely those of Baier-Dokshitzer-Mueller-Peigne-Schiff-Zakharov (BDMPS-Z) [168–170], Gyulassy-Levai-Vitev (GLV) [171–173], Amesto-Salgado-Wiedemann (ASW) [174, 175], higher twist (HT) [176–178], and Arnold-Moore-Yaffe (AMY) [179–182].

The jet quenching effect is quantified by the nuclear modification factor R_{AA}, i.e. the ratio of high p_T particle production in nucleus-nucleus (AA) collisions compared to that in pp collisions. One may define the nuclear modification factor R_{AA}

$$R_{AA}(p_T) = \frac{1}{\langle N_{coll} \rangle} \frac{d^2 N_{AA}(p_T)/dp_T d\eta}{d^2 N_{pp}(p_T)/dp_T d\eta}, \tag{4.22}$$

where the averaged number of binary nucleon-nucleon (NN) collisions $\langle N_{coll} \rangle$ is a proper normalization at a given centrality class of AA collisions calculated from the Glauber model. N_{AA} and N_{pp} represent the final state particle yield per event in AA and pp collisions, respectively. For AA collisions behaving as a simple superposition of N_{coll} binary collisions, the nuclear modification factor R_{AA} would be unity. However, many experiments observed strong suppression of high p_T charged hadrons at central heavy-ion collisions at the RHIC and the LHC as shown in Fig. 4.8. Their measurements, together with multiple theoretical approaches, support that the QGP created in heavy-ion collisions induces jet quenching.

4.4 Summary

In this chapter, a brief review of relativistic heavy-ion collisions was discussed. The study of heavy-ion collisions has been a prominent application of the theory of QCD. Moreover,

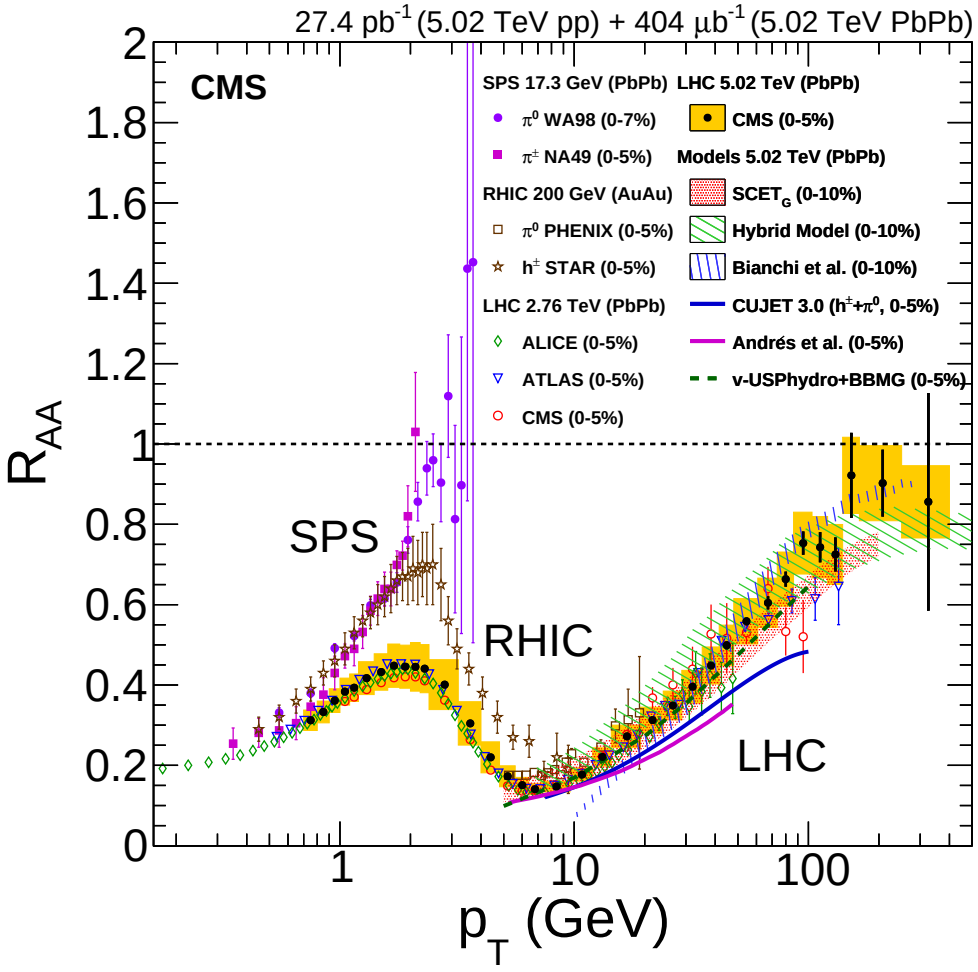

Figure 4.8: Measurements of the nuclear modification factor R_{AA} in central heavy-ion collisions at various centre-of-mass energies and colliding systems measured by the SPS, the RHIC, and the LHC [183–190], compared to predictions of six models for $\sqrt{s_{NN}} = 5.02$ TeV Pb+Pb collisions from [191–196]. The strong suppression pattern over the broad range of p_T observed at the measurements shows the QGP creation in heavy-ion collisions, which is also supported by the theoretical calculations. The figure is taken from [197].

the creation of the QGP in experimental heavy-ion programs is a remarkable success in studying the extreme environment that existed shortly after the Big Bang. This chapter addressed the two important pieces of evidence of the QGP creation in heavy-ion collisions: collective motions and jet quenching observed in measurements. A theoretical approach to studying jet quenching will be presented in Ch. 5 in detail.

Part II

Study of jet quenching in heavy-ion collisions

Chapter 5

MARTINI: Theoretical modelling of jet quenching

The phenomenological study of jet quenching in heavy-ion collisions is a challenging task. This is mainly because it requires adequate modelling of a variety of aspects of the collisions in which different scales are involved. The relevant aspects include:

- the initial hard scattering for jet production
- a realistic description of the QGP evolution
- a theoretical prescription for jet energy loss in the QGP
- a modelling of phase transition at the transition temperature T_c.

As mentioned in Sec. 4.3, jet production in the initial stage and subsequent propagation in the medium involving large momentum scales may be studied within the framework of perturbative QCD. In the parton shower language, e.g., Eq. (4.20), one has to deal with measured probabilities to find a parton with specific scales in the parton distribution function or to find a hadron from a given fragmentation function (FF). The Monte-Carlo method is well-suited for simulating systems with probability distributions and large uncertainties. The probabilistic nature of the parton shower is well realized by Monte-Carlo

event generators and a variety of parton shower event generators exist, e.g., PYTHIA [198], HERWIG++ [199], ISAJET [200], and SHERPA [201].

While those event generators are quite successful in describing parton showers in relativistic high-energy particle collisions, their focus is mainly on the lepton and nucleon collisions where clearly there is lack of creation of the QGP and jet-QGP interaction[1]. The major purpose of Monte-Carlo event generators for heavy-ion collisions is to explore jet quenching, which clearly dictates the creation of QGP, and to extract properties of the QGP. Most heavy-ion event generators are developed based on those for binary collisions and provide their own theoretical prescriptions to simulate jet evolution in the QGP.

This chapter introduces the Monte-Carlo event generator for heavy-ion collisions, MARTINI (**M**odular **A**lgorithm for **R**elativistic **T**reatment of heavy **I**o**N** **I**nteractions) [1]. In Sec. 5.1 general concepts and descriptions of MARTINI will be presented. MARTINI utilizes key components of PYTHIA [202] and its core lies in jet energy loss processes. Detailed descriptions of the jet energy loss models, i.e., the AMY radiative formalism, and collision and conversion processes, are discussed in Sec. 5.2. Sec. 5.3 covers my original work to develop the MARTINI model and to establish more realistic environments for jet quenching in heavy-ion collisions. Sec. 5.4 provides the detailed program flow in MARTINI and Monte-Carlo implementation of the theoretical models. The summary of this chapter is presented in Sec. 5.5.

5.1 Introduction to MARTINI

MARTINI [1] is a Monte-Carlo event generator for relativistic heavy-ion collisions. MARTINI simulates time-ordered jet evolution in the presence of the evolving QGP background. The evolution of the momentum distribution $P_a(p)$ for a given parton a of momentum p propagating through a QGP medium is governed by a set of coupled rate

[1]There have been attempts to encapsulate heavy-ion modules in PYTHIA [202], namely Angantyr, although rigorous simulations of the QGP sector using hydrodynamics is not provided.

equations,

$$\frac{dP_q(p)}{dt} = \int_k P_q(p+k)\frac{d\Gamma^q_{qg}(p+k,k)}{dkdt} - P_q(p)\frac{d\Gamma^q_{qg}(p,k)}{dkdt} + 2P_g(p+k)\frac{d\Gamma^g_{qq}(p+k,k)}{dkdt}, \tag{5.1}$$

$$\frac{dP_g(p)}{dt} = \int_k P_q(p+k)\frac{d\Gamma^q_{qg}(p+k,p)}{dkdt} + P_g(p+k)\frac{d\Gamma^g_{gg}(p+k,k)}{dkdt} - P_g(p)\left(\frac{d\Gamma^g_{qq}(p,k)}{dkdt} + \frac{d\Gamma^g_{gg}(p,k)}{dkdt}\theta(2k-p)\right), \tag{5.2}$$

where $P_a(p)$ is the probability of finding a parton a of momentum p with a being either a quark (anti-quark) or a gluon. $d\Gamma^a_{bc}(p,k)/dk$ is the transition rate of a parton a of momentum p emitting a parton c of momentum k and becoming a parton b. In the last term of Eq. (5.1), $\Gamma^g_{qq}(p+k,k)$ represents either $\Gamma^g_{q\bar{q}}(p+k,k)$ and $\Gamma^g_{\bar{q}q}(p+k,k)$. The factor of 2 takes into account that q and $\bar{q}$ are distinguishable. However, this factor is not present in the transition $\Gamma^g_{gg}(p+k,k)$ as shown in Eq. (5.2), since the two outgoing gluons are identical. The θ function in Eq. (5.2) prevents double-counting of the final states. The integration includes $k < 0$, which represents the energy gain of the parton a from the background medium.

The transition rate $\Gamma(p,k)$ encodes the $1 \to 2$ AMY radiative energy loss rates [179–182] incorporated in MARTINI. The $2 \leftrightarrow 2$ collisional transition rates [203] and the conversion rates [1] are also implemented in a similar manner. The theoretical descriptions of the jet energy loss processes are presented in detail in the next section. The evolving QGP background is simulated by MUSIC [100], a (3+1) dimensional viscous hydrodynamic model. The initial conditions of the hydrodynamic simulations are provided by either the Monte-Carlo Glauber model [87] or the IP-Glasma model [3].

MARTINI solves the coupled parton evolution equations Eq. (5.1) and Eq. (5.2) using Monte-Carlo methods. Every hard parton evolves individually and randomly undergoes transition processes. The probabilistic parton evolution averaged over a large number of independent events yields a reasonable and reliable solution for the evolution equations.

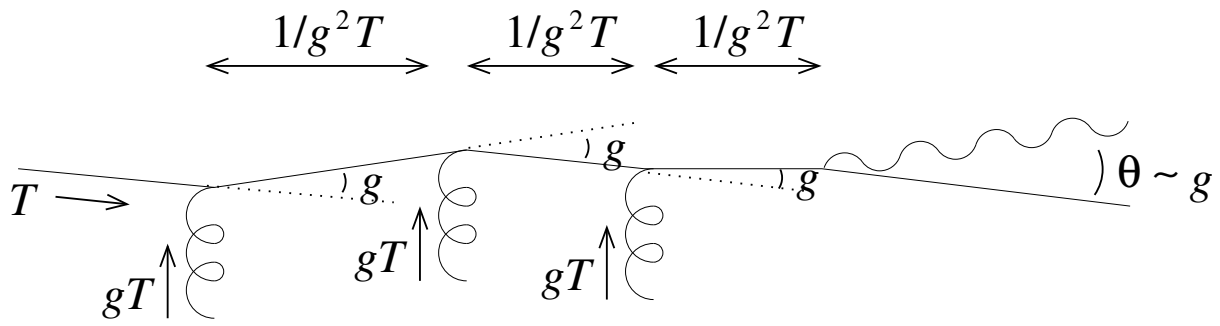

Figure 5.1: A diagram of typical parton interaction involving multiple elastic collisions between hard and thermal partons and additional gluon radiation. The orders of magnitude of various scales associated with each process are also shown. The figure is reproduced from [181].

The modular structure of MARTINI allows users to include or omit certain processes independently in the simulations. MARTINI also provides flexibility to choose different models such as different initial state and hydrodynamics models. The interface for setting parameters in MARTINI is identical to that of PYTHIA and adding or modifying parameters is also straightforward.

In the following section, we will discuss the jet energy loss processes implemented in MARTINI and their theoretical background.

5.2 Jet energy loss models

Gluon radiation and elastic scattering are regarded as the processes that lead to jet quenching in heavy-ion collisions. In the following subsections, we introduce the AMY radiative energy loss formalism [179–182], and the collisional energy loss model [203]. These two independent models are incorporated in the MARTINI framework to provide realistic descriptions of jet energy loss.

typical particle momentum p, k	T
typical momentum transfer q Debye screening mass m_D	gT
typical scattering angle θ typical radiation angle θ	g
mean free path: small angle scattering $(\theta \sim g, q \sim gT)$ formation time of collinear radiation $(\theta \sim g)$	$(g^2T)^{-1}$

Table 5.1: List of various parametric scales typically emerging in a weakly-coupled equilibrated QCD plasma.

5.2.1 AMY radiative formalism

The Arnold-Moore-Yaffe (AMY) [179–182] formalism is a finite-temperature field theory formulation of gluon radiation. The AMY formalism concerns a weakly-coupled and fully equilibrated QGP at asymptotically high temperature where perturbative QCD is applicable. A hierarchy of well-separated energy scales $g^2T \ll gT \ll T$ emergent in the pQCD regime facilitates a power counting analysis in the formalism.

One assumes a hard on-shell parton undergoing multiple elastic scatterings with thermal partons in the medium, emitting a gluon as illustrated in Fig. 5.1. The typical momenta of the participants of scattering is order T, the temperature scale. The momentum transfer q of an exchanged gluon is order gT, causing deflection angle of $\theta \sim g$. The mean free path between consecutive scatterings is order $(g^2T)^{-1}$, which is also the order of the formation time of gluon radiation. The radiation is nearly collinear, order of $\theta \sim g$. The relevant scales associated with elastic scattering and gluon radiation are summarized in Table 5.1[2].

LPM effect At high temperatures where $g(T) \ll 1$, the elastic collisions against plasma constituents are treated as instantaneous compared to the radiation processes. The time

[2]A detailed review of the scale estimation is given in Sec. I.B of Ref. [180].

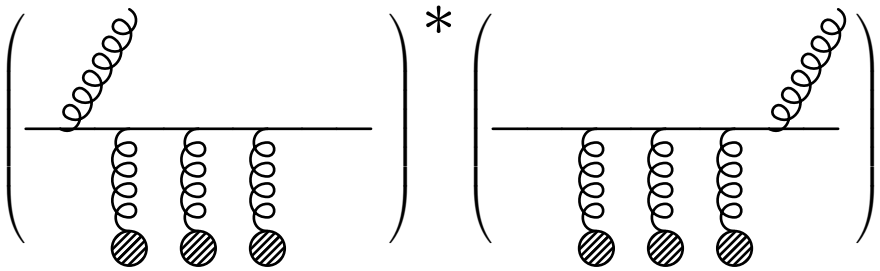

Figure 5.2: A typical interference term appearing in the square of multiple scattering amplitudes involving gluon emissions. A gluon may be radiated before and after consecutive scatterings against plasma constituents. In the LPM regime, this term contributes to the leading-order gluon emission rate.

for typical elastic scattering is estimated as $\tau \sim 1/m_D \sim (gT)^{-1}$ (See Table 5.1). However, the moment of a radiation process is not uniquely defined; this time scales like $t_f \sim (g^2T)^{-1}$ in the weakly-coupled plasma limit. This finite formation time of radiation is of the same order of magnitude as the mean free path λ_{mfp} between elastic scatterings as shown in Table 5.1. As a result, radiations induced by consecutive scatterings may not be treated as independent events due to coherence between multiple scattering events. This is known as the Landau-Pomeranchuk-Migdal (LPM) effect [204–206]. The LPM effect manifests as non-vanishing interference terms in the squared matrix element as shown in Fig. 5.2. Therefore, even in the perturbative QCD regime, one essentially considers resummation of all appropriate diagrams to obtain the leading-order gluon emission rate.

Fig. 5.3 shows a typical ladder diagram with contributions from the interference terms. The leading-order radiation rate requires a resummation of these diagrams with all possible number of gluon rungs. Note that the self-energy resummation on the top and bottom fermion propagators is implied[3]. Arnold, Moore and Yaffe rigorously evaluated the ladder diagrams of Fig. 5.3 via diagrammatic analysis and proved that only these diagrams are relevant to the leading-order gluon emission rate [181].

[3]The self-energy resummation emerges from the non-interfering terms in the squared diagram of all possible gluon radiations. See Fig. 14 in Ref. [181].

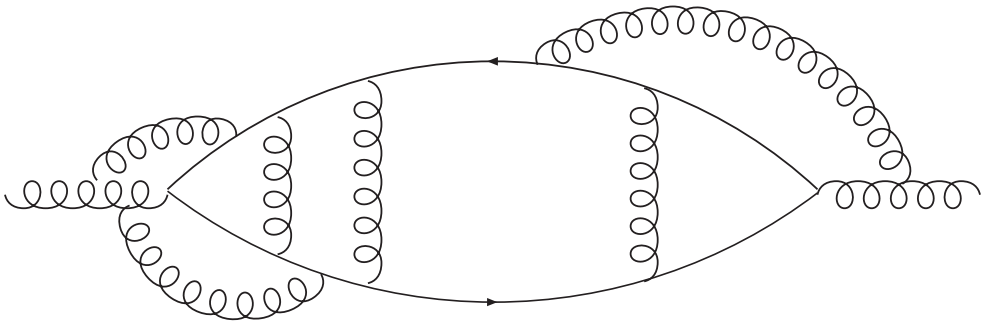

Figure 5.3: A generic gluon self-energy diagram contributing to the leading-order gluon radiation rate. The gluon propagators can be arbitrary attached in the diagram due to non-Abelian theory of QCD. Resummation of self-energy attached in the top and bottom fermion propagators is implied. The figure is taken from [207].

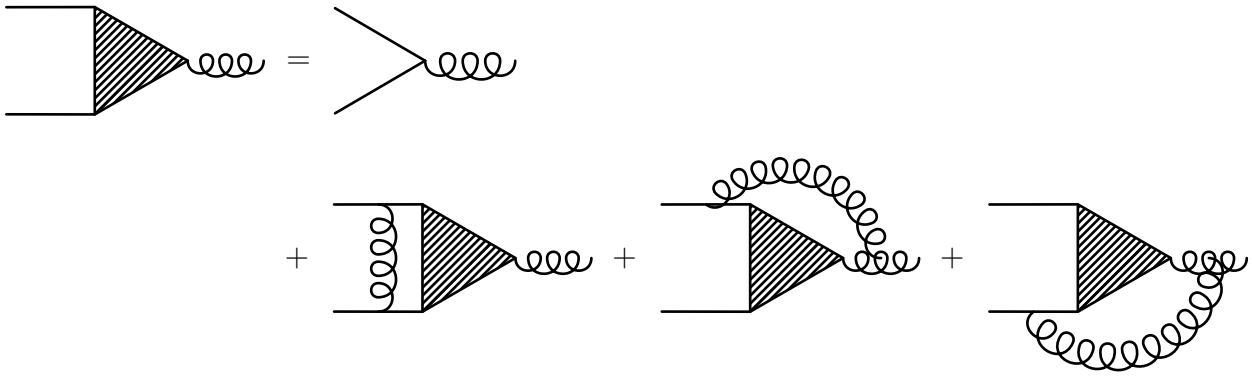

Figure 5.4: Diagrams of the Schwinger-Dyson equation for the gluon self-energy resummation in Eq. (5.3).

The resummed ladder diagrams can be expressed in terms of the Schwinger-Dyson type equation, where randomly attached gluons are classified into three groups. The diagrammatic representation of the Schwinger-Dyson type equation is illustrated in Fig. 5.4

The corresponding integral equation is given by [208]

$$2\mathbf{h} = i\delta E(\mathbf{h},p,k)\mathbf{F}(\mathbf{h}) + g^2T\int\frac{d^2\mathbf{q}_\perp}{(2\pi)^2}C(\mathbf{q}_\perp)\Big\{(C_R - C_A/2)[\mathbf{F}(\mathbf{h}) - \mathbf{F}(\mathbf{h}-k\mathbf{q}_\perp)] \\ + (C_A/2)[\mathbf{F}(\mathbf{h}) - \mathbf{F}(\mathbf{h}+p\mathbf{q}_\perp) \\ + (C_A/2)[\mathbf{F}(\mathbf{h}) - \mathbf{F}(\mathbf{h}-(p-k)\mathbf{q}_\perp)]\Big\}, \quad (5.3)$$

where $\mathbf{h} \equiv (\mathbf{k}\times\mathbf{p})\times\mathbf{e}_\parallel$ determines non-collinearity of the final states. A unit vector $\mathbf{e}_\parallel$ is fixed by convention as collinear with any of $\mathbf{p}$, $\mathbf{k}$, and $\mathbf{p}+\mathbf{k}$, where $\mathbf{p}$ and $\mathbf{k}$ are momenta of initial and radiated partons, respectively. $\delta E(\mathbf{h},p,k)$ is the energy difference between the initial and final states in the leading order,

$$\delta E(\mathbf{h},p,k) = \frac{\mathbf{h}^2}{2pk(p-k)} + \frac{m_k^2}{2k} + \frac{m_{p-k}^2}{2(p-k)} - \frac{m_p^2}{2p}, \quad (5.4)$$

where m_k^2 is the medium induced thermal mass of a parton carrying the momentum k. For each species, they are given by

$$m^2 = \begin{cases} m_D^2/2 & : \text{ gluon} \\ C_F g^2T^2/4 & : \text{ quark,} \end{cases} \quad (5.5)$$

where the Debye mass is [209]

$$m_D^2 = \frac{2N_c+N_f}{6}g^2T^2. \quad (5.6)$$

$C(\mathbf{q}_\perp)$ is the differential elastic cross-section to exchange transverse momentum $\mathbf{q}_\perp$. In the QCD medium, this value at leading order in the strong coupling is given by [209]

$$C(\mathbf{q}_\perp) = \frac{m_D^2}{\mathbf{q}_\perp^2(\mathbf{q}_\perp^2+m_D^2)}. \quad (5.7)$$

The three terms in the integral in Eq. (5.3) correspond to the second, third, and fourth terms in the right hand side of Fig. 5.4. They represent the three possible types of an

additional gluon propagator attached to the resummed gluon self-energy diagram. The quadratic Casimir is $C_R = C_F$ for the fundamental representation of a quark field and $C_R = C_A$ for the adjoint representation of a gluon field. The number of the colour states is $N_c = 3$ in $SU(3)$.

The solution of Eq.(5.3), $\mathbf{F}(\mathbf{h}, p, k)$, is the input of the radiative rates for various $2 \to 1$ processes, which are given by

$$\frac{d^2\Gamma(p,k,T)}{dpdk} = \frac{C_R g^2}{16\pi p^7} \frac{1}{1 \pm e^{-k/T}} \frac{1}{1 \pm e^{-(p-k)/T}} \times \left\{ \begin{array}{ll} \frac{1+(1-x)^2}{x^3(1-x)^2} & q \to qg \\ N_f \frac{x^2+(1-x)^2}{x^2(1-x)^2} & g \to q\bar{q} \\ \frac{1+x^4+(1-x)^4}{x^3(1-x)^3} & g \to gg \end{array} \right\} \times \int \frac{d^2\mathbf{h}}{(2\pi)^2} 2\mathbf{h} \cdot \mathrm{Re}\, \mathbf{F}(\mathbf{h}, p, k), \tag{5.8}$$

where $1/(1 \pm e^{-k/T})$ is the Pauli blocking or Bose enhancement factor for a final state parton of momentum k with positive sign for quarks (the Fermi-Dirac distribution) and a negative sign for gluons (the Bose-Einstein distribution). T is the local temperature of the QGP and the momentum fraction x is defined as $x \equiv k/p$. For the case of $q\bar{q}$-pair production $g \to q\bar{q}$, the prefactor $C_R - C_A/2$ should appear on the second term of the integral in Eq. (5.3). Additional photon radiation rates are also calculated analogously to the gluon radiation rates in Ref. [179, 181]. The results in Eq. (5.8) correctly reproduce both the Bethe-Heitler ($\lambda_{mfp} > t_f$) and the LPM ($\lambda_{mfp} < t_f$) limits.

Fig. 5.5 shows the AMY radiative rates in Eq. (5.8) versus the momentum of an initial parton (left) and the temperature of the QGP (right) for the different radiative processes, including photon radiation. The left picture in Fig. 5.5 shows the majority of radiation rates is contributed from gluon radiation ($q \to qg$ and $g \to gg$), while the $q\bar{q}$-pair creation and the photon radiation processes are suppressed by several orders of magnitude. The gluon radiation processes exhibit a monotonic dependence on the momentum of an initial hard parton, whereas the $q\bar{q}$-pair creation and the photon radiation rates moderately

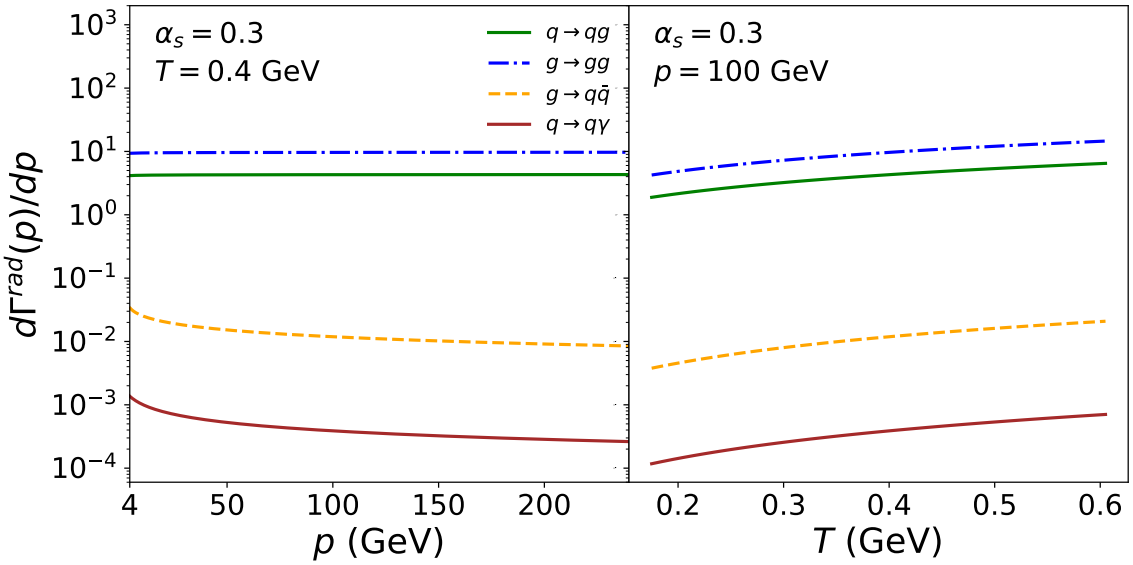

Figure 5.5: The AMY radiative rates in Eq. (5.8) as a function of momentum p of a hard parton (left) and of the temperature of the background medium (right). In each figure, four different radiative processes are plotted; $q \to qg$, $g \to gg$, $g \to q\bar{q}$, $q \to q\gamma$. The temperature in the left figure is set to $T = 0.4$ GeV and the initial momentum is set to $p = 100$ GeV. The strong coupling $\alpha_s = 0.3$ is used for both of the plots.

decrease at higher momentum. Fig. 5.5 (right) clearly indicates that all processes have increasing behaviour with temperature.

Double differential rates of the radiative processes are shown in Fig. 5.6. In each panel, the momenta of initial incoming partons are set to $p = 20$ GeV (left) and $p = 100$ GeV (right). The differential rates are non-zero since the k integration in Eq. (5.1) and Eq. (5.2) runs from $-\infty$ to ∞. The negative radiation can be understood as $2 \to 1$ absorption where a hard parton absorbs a thermal parton and gains its energy. However, photon absorption is neglected since photons interact electromagnetically and its interactions are much weaker than strong interactions. The distribution of radiated momentum for the two gluon emission processes has a peak at $k \sim 0$, indicating that radiation is dominated by soft gluon radiation.

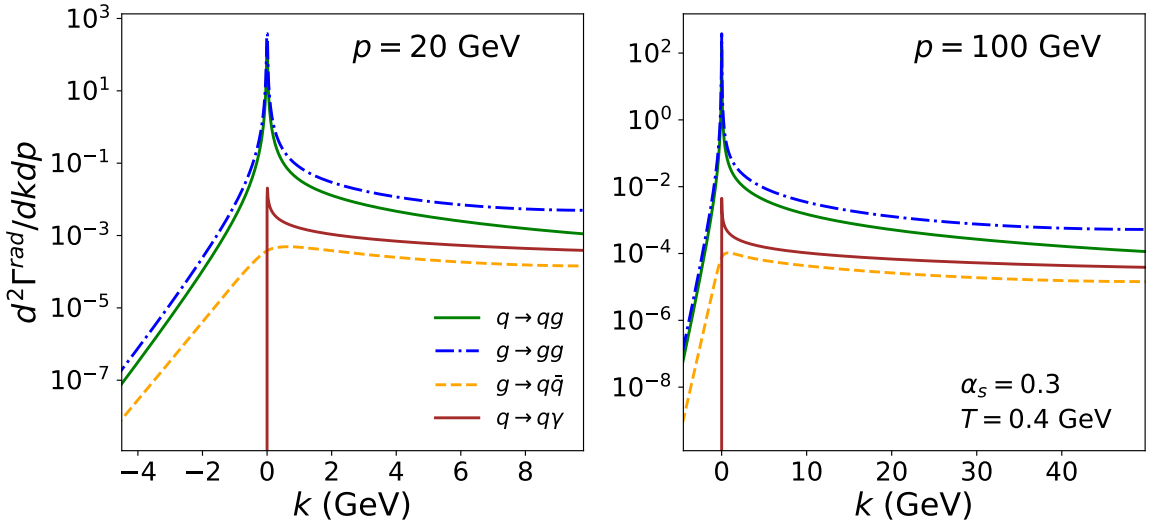

Figure 5.6: The double differential AMY radiative rates for a fixed initial momentum of $p = 20$ GeV (left) and $p = 100$ GeV (right) as a function of momentum k of a radiated parton. In each panel, four different radiative processes are plotted; $q \to qg$, $g \to gg$, $g \to q\bar{q}$, $q \to q\gamma$. The temperature $T = 0.4$ GeV, and the strong coupling $\alpha_s = 0.3$ is used.

Finite-size effect The AMY formalism is developed assuming an infinite, static thermal QCD medium. Caron-Huot and Gale [210] generalized the AMY formalism considering a dynamically evolving medium to incorporate the effect of a finite formation time of radiative processes, $\tau_f \sim 1/g^2T$. In this work, the AMY radiative rate in momentum space as shown in Eq. (5.8) is reformulated to capture the time dependence of the inelastic radiation rate. The basic idea starts with benchmarking the results of the BDMPS-Z radiative energy loss [168–170], in which a rigorous quantum treatment of the LPM effect at finite-size QCD medium is elaborated. The total probability of radiation is given by

$$\frac{dP^a_{bc}}{dk} = \frac{P^{a(0)}_{bc}(x)}{\pi p} \times \mathrm{Re} \int_0^\infty dt_1 \int_{t_1}^\infty dt_2 \frac{\partial}{\partial \mathbf{x}} \cdot \frac{\partial}{\partial \mathbf{y}} \left(\frac{p}{2k(p-k)} \right)^2 [K(t_2, \mathbf{x}; t_1, \mathbf{y}) - (\mathrm{vac})]_{\mathrm{x=y=0}}, \tag{5.9}$$

representing a parton a with energy p produced at time $t_1 = 0$ split into a pair of partons b and c with energy k and $p-k$, respectively. $P^{a(0)}_{bc}(x)$ represent the Altarelli-Parisi splitting

functions in vacuum as shown in Table 3.1. $K(t_2, \mathbf{x}; t_1, \mathbf{y})$ is a propagator associated with the Hamiltonian of the process

$$H = \delta E(\mathbf{p}_\perp) - i\mathcal{C}_3, \tag{5.10}$$

where $\delta E(\mathbf{p}_\perp)$ and $\mathcal{C}_3$ are given by

$$\begin{aligned}
\delta E(\mathbf{p}_\perp) &= \frac{p\mathbf{p}_\perp^2}{2k(p-k)} + \frac{m_b^2}{2k} + \frac{m_c^2}{2(p-k)} - \frac{m_a^2}{2p}, \\
\mathcal{C}_3(\mathbf{x}) &= \frac{C_b + C_c - C_a}{2} v_2(\mathbf{x}) + \frac{C_a + C_c - C_b}{2} v_2(\frac{k}{p}\mathbf{x}) + \frac{C_a + C_b - C_c}{2} v_2(\frac{p-k}{p}\mathbf{x}).
\end{aligned} \tag{5.11}$$

m_a and C_a are respectively the thermal mass and the Casimir factor ($C_F = 4/3$ for quarks and $C_A = 3$ for gluons) of the parton a. $v_2(\mathbf{x})$ is the dipole cross-section for colour singlet $q\bar{q}$ pair [211]. The vacuum term in the time integration in Eq. (5.9) corresponds to the propagator in vacuum. The subtraction of the vacuum term accounts for the renormalization of the parton wave function.

Eq. (5.9) is Fourier-transformed to transverse momentum space and re-organized to remove non-compact time integration to implement the AMY results. The resulting rate is given by [210]

$$\frac{d\Gamma^a_{bc}(t)}{dk} \equiv \frac{P^{a(0)}_{bc}(x)}{\pi p} \times \mathrm{Re} \int_0^t dt_1 \int \frac{d^2\mathbf{q}_\perp}{(2\pi)^2} \int \frac{d^2\mathbf{p}_\perp}{(2\pi)^2} \frac{i\mathbf{q}_\perp \cdot \mathbf{p}_\perp}{\delta E(\mathbf{q}_\perp)} \mathcal{C}(t) K(t, \mathbf{q}_\perp; t_1, \mathbf{p}_\perp). \tag{5.12}$$

$d\Gamma^a_{bc}(t)/dk$ is the time-dependent inelastic radiation rate and the time integration of Eq. (5.12) over t from 0 to ∞ recovers dP^a_{bc}/dk in Eq. (5.9). In transverse momentum space, the time-dependent $\mathcal{C}(t)$ acts as the Boltzmann-like collision operator

$$\begin{aligned}
\mathcal{C}\psi(\mathbf{p}_\perp) = \int_{\mathbf{q}_\perp} C(\mathbf{q}_\perp) \Bigg\{ & \frac{C_b + C_c - C_a}{2} \left[\psi(\mathbf{p}_\perp) - \psi(\mathbf{p}_\perp - \mathbf{q}_\perp)\right] \\
& + \frac{C_a + C_c - C_b}{2} [\psi(\mathbf{p}_\perp) - \psi(\mathbf{p}_\perp + \frac{k}{p}\mathbf{q}_\perp)] \\
& + \frac{C_a + C_b - C_c}{2} [\psi(\mathbf{p}_\perp) - \psi(\mathbf{p}_\perp + \frac{p-k}{p}\mathbf{q}_\perp)] \Bigg\},
\end{aligned} \tag{5.13}$$

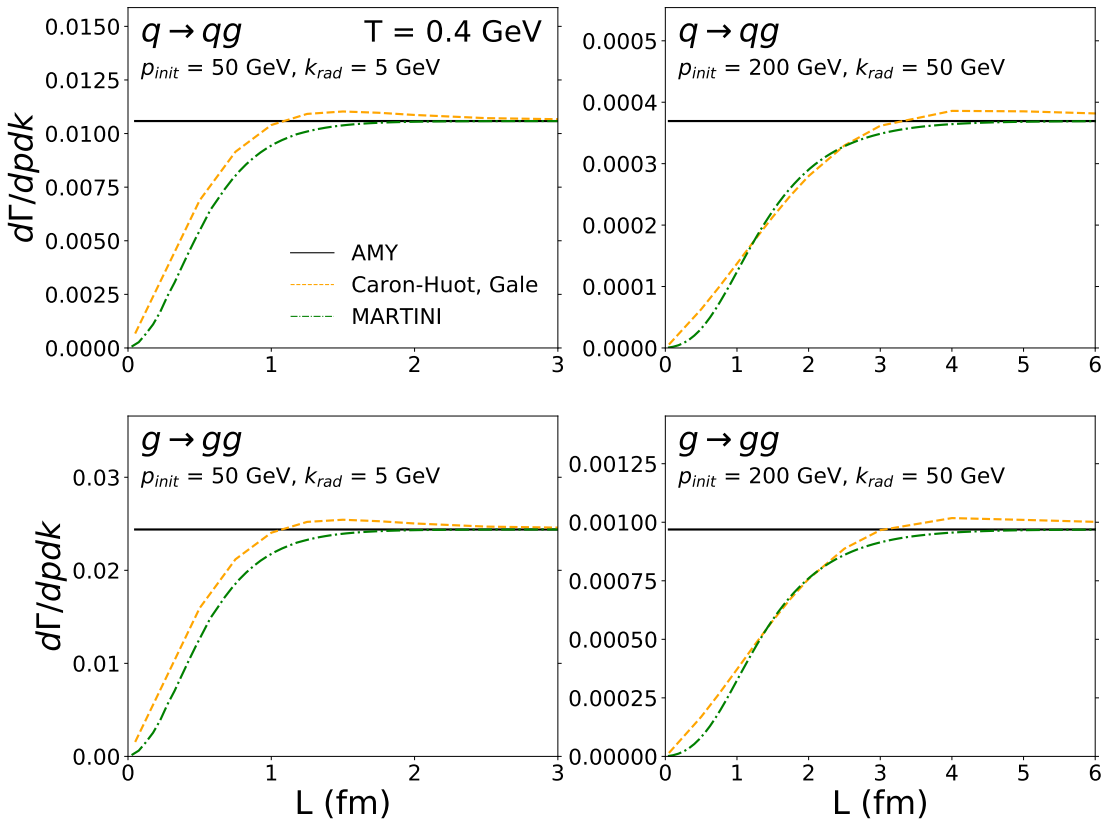

Figure 5.7: The radiative transition rates with the formation time of radiation [210], compared to those reproduced by the Monte-Carlo method in MARTINI. The horizontal axis indicates the length of the non-evolving medium propagated since the birth of initial parton. Each panel represents the two different radiative transition processes (the top and bottom panels) and the two momentum configurations (the left and right panels) at the background temperature of $T = 0.4$ GeV. In each panel, the original AMY rate is also plotted for reference.

where $\psi(\mathbf{p}_\perp)$ is a wave function in transverse momentum space and the function $C(\mathbf{q}_\perp)$ is associated with the differential elastic cross-section in Eq. (5.7). The AMY inelastic radiation rates in Eq. (5.8) and the correction for the finite-size formation time of radiation in Eq. (5.12) will be used for the radiative energy loss processes in this thesis.

Physically, the moment of hard splitting is ambiguously defined within the formation time and the pair of the split partons are not resolved by the medium during this period.

Hence, the radiation rates are suppressed until the pair of partons are identified as individual partons. Eq. (5.12) is the modified AMY rates in which the formation time of radiation is taken into account. Unfortunately, solving Eq. (5.12) repeatedly for each parton in the evolution is a time-consuming task. Instead, we designed a Monte-Carlo procedure that closely follows the physics contained in Eq. (5.12) in our previous work [212] and improved the reproducibility in this work.

To implement the formation time effects in the Monte-Carlo simulations, we introduced a separation condition between the pair using the uncertainty principle,

$$\Delta r_\perp \Delta p_\perp > C(k,T), \tag{5.14}$$

in the transverse direction to that of the original parton. With this condition, the pair of partons are fully incoherent when their transverse distance is greater than the quantum mechanically allowed uncertainty. The minimum uncertainty $C(k,T)$ is parameterized as

$$C(k,T) = 0.25 \times (k/T)^{0.11}, \tag{5.15}$$

where k is the momentum of the emitted parton. Since the radiative processes in MARTINI are collinear, the transverse distances $\Delta r_\perp$ and $\Delta p_\perp$ are driven by the random walk motions of each parton in the response to successive elastic scatterings against thermal partons. This parameterization is chosen to modify the original AMY rates that imitate the solution of Eq. (5.12). This ensures that the radiation rate at early times of the radiation is suppressed while the probability increases at later times as the two partons individually get transverse kicks by elastic collisions in the thermal background.

Fig. 5.7 shows comparisons between the solution of Eq. (5.12) and the results of the Monte-Carlo procedure implemented in MARTINI. The horizontal axis represents the propagation length (time) through the brick medium with a temperature of $T = 0.4$ GeV since the birth of initial parton. The four different configurations of the radiative transition are presented to see the effects of the formation time of radiation and the performance

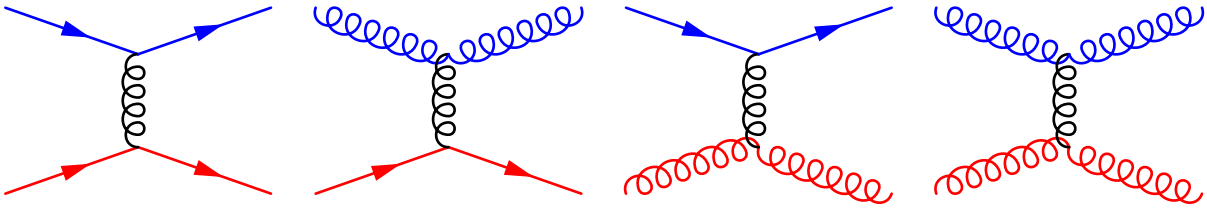

Figure 5.8: Example Feynman diagrams with time running from left to right for the elastic processes included in the MARTINI energy loss model. From left to right, the figures show qq, gq, qg, and gg processes, where qg denotes a process of a hard quark scattering against to a thermal gluon. The symbol q implies either a quark or an anti-quark. The two blue external propagators in each sub-figure indicate hard partons, while those with red external propagators represent thermal partons.

of reproduction in MARTINI in various cases. The top panel shows the process of an initial quark radiating a gluon $q \to qg$, while the lower panel presents the transition of initial gluon radiating another gluon $g \to gg$. The momenta of the original and radiated partons are $p_{init} = 50$ GeV, $k_{rad} = 5$ GeV, respectively, on the left panel and $p_{init} = 200$ GeV, $k_{rad} = 50$ GeV on the right panel. In each panel, the original AMY rates, in which no length (time) dependence is exhibited, are also shown for reference.

We observed that the radiative rates reproduced in MARTINI show gradual increases at early time of the birth of the incoming parton. At later times, roughly after a formation time of radiation τ_f, the rates smoothly converge to the original AMY rates. The behaviours adequately track the results in [210]. We verified that the formation time τ_t parametrically increases with the radiated momentum, i.e., $\tau_f \sim \sqrt{k/T^3}$ in the LPM limit [210].

5.2.2 Collisional energy loss

Collisional energy loss plays an important role in momentum broadening of jet particles. This can be understood by space-like momentum transfer between two scattering particles. Considering collisional energy loss in our research, we follow the approach described in Ref. [203] to obtain the transition rate for $2 \leftrightarrow 2$ elastic scatterings as shown in

Fig. 5.8. Neglecting scatterings between two hard partons, the general expression for the transition rate in the massless limit is

$$\frac{d^2\Gamma(p,\omega,T)}{dpd\omega} = d_k \int \frac{d^3k}{(2\pi)^3} \int \frac{d^3k'}{(2\pi)^3} \frac{2\pi}{16pp'kk'} \delta(p-p'-\omega)\delta(k'-k-\omega) \times |\mathcal{M}|^2 f(k,T)(1 \pm f(k',T))), \tag{5.16}$$

where $p = |\mathbf{p}|$ and $p' = |\mathbf{p}'|$ are the absolute value of the three-momenta of incoming and outgoing hard partons, respectively. $k = |\mathbf{k}|$ and $k' = |\mathbf{k}'|$ are those of thermal partons. The transferred energy ω satisfies the energy conservation condition, $\omega = p - p' = k' - k$, imposed by the delta functions. d_k denotes the degeneracy of the thermal parton of momentum k. The particle distribution functions $f(k,T)$ follow either the Fermi-Dirac distribution for quarks or the Bose-Einstein distribution for gluons. The factor of $1 \pm f(k',T)$ is either Pauli blocking $(-)$ for quarks or Bose enhancement $(+)$ for gluons.

One of the techniques to calculate Eq. (5.16) is to replace the k' integration with the integration over exchanged momentum $\mathbf{q} = \mathbf{k}' - \mathbf{k}$ [213, 214]. In the limit $p \to \infty$ and by placing $\mathbf{p}$ on the x-z plane and $\mathbf{q}$ on the z-axis, Eq. (5.16) reduces to

$$\frac{d^2\Gamma(p,\omega,T)}{dpd\omega} = \frac{d_k}{(2\pi)^3} \frac{1}{16p^2} \int_0^p dq \int_{\frac{q-\omega}{2}}^{\infty} dk\, \theta(q-|\omega|) \times \int_0^{2\pi} \frac{d\phi_{kq|pq}}{2\pi} |\mathcal{M}|^2 f(k,T)(1 \pm f(k',T)), \tag{5.17}$$

where $\phi_{kq|pq}$ is the angle between the $\mathbf{k} \times \mathbf{q}$ and the $\mathbf{p} \times \mathbf{q}$ plane. The lower bound of the k integration $k_{min} = (q-\omega)/2$ is the minimum value of k, which is kinematically allowed to satisfy the on-shell condition for the four partons. The θ function in Eq. (5.17) imposes the momentum restriction, $-q < \omega < q$, ensuring the momentum transfer is always space-like.

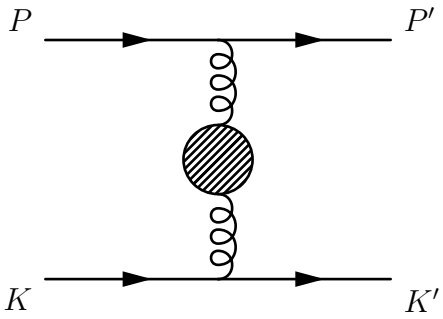

Figure 5.9: Feynman diagram for $2 \to 2$ soft scatterings that contributes to the collisional energy loss rate. P and K are the four-vectors of incoming hard and thermal partons, respective. P' and K' are those of outgoing partons. The upper and lower lines are either quark or gluon legs. The shaded bulb in the middle of the gluon propagator represents the Hard Thermal Loop (HTL) resummation [215, 216].

The transition rate in Eq. (5.17) is evaluated in the limit where the momentum transfer is soft $\sim gT$. In this limit, the squared matrix element, e.g., for $qq \to qq$ scattering, reads

$$|\mathcal{M}|^2_{qq} = \frac{8}{9} g^4 \,\mathrm{Tr}\Big(\not{P}\gamma^\mu \not{P}'\gamma^\nu\Big)\,\mathrm{Tr}\Big(\not{K}\gamma^\alpha \not{K}'\gamma^\beta\Big) D_{\mu\alpha}(Q) D^*_{\nu\beta}(Q), \tag{5.18}$$

where the capital letters denote the four-momenta. The Hard Thermal Loop (HTL) resummed gluon propagator [215, 216] in the Coulomb gauge, shown in Fig. 5.9, is

$$D^{\mu\nu}(Q) = \delta^{\mu 0}\delta^{\nu 0}\Delta_L(\omega, q) + P_T^{\mu\nu}\Delta_T(\omega, q), \tag{5.19}$$

where $P_T^{ij} = \delta^{ij} - \hat{q}^i\hat{q}^j$ is the only non-zero component of the transverse projection operator. The longitudinal and transverse components of the gluon propagators are, respectively,

$$\begin{aligned}
\Delta_L(\omega, q) &= \frac{-1}{q^2 - m_g^2\left[x\ln\left(\frac{x+1}{x-1}\right) - 2\right]}, \\
\Delta_T(\omega, q) &= \frac{-1}{q^2(x^2-1) - m_g^2\left[x^2 + \frac{x}{2}(1-x^2)\ln\left(\frac{x+1}{x-1}\right)\right]},
\end{aligned} \tag{5.20}$$

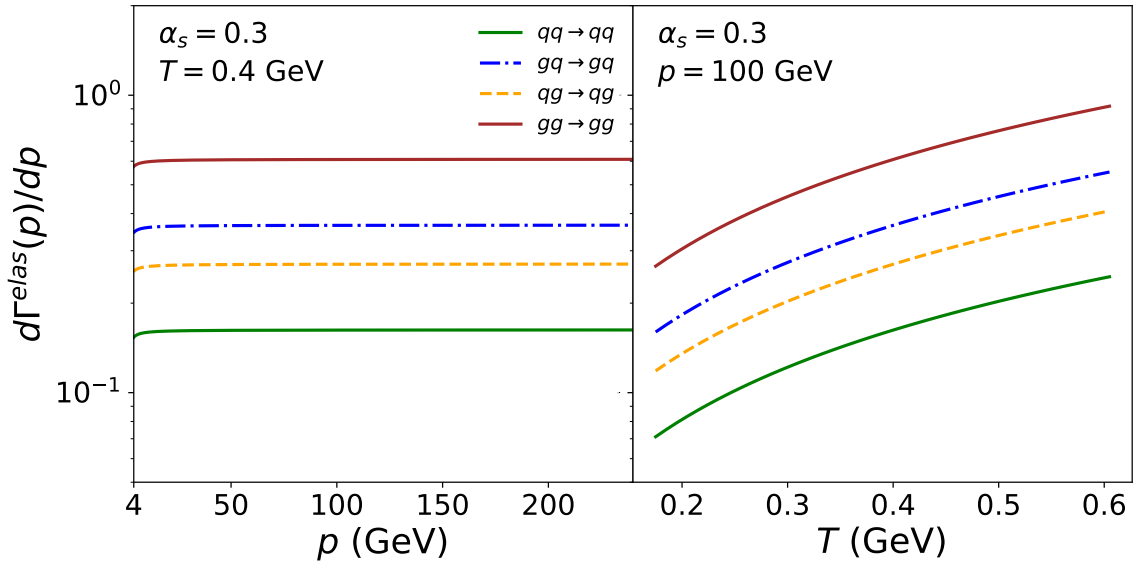

Figure 5.10: The elastic collision rates in Eq. (5.17) as a function of momentum p of a hard parton (left) and of temperature of background medium (right). In each panel, four different elastic scattering processes are plotted; $qq \to qq$, $gq \to gq$, $qg \to qg$ and $gg \to gg$. For $ij \to ij$ process, i and j denote a hard and thermal partons, respectively. The temperature in the left panel is set to $T = 0.4$ GeV, and the initial momentum is set to $p = 100$ GeV. The strong coupling $\alpha_s = 0.3$ is used.

where $x = \omega/q$. Substituting Eq. (5.19) and Eq. (5.20) into Eq. (5.18) and integrating in Eq. (5.18) over the angular variable, we obtain

$$\int \frac{d\phi_{kq|pq}}{2\pi} |\mathcal{M}|^2_{qq} = \frac{8}{9} g^4 p^2 \Bigg[\left\{ (k+k')^2 - q^2 \right\} |\Delta_L|^2 + \frac{1}{2} \left(1 - \frac{\omega^2}{q^2} \right)^2 \left\{ (k+k')^2 + q^2 \right\} |\Delta_T|^2 \Bigg]. \tag{5.21}$$

This result, derived from the soft momentum transfer limit $q \sim gT$, is then applied to the whole transferred momentum region[4]. Inserting Eq. (5.21) into Eq. (5.17) and numerically evaluating the integrals, we finally obtain the collisional energy loss rates.

[4]This approximation is labelled as 'method B' in Ref. [203]. Detailed descriptions and validation of the approximated method can be found in the reference.

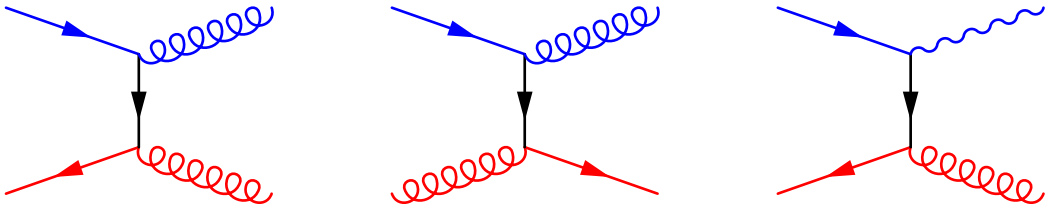

Figure 5.11: Example Feynman diagrams with time running from left to right for the conversion processes in the MARTINI energy loss model. From the left to right panel, an annihilation, a Compton scattering, and a photon conversion process are shown. For the annihilation and Compton scattering processes, time running in both directions is possible. The colour scheme for the external propagators follows the convention shown in Fig. 5.8.

Fig.5.10 shows the elastic rates in Eq. (5.17) versus momentum of an initial parton (left) and the temperature of the QGP (right) for the different elastic scattering processes. Due to the larger Casimir factor for gluons, the scattering processes involving gluons have higher rates than those involving quarks only. Similar to the radiative rates, the collisional rates also have a monotonic dependence on p and moderate dependence on T.

5.2.3 Conversion rate

Besides the scattering processes in which the species of participants remain unaltered, MARTINI also handles conversion processes. Typical examples of annihilation and Compton processes for $q \leftrightarrow g$ as well as photon conversion processes $q \to \gamma$ are shown in Fig. 5.11. In the limit $p \gg T$, the transition rates for those conversion processes are given by [1],

$$\frac{d\Gamma^{conv}_{q\to g}(p,T)}{dp} = C_F \frac{2\pi\alpha_s^2 T^2}{3p}\left(\frac{1}{2}\ln\frac{pT}{m_q^2} - 0.36149\right), \tag{5.22}$$

$$\frac{d\Gamma^{conv}_{g\to q}(p,T)}{dp} = N_f \frac{N_c}{N_c^2-1}\frac{d\Gamma^{conv}_{q\to g}}{dp}, \tag{5.23}$$

$$\frac{d\Gamma^{conv}_{q\to \gamma}(p,T)}{dp} = \left(\frac{e_f}{e}\right)^2 \frac{2\pi\alpha_e\alpha_s T^2}{3p}\left(\frac{1}{2}\ln\frac{pT}{m_q^2} - 0.36149\right), \tag{5.24}$$

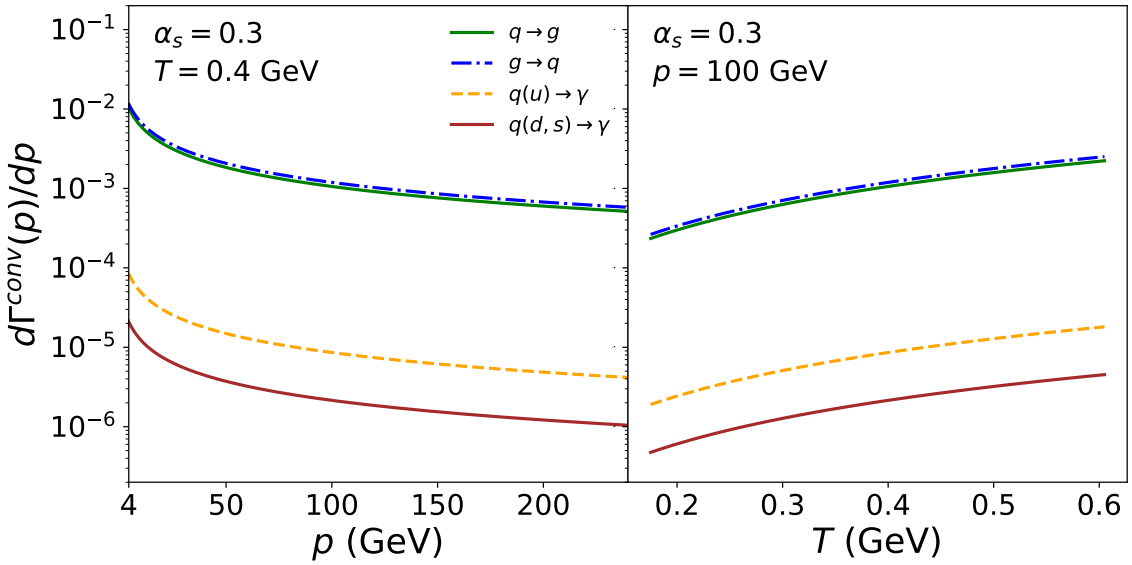

Figure 5.12: Conversion rates in Eq. (5.22), (5.23), and (5.24) as a function of momentum p of a hard parton (left) and of the temperature of the background medium (right). In each panel, four different conversion processes are plotted: $q \to g$, $g \to q$, and $q \to q\gamma$ where q is either u, d or s quarks. The temperature in the left panel is set to $T = 0.4$ GeV and the initial momentum is set to $p = 100$ GeV. The strong coupling $\alpha_s = 0.3$ is used.

The transition rates for $q \to g$ and $g \to q$ in Eq. (5.22) and Eq. (5.23) differ by the factors from the colour and flavour states of the initial and final species. The transition rate for photon conversion $q \to \gamma$ in Eq. (5.24) is analogous to the $q \to g$ rate in Eq. (5.22) where the electromagnetic coupling α_e and the quark charge e_f of flavour f are used for the photon vertex. $m_q = g^2T^2/6$ is the thermal quark mass. Currently, we neglect energy loss during the conversion processes for simplicity, resulting in conversion rates independent of ω.

Fig.5.12 shows the conversion rates in Eq. (5.22), (5.23), and (5.24) versus momentum of an initial parton (left) and the temperature of the QGP (right) for the different conversion processes. We observed that the conversion rates between q and g are nearly identical, while the photon conversion rates are highly suppressed. We also differentiated

the photon conversion processes from u quarks and d, s quarks, which differ by electric charges of the quarks e_f. Similar to the $q\bar{q}$-pair production and photon radiation rates shown in Fig. 5.5, the conversion rates also moderately decrease at higher momentum and increase at higher temperature.

5.3 New developments

5.3.1 QCD running coupling

As discussed in Ch. 2.1, the dependence of the strong coupling constant $\alpha_s(\mu_R^2)$ on a renormalization scale μ_R is an important feature of perturbative QCD. The heavy-ion collision programs at the RHIC and the LHC involve energy scales in the range of $100\,\text{GeV} \sim 1\,\text{TeV}$, providing a good opportunity to explore the dynamics of quarks and gluons in the weak coupling limit. At such high energy scales, it is natural to employ the running coupling scheme in Eq. (2.15) with the β-function coefficient β_0 in Eq. (2.18),

$$\alpha_s(\mu_R^2) = \frac{4\pi}{\beta_0 \ln\left(\mu_R^2/\Lambda_{QCD}^2\right)}, \tag{5.25}$$

$$\beta_0 = 11 - \frac{2}{3}n_f, \tag{5.26}$$

where the number of flavours n_f is fixed to 3 since the massless approximation is the prerequisite for the energy loss models in MARTINI and the dimensional scale $\Lambda_{QCD} = 200$ MeV is used. We impose a cutoff at $\alpha_s = 0.45$ to regulate the divergence in the limit, $\mu_R \to \Lambda_{QCD}$. The running scale μ_R is substituted by the average momentum transfer $\sqrt{\langle p_\perp^2 \rangle}$, which is estimated as

$$\mu_R \to \sqrt{\langle p_\perp^2 \rangle} = \begin{cases} \kappa_r(\hat{q}p)^{\frac{1}{4}} & \text{: radiative processes [2],} \quad (5.27) \\ \kappa_e\sqrt{\hat{q}\lambda_{mfp}} & \text{: elastic processes.} \quad (5.28) \end{cases}$$

For the radiative processes, $\sqrt{\langle p_\perp^2 \rangle}$ is the momentum transfer between original and radiated partons. To obtain Eq. (5.27), we combine the following two equations

$$\hat{q} = \frac{\langle p_\perp^2 \rangle}{\tau_f}, \tag{5.29}$$

$$\tau_f \sim p/\langle p_\perp^2 \rangle, \tag{5.30}$$

where Eq. (5.29) is the definition of the average momentum transfer per unit length $\hat{q}$ and Eq. (5.30) can be derived from the geometrical relationship between original and radiated partons. Eq. (5.28) follows Eq. (5.29) where τ_f is replaced by the mean-free path of the elastic processes λ_{mfp}.

In the previous version of MARTINI [2,217], the running coupling scheme was applied to the vertex of hard splitting and the coupling constant for elastic scattering were fixed. $\hat{q}$ in Eq. (5.27) was parameterized using p and T to reproduce the relative strength of the coupling constant compared to $\alpha_s(p = 10 \text{ GeV})$. The new version uses a rigorous estimation of $\hat{q}$ in Eq. (5.27) for radiative processes and implements the running coupling scheme for the elastic processes as shown in Eq. (5.28).

The average momentum transfer per unit length $\hat{q}$ in Eq. (5.27) and Eq. (5.28) is analytically derived in Ref. [117], given by

$$\begin{aligned}\hat{q} &= \int^{q_{max}} d^2\mathbf{q}_\perp \mathbf{q}_\perp^2 \frac{d\Gamma_{elas}}{d^2\mathbf{q}_\perp} \\ &= C_R \alpha_{s,0} m_D^2 T \ln\left(1 + q_{max}^2/m_D^2\right),\end{aligned} \tag{5.31}$$

with $m_D^2 = g^2T^2(2N_c + N_f)/6$ and $q_{max} \approx 6pT$. The elastic collision rate that enters in Eq. (5.31) is given by

$$\frac{d\Gamma_{elas}}{d^2\mathbf{q}_\perp} = \frac{C_R}{(2\pi)^2} \frac{g^2 m_D^2 T}{\mathbf{q}_\perp^2(\mathbf{q}_\perp^2 + m_D^2)}. \tag{5.32}$$

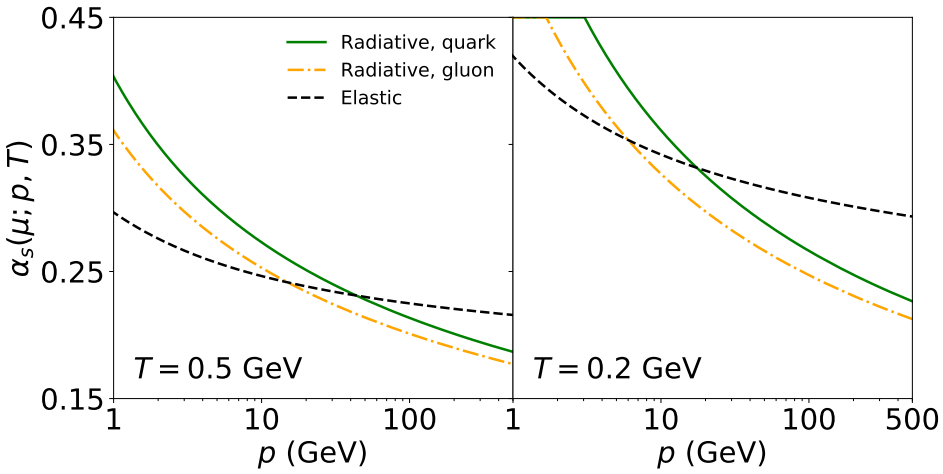

Figure 5.13: Running coupling constant $\alpha_s(\mu_R^2; p, T)$ for the radiative (quark and gluon) and elastic processes as a function of momentum at $T = 0.5$ GeV (left), $T = 0.2$ GeV (right). The maximum value of $\alpha_s = 0.45$ is fixed to avoid infra-rad divergence at $\mu_R \to \Lambda_{QCD}$.

The mean free path of the elastic scatterings λ_{mfp} in Eq. (5.28) can be obtained by

$$\lambda_{mfp} = \frac{1}{\Gamma_{elas}}, \tag{5.33}$$

$$\begin{aligned}\Gamma_{elas} &= \int_{q_{min}}^{q_{max}} d^2\mathbf{q}_\perp \frac{d\Gamma_{elas}}{d^2\mathbf{q}_\perp} \\ &= C_R \alpha_{s,0} T \left[\ln\left(1 + \frac{m_D^2}{q_{max}^2}\right) - \ln\left(1 + \frac{m_D^2}{q_{min}^2}\right)\right].\end{aligned} \tag{5.34}$$

The IR cut-off of the integration in Eq. (5.34) is set to $q_{min} = 0.05T$ to be consistent with the minimum momentum transfer used for the calculations of the total elastic rates [203] implemented in MARTINI.

The prefactors κ_r and κ_e are the free parameters of our model to determine the proportionality between the scale μ_R and averaged momentum transfer estimated in Monte-Carlo simulations for radiation and scattering, respectively. In this thesis, we used $\kappa_r = 1.5$, $\kappa_e = 4.5$. The reference coupling $\alpha_{s,0}$ in Eq. (5.31) influences the running coupling for

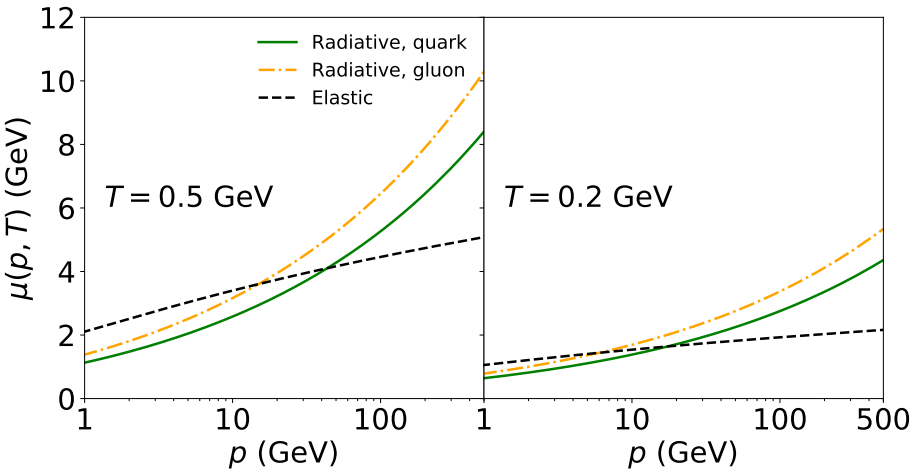

Figure 5.14: The renormalization scale of running coupling constant $\mu_R(p,T)$ for the radiative (quark and gluon) and elastic processes as a function of momentum at $T = 0.5$ GeV (left), $T = 0.2$ GeV (right).

radiation and is set to 0.3. The $\alpha_s(\mu_R^2)$ for elastic scatterings are not affected by the choice of the fixed $\alpha_{s,0}$ since it is cancelled out by $\hat{q}$ and λ_{mfp}.

The quadratic Casimir C_R ($4/3$ for a quark and 3 for a gluon) is cancelled in the final expression of μ_R for scattering in Eq. (5.28), but not for radiation in Eq. (5.27). This naturally introduces a species dependence in the running coupling constant for the radiative processes. The physical argument for this is that the greater colour factor for gluons leads to greater momentum transfer in each interaction, while the strength of the coupling is weaker due to the asymptotic behaviour of the strong coupling constant.

The running coupling constant $\alpha_s(\mu_R^2; p, T)$ in Eq. (5.25) with Eq. (5.27) or Eq. (5.28) versus momentum of a hard parton is shown in Fig. 5.13 at $T = 0.5$ GeV (right) and $T = 0.2$ GeV (left). As mentioned above, the running coupling constant for radiation is distinguished by the quadratic Casimir of species. For the radiative processes, we found the running coupling is 10% higher for quarks than for gluons at $p = 1$ GeV, $T = 0.5$ GeV and this gap decreased at higher momentum scales. The coupling for radiation runs faster than that for elastic scattering. Consequently, the relative contribution of the ra-

diative processes on jet modification would decrease at higher energy scales. Comparing the left and the right panels in Fig. 5.13, the coupling is weaker at the early time of the jet evolution due to high temperatures of the background medium, while it gradually strengthened as the system cools down at later times. Fig. 5.14 shows the estimated renormalization scale $\mu_R(p,T)$ versus parton momentum p at $T = 0.5$ GeV (right) and $T = 0.2$ GeV (left). Similarly to Fig. 5.13, the three different curves represent $\mu_R(p,T)$ for radiative (quark and gluon) and elastic processes. As expected from the analytic expressions, we found that $\mu_R(p,T)$ for radiation has larger dependence on momentum than that for scattering. The difference in $\mu_R(p,T)$ between the radiative and elastic processes becomes significant at higher momentum, $p > 100$ GeV. We also observed that the scale $\mu_R(p,T)$ decreases at lower temperatures.

5.3.2 Thermal recoils

When a jet propagates through a droplet of hot and dense QCD medium, energetic partons from the jet and constituents of the QGP exchange their energies and momenta through successive elastic scatterings. The lost energy and momentum from the jet are deposited into the medium, creating collective flows propagating along with the fast-moving jet [218–224]. The jet-induced flows contain energy and momentum originating from the jet partons, enhancing the soft hadron production near the jet axis. In the kinetic theory approach, this medium response to the jet energy loss is characterized by the constituent partons in the thermalized medium scattering with the jet partons. In traditional analyses of jet quenching, hadronic observables, e.g., the nuclear modification factor R_{AA}, are dominated by energetic hadrons and are relatively insensitive to soft processes. However, since the enhanced soft hadron yield is captured by the jet reconstruction, jet observables are significantly affected by the distribution of the lost energy [225–228]. MARTINI implements the evolution of recoiling partons based on the kinetic theory prescription to study the effect of thermal recoils on jet observables.

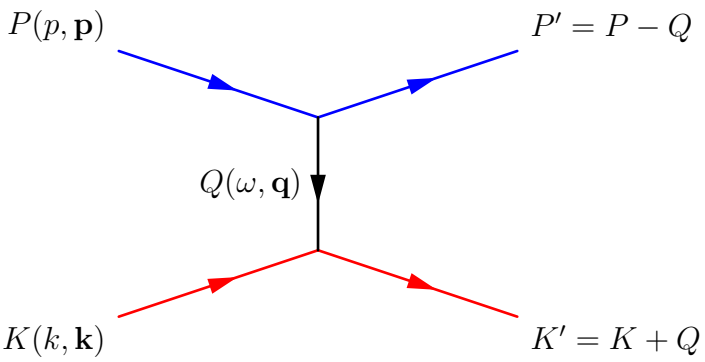

Figure 5.15: Illustration of a $2 \leftrightarrow 2$ elastic scattering process, which creates a thermal recoiling particle of momentum K'. The momenta of hard and soft partons are represented by blue and red, respectively. By convention, the momentum transfer Q flows from a hard parton to a thermal parton.

The elastic scattering processes in MARTINI involve space-like momentum transfer Q as shown in Fig. 5.15. We first sample the four-momentum transfer $Q(\omega, \mathbf{q})$ and then sample a thermal parton $K(k, \mathbf{k})$. The four-momentum of a recoiling parton from a collision is determined by the four-momentum sum of the momentum transfer Q and the momentum of a sampled thermal parton K. In Sec. 5.2, we assumed that all partons in MARTINI jet evolution are massless and on-shell, i.e., $P^2 = K^2 = 0$. The thermal parton is sampled such that the recoil parton also satisfies the on-shell condition, with $|\mathbf{q}| = q$ and $|\mathbf{k}| = k$,

$$\begin{aligned} K'^2 &= (K + Q)^2 \\ &= 2KQ - Q^2 \\ &= 2(k\omega - 2kq\cos\theta) + \omega^2 - q^2 \\ &= 0, \end{aligned} \tag{5.35}$$

which constrains the lower bound of the kinematic range of k,

$$k_{min} = \frac{q - \omega}{2}, \tag{5.36}$$

when $\cos\theta = -1$. This lower limit indicates how much the momentum transfer Q is away from on-shell. We use the rejection sampling method to sample the thermal momentum

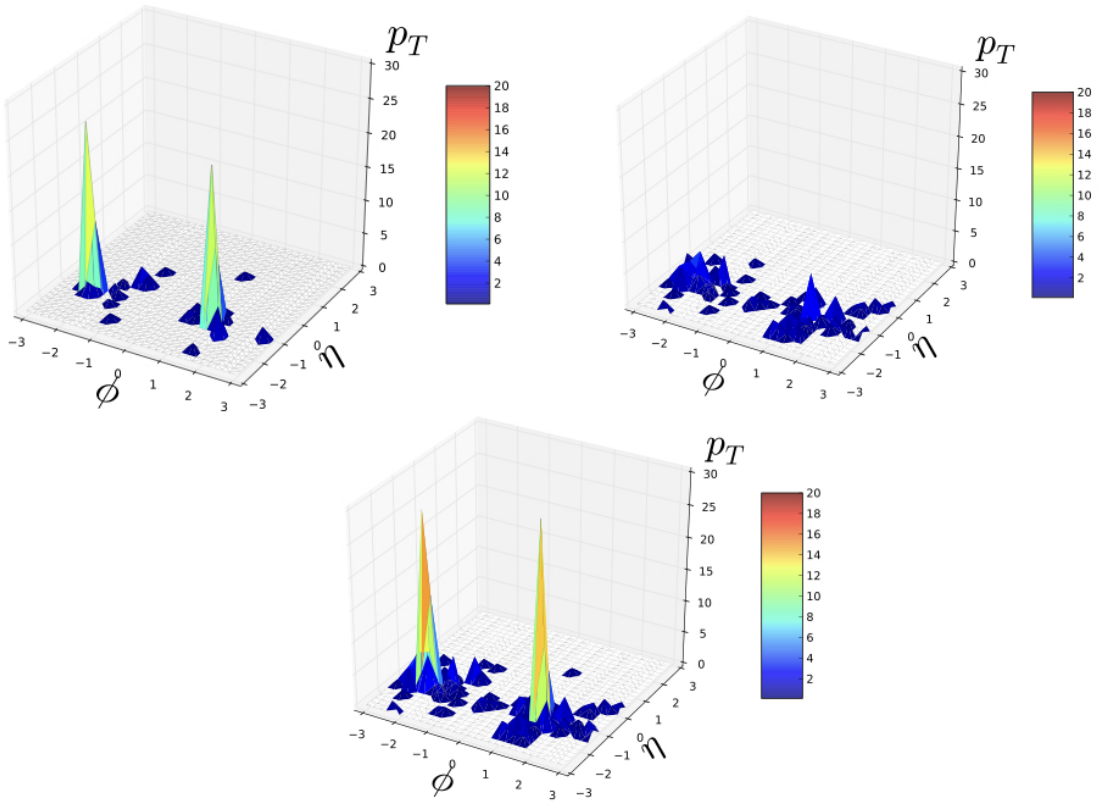

Figure 5.16: The energy distribution of hard partons (upper left), recoiling partons (upper right), and the sum of the hard and recoil partons (lower centre). The horizontal plane represents the azimuthal angle ϕ and rapidity η axis while the vertical axis indicates p_T of partons.

$k \in [k_{min}, \infty)$, which follows either the Fermi-Dirac or the Bose-Einstein distribution. Sampling k determines the angle θ between $\mathbf{k}$ and $\mathbf{q}$.

If the three-momentum of the recoiling parton is greater than a certain kinematic cut p_{cut}, it is included in the list of partons to evolve through the QGP medium. Newly added particles, thermal recoils or medium recoils, can further participate in jet-medium interactions. One can set p_{cut} either to be proportional to the local temperature of the fluid cell or to a fixed value in energy scale. Those whose momenta are lower than p_{cut} should

be treated as a source of medium response to the jet, which is not yet implemented in MARTINI.

The energy distribution of hard parton including thermal recoils in a typical MARTINI event is illustrated in Fig. 5.16. The upper left figure shows hard partons after jet evolution through a QGP medium, while the recoiling partons produced by elastic processes are shown in the upper right figure. The inclusive parton distribution is shown in the lower panel. We observed that the distribution of thermal recoils spread out around the di-jet peaks, confirming momentum broadening effects due to scattering processes. We also noticed that thermal recoils are a richer source than radiated partons at peripheral areas of jets. This effect will be quantified and discussed in detail in Sec. 6.5 by examining jet structure observables.

Notably, the inclusion of recoils causes an increase in the total energy of the system, e.g., those in the parton list for jet evolution in MARTINI, because of additional contribution of sampled thermal partons. To remove the influence of the background component, MARTINI keeps the information of the sampled thermal partons. The energy-momentum of those artificial partons, so-called holes, are subtracted at the analysis level. There exists a caveat that the holes evolve by free-streaming without any elastic scattering against other thermal partons.

5.4 Monte-Carlo implementation

The general flow of the MARTINI program and Monte-Carlo implementation of each component are described as follows:

Jet production An initial hard scattering and subsequent parton shower in vacuum are generated by PYTHIA. The species to collide are decided by the ratio of the number of protons in each nucleus; for heavy-ion collisions, the combinations of proton-proton, proton-neutron, and neutron-neutron collisions are possible. Since PYTHIA does not pro-

vide the option to change the collision system after its initialization, MARTINI employs the modified version of PYTHIA to specify beam species while the events are iterated. The `HadronLevel` flag in PYTHIA is by default off to prevent PYTHIA from processing hadronization before medium evolution.

Jet evolution in vacuum After a collision event is initialized, PYTHIA performs initial state radiation (ISR), final state radiation (FSR), and multiparton interaction (MPI). Partons created in the PYTHIA parton shower enter the time-ordered jet evolution stage. MARTINI accepts only light quarks (u, d, and s) since the energy loss models implemented in MARTINI are based on massless approximation. The partons passed to the jet evolution stage are assumed to be massless and on-shell. The position of the initial hard scattering is randomly sampled from the initial energy or entropy density distribution by giving weight proportional to the density. The partons created by the PYTHIA parton shower are placed at the sampled position and free streamed according to their momentum until the initialization time τ_0 of the QGP. Here we assume that the vacuum shower takes place before the QGP stage and there is no interference between the vacuum and the in-medium shower[5].

In-medium shower Once the hydrodynamic medium emerges, i.e., $\tau > \tau_0$, the vacuum shower switches to an in-medium shower. In MARTINI, partons can evolve if their momenta exceed a certain threshold[6], typically chosen to $p_{min} \sim 4T$. While a parton propagates through the medium, it is Lorentz-boosted into the rest frame of the hydrodynamic

[5]This assumption implies that the virtualities (off-shellness) of all partons have to decrease down to a scale of order $Q^2 \sim 1$ GeV^2 before $\tau < \tau_0$ so that the vacuum shower ends before the QGP is initialized. More recent work [229] showed that there is a large potential overlap between the vacuum and the in-medium shower, e.g., see Fig. 1 in Ref. [229]. This requires that an energy loss model handles high-virtuality parton showers in the medium as well as in-medium showers for on-shell partons, which is challenging to achieve. The purpose of [229] is to combine multiple energy loss models, each of which engages in a different virtuality regime of jet evolution. For this study, we stick to this assumption as we utilize a single energy loss model.

[6]This is because the energy loss models implemented in MARTINI are constructed in the asymptotic limit. The momentum cut, $p_{min} \sim 4T$, is to avoid any unreliable behaviours at the energy scale $\sim \Lambda_{QCD}$, while to preserve features of parton energy loss as much as possible.

fluid cell where the parton is located. The boost factor is determined by the fluid velocity $\mathbf{v}$ in Eq. (4.17) and (4.18), which is provided by the hydrodynamic calculations. In the frame of the fluid cell, transition rates are computed according to the local temperature of the cell. The total probability for a parton of momentum p to undergo any energy loss process is determined by

$$\begin{aligned} P(p,\Delta\tau) &= \Delta\tau \frac{d\Gamma_{total}(p,T)}{dp} \\ &= \Delta\tau \left[\int dk \frac{d^2\Gamma_{rad}(p,k,T)}{dpdk} + \int d\omega \frac{d^2\Gamma_{elas}(p,\omega,T)}{dpd\omega} + \frac{d\Gamma_{conv}(p,T)}{dp} \right], \end{aligned} \tag{5.37}$$

where $\Delta\tau$ is time step in a unit of proper time. The transition rate of each process can be found in Eq. (5.8) (radiative), Eq. (5.17) (elastic), and Eq. (5.22) (conversion). The time step $\Delta\tau$ is set to a small number to guarantee the total probability does not exceed 1.

If a random number $x \in (0,1)$ is smaller than the total probability $x < P(p,\Delta\tau)$, then it decides which process occurs according to the relative probabilities of each process that the given parton can undergo. In case of radiative processes, we sample the radiated energy assuming that radiation processes are collinear. This is a good approximation in the weak coupling limit since the opening angle of radiation, of order g [181], is suppressed. For elastic processes, a space-like four-momentum transfer $Q = (\omega, \mathbf{q})$ is sampled with constraints such that $|\omega| < |\mathbf{q}|$. In case the recoil feature is on, a thermal parton that satisfies Eq. (5.36) is sampled to create a thermal recoiling parton. We use the rejection sampling method to sample those quantities. Once parton information is updated accordingly, the transition processes are finished and the resulting outgoing parton(s) is boosted back into the lab frame for further propagation.

Hadronization The in-medium shower terminates when all fluid cells cool down to a transition temperature T_c. Then information on final partons is passed to PYTHIA for hadronization. Since we use the Lund string model in PYTHIA, it is essential to keep track of colour strings of all partons during the in-medium shower. Partons originating from

the PYTHIA parton shower, thermal recoils, and holes are separately hadronized through the Lund model to distinguish sources of hadrons for analysis purposes. The final-state hadrons converted from the hadronization process are collected for further analysis purposes.

5.5 Summary

In this chapter, we introduced MARTINI, a Monte-Carlo event generator for heavy-ion collisions to study jet energy loss. In Sec. 5.1, we discussed the time-ordered evolution of the momentum distribution in Eq. (5.1) and Eq. (5.2), key components in MARTINI, as well as MARTINI's modular features. Sec. 5.2 briefly reviewed the jet energy loss models implemented in MARTINI, including the AMY radiative energy loss formalism, collisional processes, and conversion processes. Apart from the energy loss models, we improved MARTINI by adopting the running coupling scheme and thermal recoils as discussed in Sec. 5.3 for more realistic heavy-ion simulation at higher energy scales. Finally, the detailed Monte-Carlo methodology to solve Eq. (5.1) and Eq. (5.2) was covered in Sec. 5.4. In the next two chapters, we will show MARTINI results of jet observables that are sensitive to jet quenching and modification due to the QGP medium created in heavy-ion collisions.

Chapter 6

Jet modification in Pb+Pb collisions

In the previous chapter, we discussed the Monte-Carlo event generator for heavy-ion collisions MARTINI with full details of theoretical energy loss models. Its primary purpose is to quantify the jet-medium interplay at the parton level and provide a profound understanding of jet quenching in the QGP. To achieve a realistic environment of jet evolution, we have incorporated the new running coupling scheme and creation of thermal elastic recoils in Sec. 5.3. Implementing jet energy loss prescriptions into the Monte-Carlo event generator is described in Sec. 5.4.

In this chapter, we investigate jet quenching in large colliding systems e.g., Pb+Pb collisions, at LHC energy scales. This involves the theory-to-experiment comparisons to support the findings from experimental measurements provided by the RHIC and the LHC. Sec. 6.1 provides initial conditions of the jet evolution and hydrodynamic modelling of the QGP medium for jet-medium interaction. We introduce the full jet reconstruction techniques [230] provided by FASTJET [231] to find the original jet partons produced by primary hard scatterings. This chapter addresses the analyses of reconstructed jet observables together with single hadron observables. In Sec. 6.3 we investigate the effects of the running coupling and the formation time of radiation using hadronic and jet observables. Sec. 6.4 presents the systematic study of jet energy loss at two different centrality classes and with various values of the jet radius. The study of jet structure modifications due to

medium interaction yield plenty of insights into jet quenching. We show the results of selected jet structure observables in Sec. 6.5. Sec. 6.6 summarizes this chapter.

6.1 Initial conditions and hydrodynamic modelling

The MARTINI simulation requires three key components of jet evolution in heavy-ion collisions: a parton list after vacuum shower, the initial positions of jets, and space-time information of the QGP medium. PYTHIA creates a parton shower through the built-in MARTINI interface (see Sec. 5.4 for details). For realistic jet production, we use CTEQ6L [113] parton distribution function and EPS09LO [121] nuclear PDFs. MARTINI, however, does not incorporate the initial condition module for jets and hydrodynamic modellings. Users should, therefore, specify the paths to those external files in the MARTINI setup file.

To determine the initial positions of jets embedded into the evolution, we first assume that the density distribution of jets is correlated with the energy density at the initial stage of the collision. This is a good approximation because the initial energies are deposited from binary collisions, which also produce high-energy jets. Then the location of each jet is sampled in the transverse plane with weights proportional to the energy density provided by IP-Glasma [3]. The longitudinal position in the z direction is fixed to zero at $\tau = 0$.

Fig. 6.1 shows the transverse profiles of initial energy density of four different centrality classes of Pb+Pb collisions at $\sqrt{s_{NN}} = 2.76$ TeV. The bumpy shapes of the density profiles reflect the realistic event-by-event fluctuations of initial parton interaction between the two nuclei. The randomly distributed hot spots (red) represent higher chances of jet production at the locations. In peripheral centralities, the size of the QGP decreases because of the smaller overlap zone of collisions. Our hydrodynamic model uses the initial energy density profile as an input to the simulations.

MUSIC, state-of-the-art viscous $3 + 1$ dimensional hydrodynamic model [100], performed the hydrodynamic simulations in this work. We used the parameterized equa-

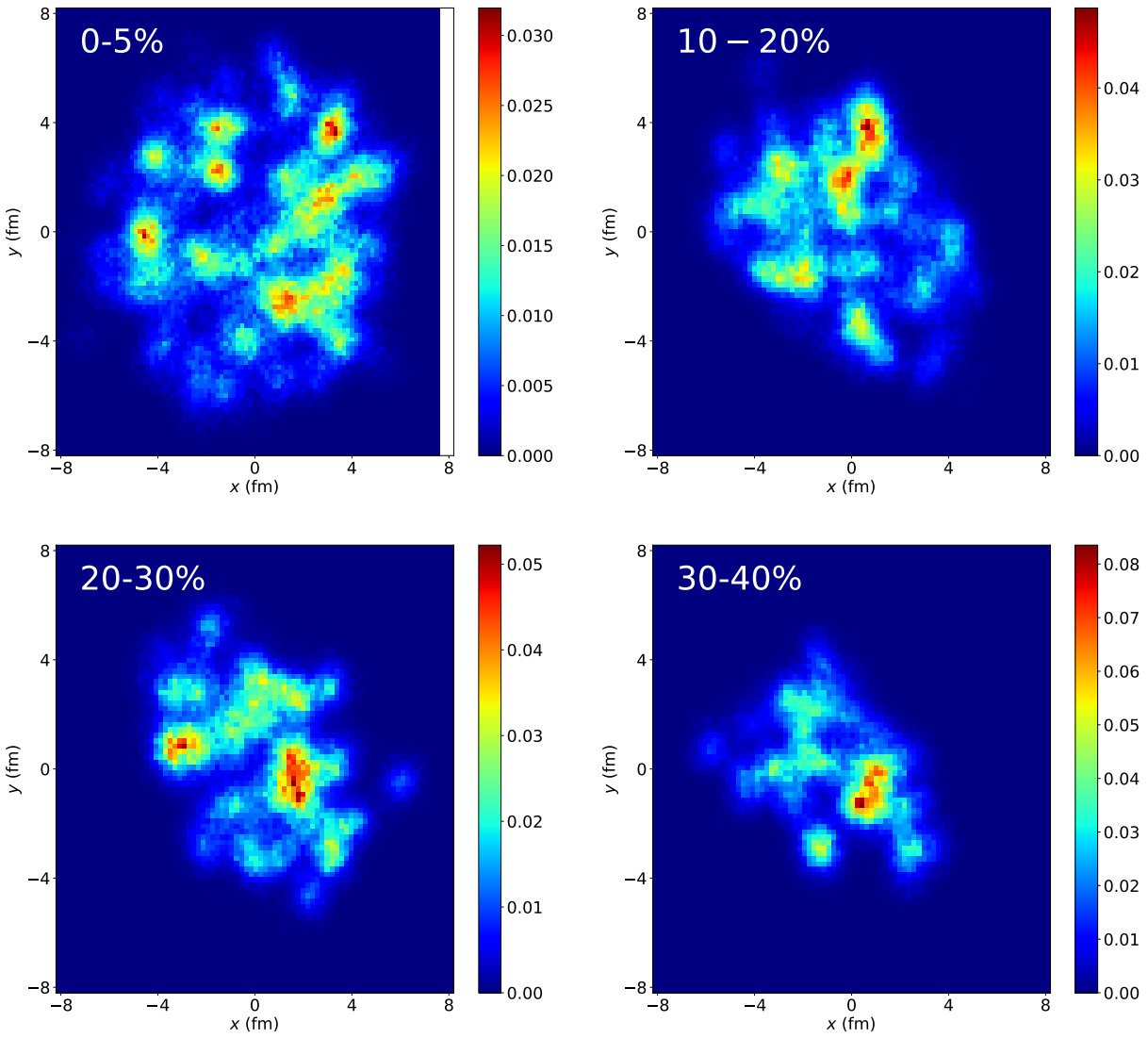

Figure 6.1: The transverse profile of the energy density at the initial stage of collisions for $\sqrt{s_{NN}} = 2.76$ TeV Pb+Pb collisions. Each figure shows different centrality classes. The colour bar represents the relative energy density at a given location. The profile is provided by IP-Glasma model [3].

tions of state provided by Huovinen and Petreczky (s95p-v1) [232] for $\sqrt{s_{NN}} = 2.76$ TeV, and the HotQCD Collaboration [50] for 5.02 TeV collisions. MUSIC generates information of the three velocity and temperature of the fluid cell at each $3+1$D space-time grid, which is then imported by MARTINI for jet-medium interaction.

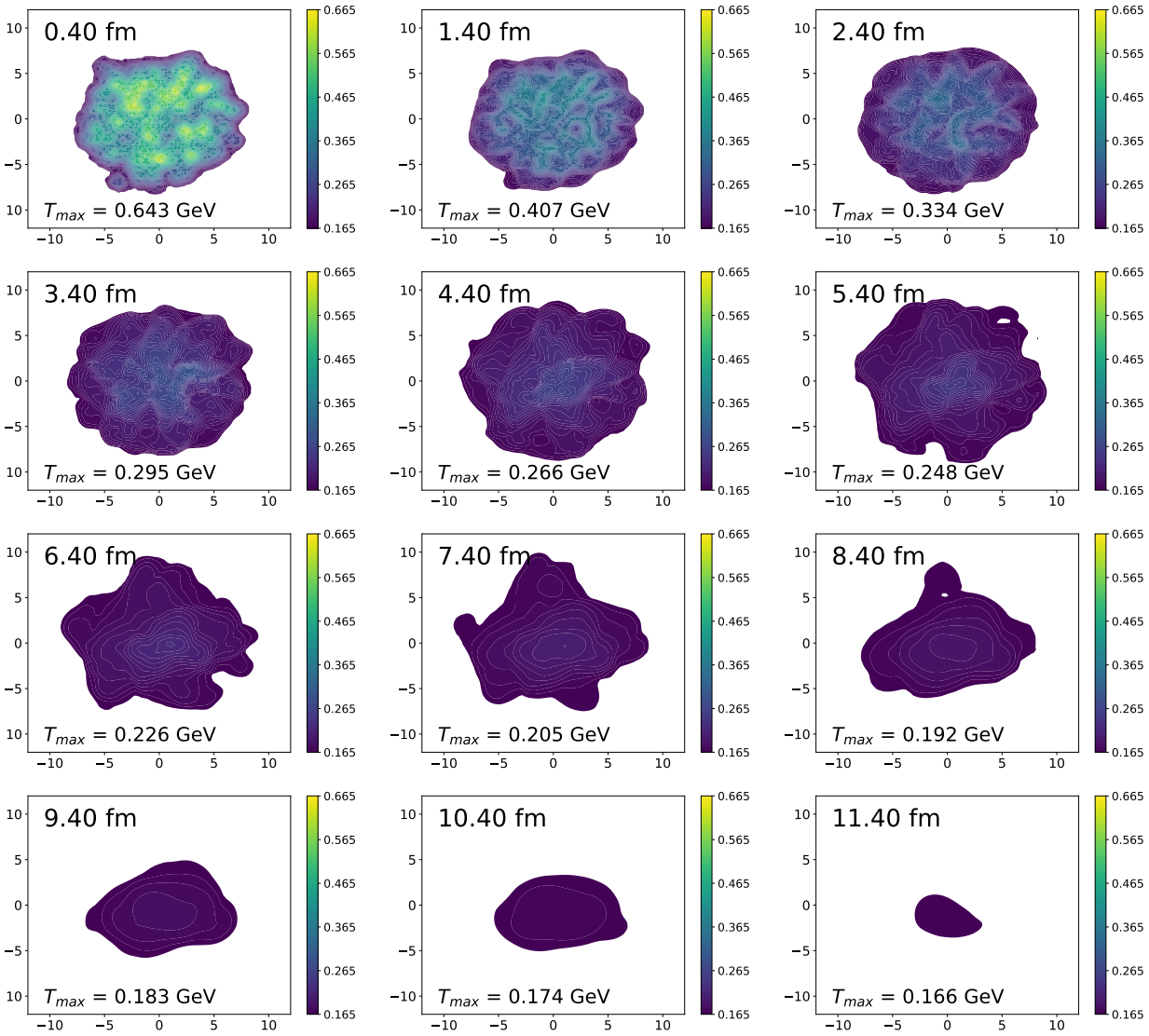

Figure 6.2: Temperature distributions in the transverse plane at mid-rapidity ($\eta = 0$) at different times obtained by MUSIC [100] simulations for 0-5% Pb+Pb collisions at $\sqrt{s_{NN}} = 2.76$ TeV. The initialization time of hydrodynamic simulation is $\tau = 0.4$ fm and the freeze-out temperature of the system is $T_c = 0.165$ GeV. The white background represents either the medium is absent or the temperature is lower than T_c. As time goes on, the thermalized medium cools down to T_c and the whole medium is frozen out at $\tau \sim 12$ fm.

Fig. 6.2 illustrates the different time slices of the temperature evolution in the transverse plane at mid-rapidity ($\eta = 0$) obtained from a 0-5% Pb+Pb collision at $\sqrt{s_{NN}} = 2.76$ TeV. The hydrodynamic simulation is initialized at $\tau_0 = 0.4$ fm, and the chemical freeze-

out temperature, where the phase transition to the hadronic state occurs, is $T_c = 0.165$ GeV. The white background shows that either the medium is absent or the temperature of the fluid cell at the position is lower than T_c. The maximum temperature T_{max} is represented on the bottom-left side of each panel. We found that the highest temperature is around $T_{max} = 0.65$ GeV at the beginning of the evolution and decreases as the medium evolves. Since we used the event-by-event fluctuating initial entropy density for the initial condition of MUSIC simulation, the temperature profiles also reflect the fluctuating features.

6.2 Hadronic and jet observables

The main observable that we present in this paper is the nuclear modification factor R_{AA} in Eq. (4.22). The Lorentz invariant charged hadron differential yield, often referred to as p_T spectrum is given by

$$E\frac{d^3N^{ch}(p_T)}{d^3\mathbf{p}} = \frac{1}{2\pi p_T}\frac{d^2N^{ch}(p_T)}{dp_T d\eta}, \tag{6.1}$$

which has a form of Eq. (4.8) but averaged over azimuthal angle. The Lorentz invariant charged hadron differential yield is related to the invariant differential cross-section

$$E\frac{d^3\sigma^{ch}(p_T)}{d^3\mathbf{p}} = \left[E\frac{d^3N^{ch}(p_T)}{d^3\mathbf{p}}\right]\sigma^{NN}_{inel}, \tag{6.2}$$

where σ^{NN}_{inel} is the inelastic nucleon-nucleon cross-section. The simplest task to perform in the experimental aspect is to measure the invariant charged hadron differential yields from Pb+Pb and pp collisions and construct the nuclear modification factor for charged hadrons

$$R^{ch}_{AA}(p_T) = \frac{1}{\langle N_{coll}\rangle}\frac{d^2N^{ch}_{AA}(p_T)/dp_T d\eta}{d^2N^{ch}_{pp}(p_T)/dp_T d\eta}, \tag{6.3}$$

where N_{coll} is the number of binary nucleon-nucleon collisions in Pb+Pb collisions.

Perturbative QCD provides a theoretical foundation to calculate parton energy loss from first principles. However, hadronic observables may blur the important features at

the parton level because of non-perturbative effects such as hadronization. This issue motivated the invention of full jet reconstruction techniques [230], which combines hadronic jet fragments in the final state. The idea is to retrieve the original partons that initiated the parton shower. Since jet reconstruction clusters four-momenta of hadrons within the defined area, reconstructed jets are less sensitive to non-perturbative effects. Moreover, full jets offer differential information on jet-medium interplay since they contain both leading and sub-leading hadrons. Jet clustering algorithms widely used in jet analyses, e.g., longitudinally invariant k_T [233, 234], inclusive Cambridge/Aachen [235, 236], and anti-k_T [237], are available in the FASTJET3 [231] package. One can cluster jets from the measured hadrons and obtain the inclusive jet yield

$$E\frac{d^3N^{jet}(p_T)}{d^3\mathbf{p}} = \frac{1}{2\pi p_T}\frac{d^2N^{jet}(p_T)}{dp_T d\eta}. \tag{6.4}$$

The jet nuclear modification factor is then evaluated using the jet cross-section from Pb+Pb and pp collisions

$$R^{jet}_{AA}(p_T) = \frac{1}{\langle N_{coll}\rangle}\frac{d^2N^{jet}_{AA}(p_T)/dp_T d\eta}{d^2N^{jet}_{pp}(p_T)/dp_T d\eta}. \tag{6.5}$$

Throughout this thesis, we used the anti-k_T jet clustering algorithm to cluster jets from final state hadrons, which is the most commonly used technique in experiments.

Using the definitions of the p_T spectra shown in Eq. (6.1) and Eq. (6.4), we computed charged hadron and jet p_T spectra in $\sqrt{s_{NN}} = 2.76$ TeV pp collisions. Since the jet production rate in the transverse momentum space is a steeply falling function, $\sim p_T^{-n}$ with positive n, producing enough statistics at a high p_T scale requires a huge number of Monte-Carlo events. To achieve high efficiency in the analysis, we divide the kinematically-allowed phase space[1] into sub-space intervals. Then we generate Monte-Carlo events of $\sim 10^4$ with the kinematic sub-interval as an input. In the analysis stage, we combine the

[1]In PYTHIA this can be controlled by phase space parameters, PhaseSpace:pTHatMin and PhaseSpace:pTHatMax. Practically we set finer grid at lower $\hat{p}_T$ and coarse grid at higher $\hat{p}_T$ up to the half of the colliding energy scale, which is the maximum energy of momentum transfer in initial hard scatterings.

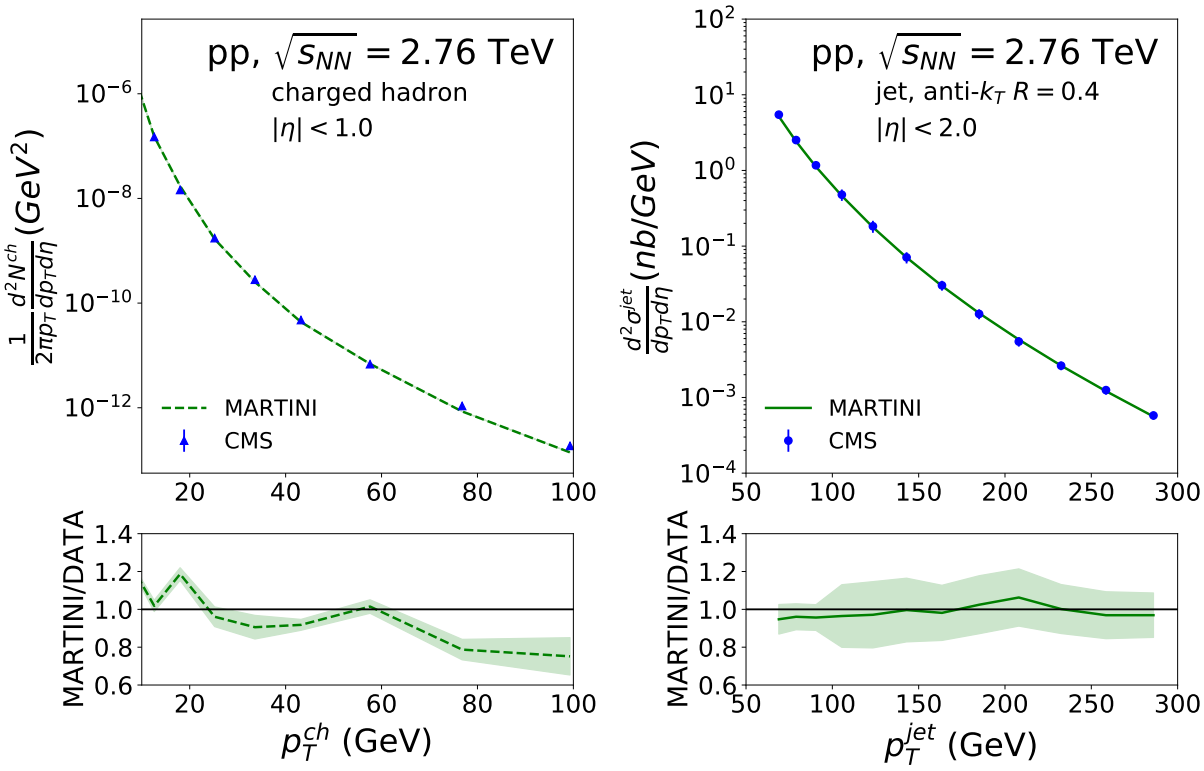

Figure 6.3: The Lorentz invariant charged hadron differential yield averaged over pseudorapidity $|\eta| < 1$ (left) and invariant jet differential cross-section in $|\eta| < 2$ at $\sqrt{s_{NN}} = 2.76$ TeV pp collisions. For the jet clustering algorithm, we used the jet radius parameter $R = 0.4$. The green lines and the blue dots correspond to the results obtained by MARTINI simulations and experimental data from the CMS collaboration [116, 187], respectively. The lower panel shows the ratio between MARTINI and the CMS results. The green bands around the lines show the statistical uncertainties.

results obtained from each sub-interval with weight by corresponding jet cross-section computed by PYTHIA.

Fig. 6.3 presents the MARTINI results for pp collisions where the hydrodynamic medium is expected to be absent. The left figure shows the invariant charged hadron differential yield averaged over pseudorapidity space $|\eta| < 1$, and the right figure is the invariant jet cross-section averaged over $|\eta| < 2$. We used the radius parameter $R = 0.4$ for the jet clustering algorithm. The green bands around the lines denote the statistical uncertainties, which are reduced by accumulating corresponding MARTINI Monte-Carlo events.

We compare our MARTINI calculations to the corresponding CMS [116,187] results. We present their ratio in the bottom panel of each plot. Each ratio shows that our results of p_T spectra at pp collisions deviates from the experimental data by at most 20%. The MARTINI simulations through PYTHIA reproduce the pp measurements within the deviation less then 20%. Thus our pp results serve as a legitimate baseline for our jet quenching analysis in heavy-ion collisions throughout this thesis.

6.3 Effects of running coupling and the formation time of radiation

In the previous chapter, we illustrated how we implemented the running coupling scheme and the formation time of radiation in MARTINI. In this section, we show the effects of each implementation in observables and demonstrate how they improve the descriptions of measurements.

Fig. 6.4 shows the charged hadron nuclear modification factor R_{AA} for 0-5% Pb+Pb collisions at $\sqrt{s_{NN}} = 2.76$ TeV. The four lines with different colours correspond to the MARTINI simulation results with unique combinations of the formation time of radiation (the last part of Sec. 5.2.1) and running coupling scheme (Sec. 5.3.1). For the case with the fixed coupling configurations, we set $\alpha_s = 0.36$ to describe the data at $p_T \sim 10$ GeV. The shaded bands around each line correspond to the statistical uncertainties.

The result with both the features (blue) agrees well with the CMS measurements [187], while that with none of the effects yields stronger energy loss of the charged hadron production rate with the weaker p_T dependence. The two features considerably decrease the energy loss of jets in the QGP. First, the running coupling scheme reduces the interaction strength between jets and the QGP. Fig. 5.13, for example, shows that the coupling constant $\alpha_s(\mu_R; p, T)$ decreases as the parton momentum and temperature increase. This reduced $\alpha_s(\mu_R; p, T)$ directly influences the AMY radiative transition rates in Eq. (5.8) and the elastic scattering rates in Eq. (5.17) and Eq. (5.21), leading to smaller quenching for

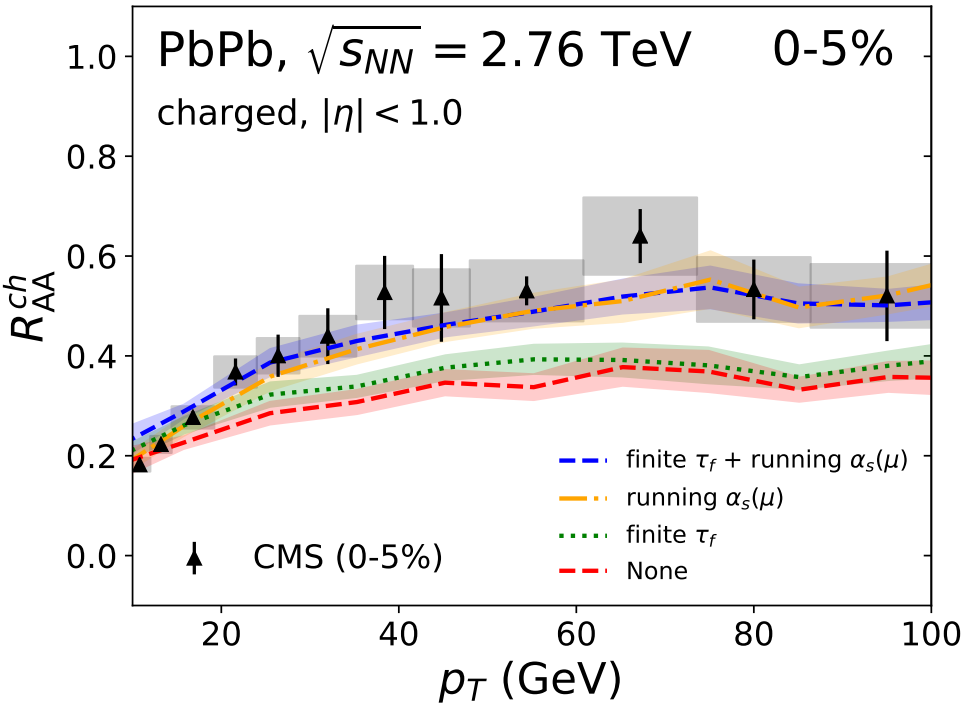

Figure 6.4: Charged hadron nuclear modification factor R_{AA} for 0-5% Pb+Pb collisions at $\sqrt{s_{NN}} = 2.76$ TeV. The blue line shows the MARTINI result, including both effects, while the red line shows the result without those effects. The orange and green lines include running coupling and finite formation time, respectively. We compare our MARTINI to the CMS measurements [187].

more energetic partons. Furthermore, the temperature dependence of $\alpha_s(\mu_R; p, T)$ results in weaker quenching at an early time of the evolution. The quenching effect becomes stronger at later times with higher QGP temperatures.

Second, the formation time of in-medium radiation reduces the radiative transition rates at the early time since the birth of the radiated parton, shown in Fig. 5.7. The formation time increases like $\tau_f \sim \sqrt{k/T^3}$, where k is the momentum of the radiated parton. However, a typical formation time of radiation should not be large since Fig. 5.6 shows that the distributions of radiated partons have a peak at $k \sim 0$. We observed that the running coupling has a dominant influence on the jet quenching and p_T dependence of R_{AA} while the effect caused by the finite-size formation time of radiation is relatively small.

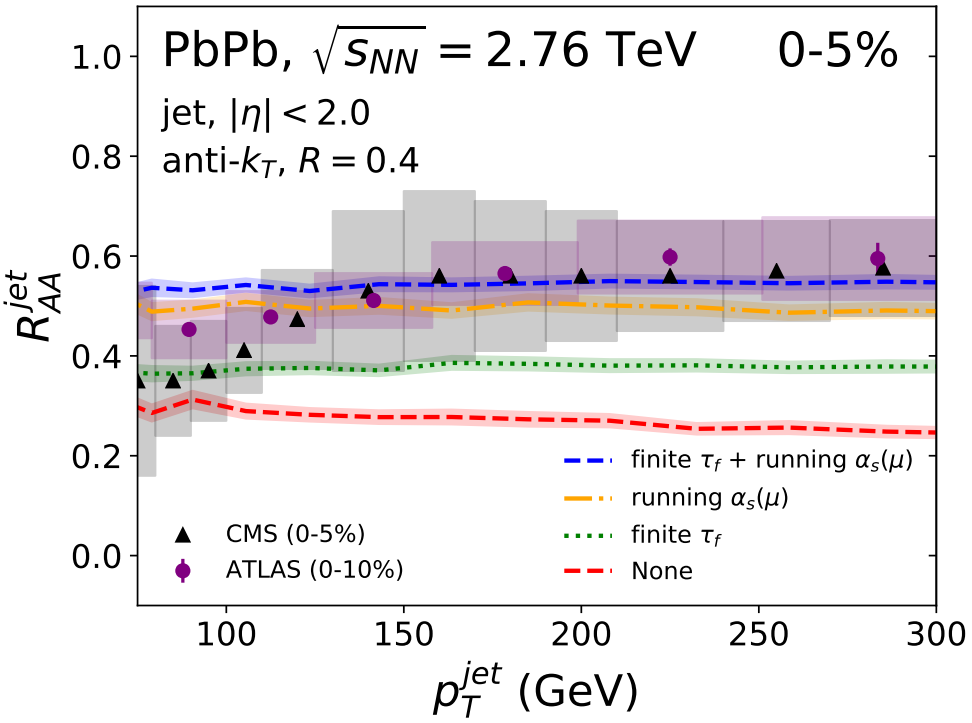

Figure 6.5: Inclusive jet nuclear modification factor R_{AA} with $R = 0.4$ for 0-5% central Pb+Pb collisions at $\sqrt{s_{NN}} = 2.76$ TeV. The colour scheme for the four lines is same as that in Fig. 6.4 We compare our results to the measurements from the CMS [116] and ATLAS [114] collaborations.

With the running coupling scheme turned on, the formation time only affects the R_{AA} values at low p_T ($10 \sim 30$ GeV). This is because their effects are not independent of each other, but are rather convolved. Our results suggest that the two features implemented in MARTINI improve the descriptions of the charged hadron R_{AA} at $\sqrt{s_{NN}} = 2.76$ TeV.

In Fig. 6.5, we present the MARTINI results of the jet R_{AA} for 0-5% central Pb+Pb collisions at $\sqrt{s_{NN}} = 2.76$ TeV with the same setups as shown in Fig. 6.4. We used the radius parameter $R = 0.4$ and passed a complete set of final-state hadrons, i.e., hadrons from the initial parton shower, recoils, and holes, to FASTJET. As mentioned earlier, the fictitious hadrons that correspond to the holes are subtracted from the jet signals at the analysis stage. Similar to the case of the charged hadron R_{AA} calculations, both the effects contribute to smaller jet quenching but result in monotonic magnitude shifts in transverse

momentum space in the jet R_{AA}. The finite-size effects of radiation induce increases of the jet R_{AA} over the entire p_T range because those jets consist of low p_T hadrons (30-50 GeV). Comparing to the measurements from the CMS [116] and ATLAS [114] collaborations, we achieved a better agreement when including the two effects. This is a consistent trend with what we found in the charged hadron analysis. We notice that the CMS measurement exhibits more quenching at lower p_T than the ATLAS result in 0-10% possibly due to the centrality difference.

6.4 Systematic analysis of jet quenching

From the analysis presented in Sec 6.3 we concluded that the two effects, the running coupling scheme and the formation time of in-medium radiation, lead to a better agreement with the measurements of the charged hadron and the jet R_{AA}. Now we shall use this MARTINI configuration with the initial conditions shown in Sec. 6.1 as our baseline for further investigations of jet quenching in heavy-ion collisions.

This section presents the in-depth analysis of jet quenching using more differential measurements of the charged hadron and the jet R_{AA} provided by the heavy-ion programs in the LHC at $\sqrt{s_{NN}} = 2.76$ and 5.02 TeV. We explore the relationship between the jet quenching effects and the size of the QGP by looking at higher centrality classes. This is further validated by cross-checking comparisons to measurements from different collaborations. The jet analysis is sensitive to the jet definition and the radius parameter R used in the analysis. We conduct the same jet analysis by varying the size parameter R and investigate the R dependence of the quenching effect of reconstructed jets. Then we switch to 5.02 TeV Pb+Pb collisions to explore the behaviour of jet quenching at a higher kinematic regime.

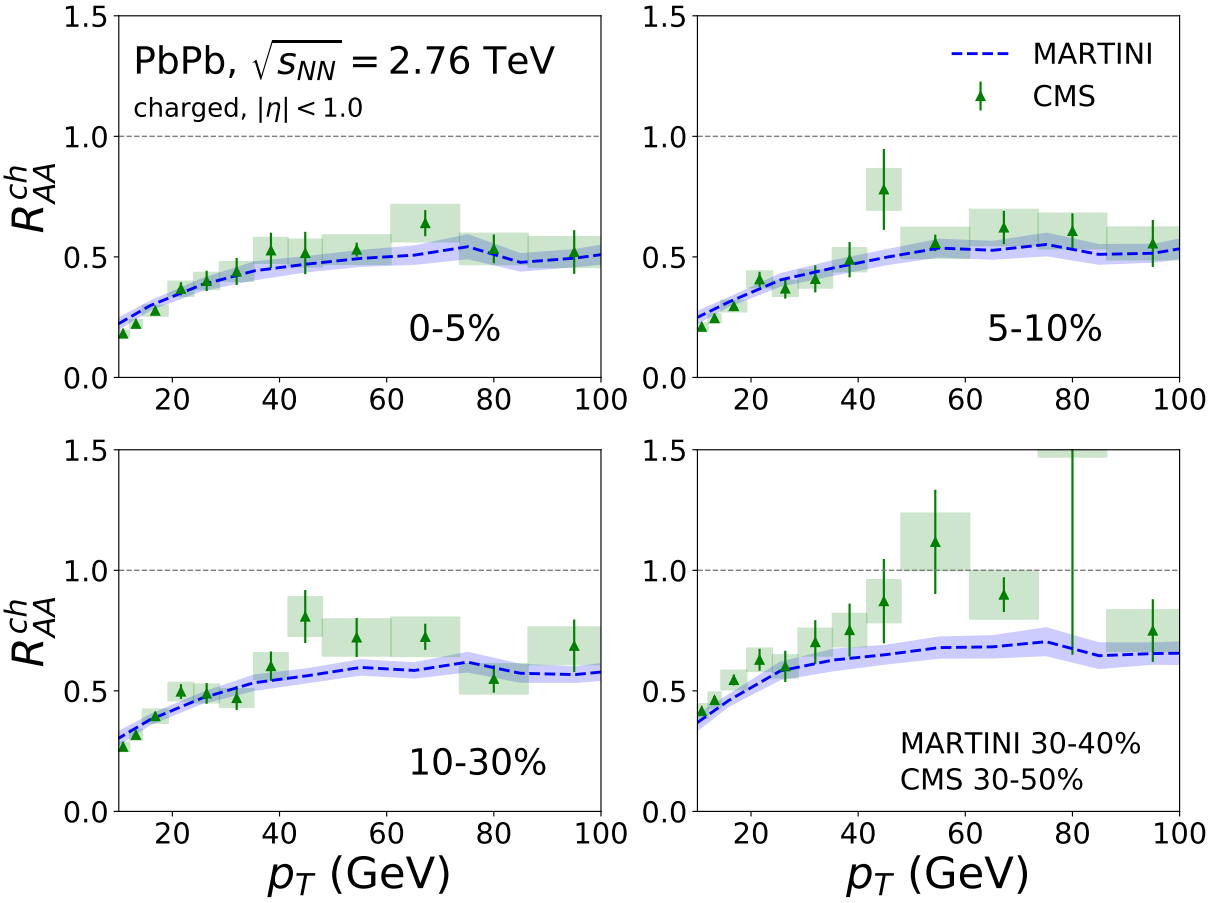

Figure 6.6: Charged hadron R_{AA} for $\sqrt{s_{NN}} = 2.76$ TeV Pb+Pb collisions, averaged over the pseudorapidity range, $|\eta| < 1.0$. We show four centralities, 0-5, 5-10, 10-30, and 30-40%. The blue lines with the statistical uncertainty bands correspond to the MARTINI result using event-by-event hydrodynamic simulation provided by MUSIC [100] and IP-Glasma initial conditions. The green triangles with the y-axis error bars and the shaded boxes represent the CMS measurements [187] and associated statistical and systematic uncertainties, respectively. Note that the centrality bin of the data in the bottom-right panel corresponds to 30-50%.

6.4.1 Centrality dependence

We present the MARTINI results of the charged hadron R_{AA} for $\sqrt{s_{NN}} = 2.76$ TeV Pb+Pb collisions with multiple centrality bins in Fig. 6.6. We simulated event-by-event MUSIC hydrodynamic evolution using 50 unique IP-Glasma initial conditions per 5% centrality

interval[2] , producing a total of 400 different hydrodynamic medium profiles for 0-40% centrality Pb+Pb collisions at $\sqrt{s_{NN}} = 2.76$ TeV. In Fig. 6.6, we performed MARTINI jet evolution using the MUSIC hydrodynamic medium profile in 0-5, 5-10, 10-30, and 30-40% centrality bins. The blue lines correspond to the MARTINI calculations and the shaded band around each line indicates the statistical uncertainties. The CMS measurements are shown as the green triangles with statistical uncertainties. The shaded boxes are the systematic uncertainties from various factors, e.g., detector efficiency and normalization determination[3].

The experimental results reported noticeable suppression of the charged hadron R_{AA} in the four different centrality bins. Our MARTINI calculations with the MUSIC hydrodynamic modelling of the QGP describe the quenched R_{AA} at all centrality bins well. Note that the centrality interval for the calculation is slightly more central than that for the data in the bottom-right panel. This leads to more quenching in the MARTINI results than the data.

These remarkable agreements support creation of the QGP in 0-40% Pb+Pb collisions at $\sqrt{s_{NN}} = 2.76$ TeV. We observed that the jet quenching effect is stronger at lower p_T ranges ($p_T \gtrsim 10$ GeV), i.e., lower values of R_{AA}, while the magnitudes rise at higher p_T ranges. Recalling that the PYTHIA parton shower and the energy loss models implemented in MARTINI are based on perturbative QCD, the low p_T region ($p_T < 10$ GeV) in which pQCD is no longer reliable is excluded from our analysis. The measurements show that the central collisions (0-5%) yield a stronger quenching effect than the peripheral collisions. This indicates that jets propagating through the QGP interact with their surrounding medium less than in peripheral collisions. This is because the overlap zones in peripheral collisions are smaller than those in head-on collisions, creating a smaller

[2]The centrality intervals of our hydrodynamic simulations are determined by the initial condition provided by the IP-Glasma model. Detailed information on the centrality determination procedure can be found in Sec. II B in [3].

[3]Detailed values for each contribution to the systematic uncertainties affecting Pb+Pb and pp collisions are listed in Table 2 in [187]

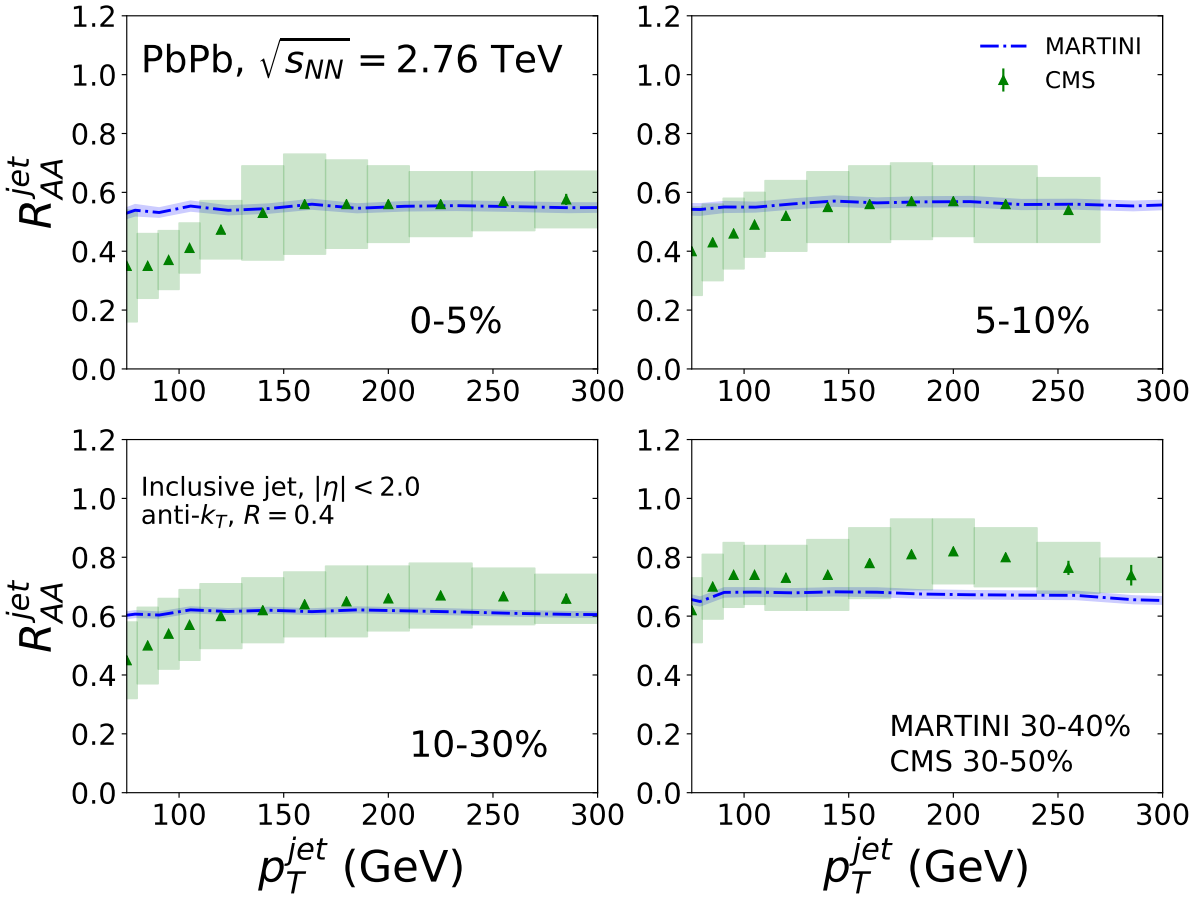

Figure 6.7: Inclusive jet R_{AA} for 2.76 TeV Pb+Pb collisions averaged over the pseudorapidity range, $|\eta| < 2.0$. Each panel shows a different interval in centrality, 0-5, 5-10, 10-30, and $30 - 40\%$. Jets are reconstructed with the anti-k_T algorithm with the radius parameter of $R = 0.4$. The MARTINI results are compared to the CMS measurement [116] with the same color notation as in Fig. 6.6. As in Fig. 6.6, the centrality bin for the data in the bottom-right panel corresponds to 30-50%.

QGP. Our MARTINI model captures the p_T and centrality dependence of charged hadron suppression in $\sqrt{s_{NN}} = 2.76$ TeV Pb+Pb collisions.

Now we investigate the suppression of fully reconstructed jets in heavy-ion collisions. Fig. 6.7 shows the inclusive jet nuclear modification factor R_{AA}^{jet} for $\sqrt{s_{NN}} = 2.76$ TeV Pb+Pb collisions with pseudorapidity $|\eta| < 2.0$. Jets are reconstructed using the inclusive final state hadrons, defined by the anti-k_T algorithm with the radius parameter $R = 0.4$.

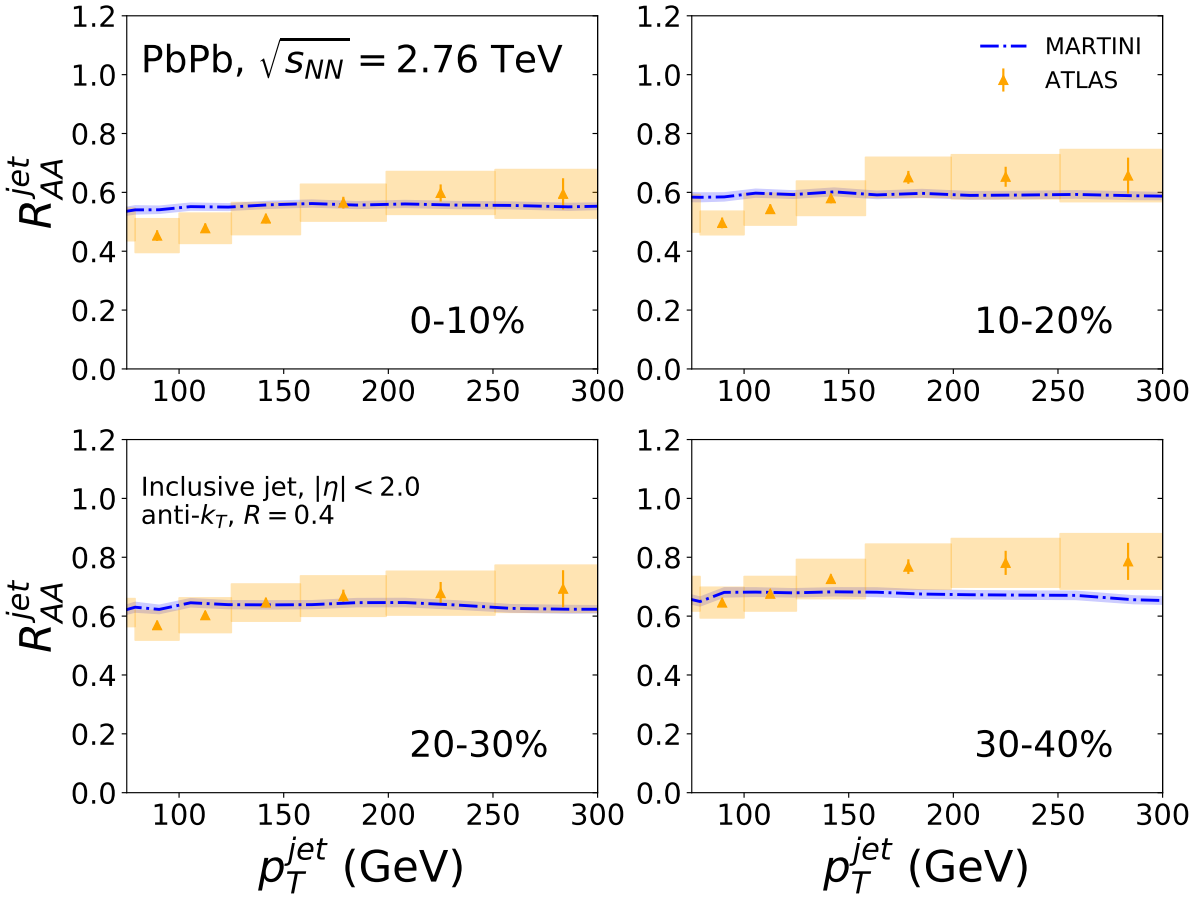

Figure 6.8: Inclusive jet R_{AA} for $\sqrt{s_{NN}} = 2.76$ TeV Pb+Pb collisions with 0-10, 10-20, 20-30, and $30 - 40\%$ centrality intervals. The MARTINI setup for these calculations are identical to that in Fig. 6.7. The MARTINI results are compared to the ATLAS measurement [114].

Each panel shows a different centrality interval, 0-5, 5-10, 10-30, and $30 - 40\%$, compared to the corresponding CMS measurements [116]. As in Fig. 6.6, the centrality intervals for the prediction and the data are slightly different, leading to moderate overestimation of jet energy loss in the MARTINI results. A slight increase of the jet R_{AA} at $75 < p_T < 150$ discussed in Sec. 6.3 appears at peripheral collisions $< 30\%$, while our results are consistently monotonic in the transverse momentum space. We observed a centrality dependence of jet quenching in the jet R_{AA} similar to that in the charged hadron R_{AA}.

We performed a similar comparison analysis using the ATLAS measurements, shown in Fig. 6.8. We divided the centrality intervals to 0-10, 10-20, 20-30, and $30 - 40\%$ for the

direct centrality comparisons. From Fig. 6.7 and Fig. 6.8, we noticed that the centrality dependence of the calculated jet R_{AA} was not clearly visible relative to that of the charged hadron R_{AA} shown in Fig. 6.6. For instance, in the 30-40% centrality bin, our calculation slightly underestimates the measured jet R_{AA} at high p_T. One possible reason for this weak centrality dependence would be the characteristics of the quenching mechanism in MARTINI. When a jet propagates through the QGP, partons in a jet lose their energies through elastic and inelastic processes. However, since the jet is an integrated object consisting of particles inside the predefined jet radius, the main reason for energy loss of jets is momentum broadening, i.e., jet energy dissipation out of the jet area. In MARTINI, the AMY radiative process is strictly collinear, i.e., opening angle of radiation is $\theta \to 0$. Therefore the role of the radiative processes in energy loss of reconstructed jets is to modify the rate of elastic scattering, only indirectly influencing the energy loss behaviour. This might cause the smaller centrality dependence of the jet R_{AA} in the MARTINI results. Nonetheless, we found qualitative agreements between the calculations and the measurements within the uncertainty range.

6.4.2 Jet radius dependence

Jets with larger jet radius parameter R have wider area in the ϕ-η space to contain hadrons and tend to get more reconstructed energies. This leads the differential jet cross-section shown in Fig. 6.3 (right panel) to a roughly longitudinal shift to higher energies. With increasing R, the jet R_{AA} values would remain unchanged if the effect of jet quenching is independent of the distance from the jet axis. Thus, the jet quenching analysis with varying the jet radius parameter R provides an opportunity to investigate differential jet energy loss versus the distance from the jet axis.

The MARTINI calculations of jet R_{AA} with various jet radius parameters R are shown in Fig. 6.9. Each panel in Fig. 6.9 shows the jet R_{AA} with $R = 0.2$, 0.3, and 0.4 compared to the CMS measurements [116]. We observe higher values of the jet R_{AA} with increasing R for all centrality bins. This suggests weaker jet quenching effects with increasing dis-

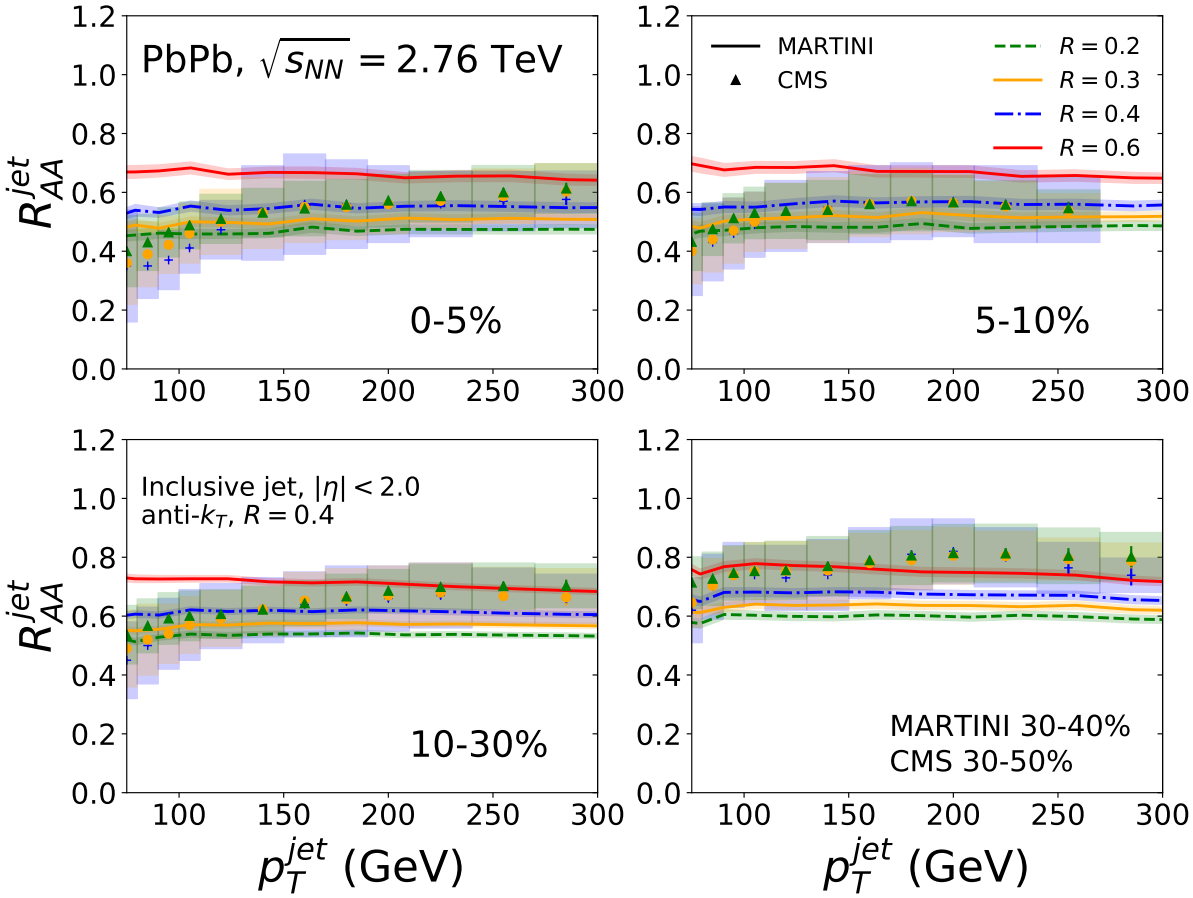

Figure 6.9: Inclusive jet R_{AA} for $\sqrt{s_{NN}} = 2.76$ TeV Pb+Pb collisions with different jet radius parameter $R = 0.2$, 0.3, and 0.4, compared to the corresponding CMS data [116]. Additionally we present our results with $R = 0.6$ to investigate the R dependence at larger R. Each panel shows centrality intervals of 0-5, 5-10, 10-30, and 30-40%. The jet R_{AA} with $R = 0.4$ in each panel is same as that shown in Fig. 6.7.

tance from the jet axis. We will show that the recoils and holes largely contribute to this behaviour of jet quenching in Sec. 6.5.

Although the uncertainty bands in the measurements are quite sizable, we noticed weak R dependence of the jet R_{AA} in the data and the predictions. The jet density distribution as a function of distance from the jet axis we will present in the next section (Sec. 6.5) describes that the majority of jet energy is concentrated within $R < 0.2$ in MARTINI. In this regard, the reason for this weak R dependence of the jet R_{AA} is because the jet

R_{AA} is mainly constrained by the jet quenching effect in $R < 0.2$. As an extended analysis, we additionally show the results with $R = 0.6$ depicted in the red lines. The results are consistent with our observation that a larger jet radius yields smaller quenching in the jet R_{AA}.

While the jet R_{AA} with $R \leq 0.4$ have negligible p_T dependence in all centrality bins, we observed slight enhancement at low p_T of $R = 0.6$, causing negative slopes for the jet R_{AA}. The interpretation of this originates from the implementation of thermal recoils in MARTINI. As we discussed in Sec. 5.3.2, when a thermal recoil parton is created during elastic scattering, an artificial parton representing an incoming thermal parton, a hole, is also produced to conserve total energy in the collision process. Since these holes do not re-scatter in the MARTINI evolution, i.e., free streaming, they are not hydrodynamically diffused before they are hadronized. This may underestimate the total energy of the holes to be subtracted from the jet signal. We expect this underestimation is more likely to be strong for jets with larger R and low p_T.

6.4.3 Jet quenching at 5.02 TeV

So far we have studied suppression of jets produced in Pb+Pb collisions at $\sqrt{s_{NN}} = 2.76$ TeV, the first collisions of Pb nuclei delivered by the LHC at the end of 2010. Following the Run I period, the LHC proceeded with the Run II program to record Pb+Pb collisions at $\sqrt{s_{NN}} = 5.02$ TeV at the end of 2015 and 2018. The increased centre-of-mass energy of heavy-ion collisions allows us to access an energy density that should create a denser, hotter, and longer-lived QGP medium [239]. From a theoretical perspective, studying heavy-ion collisions at different centre-of-mass energy is an exceptional opportunity to pin down the physics behind the measurements and constrain model parameters.

For the analysis of Pb+Pb collisions at $\sqrt{s_{NN}} = 5.02$ TeV, we simulated 500 event-by-event hydrodynamic events with IP-Glasma initial conditions for the 0-50% centrality interval. We initialized the hydrodynamic modelling with the equations of state provided by the HotQCD Collaboration [50] as mentioned earlier in Sec. 6.1 and the initialization

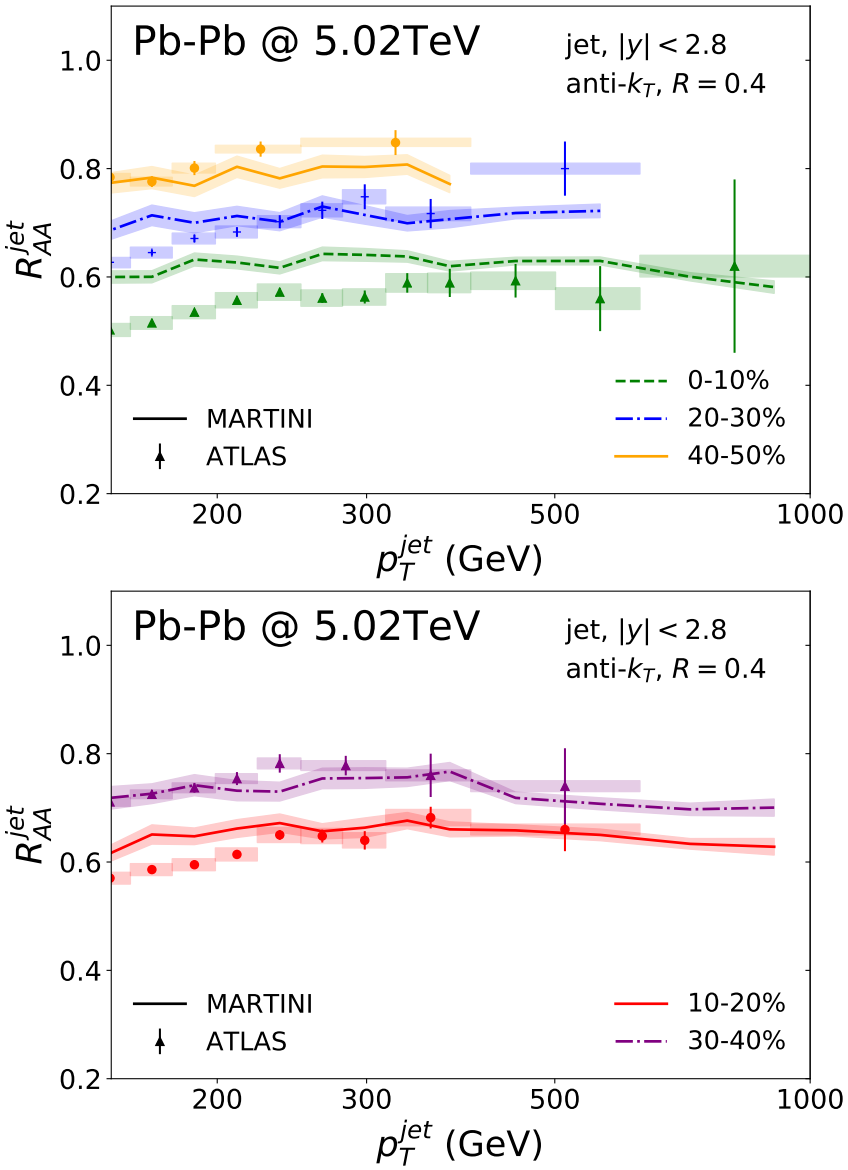

Figure 6.10: Inclusive jet R_{AA} for $\sqrt{s_{NN}} = 5.02$ TeV Pb+Pb collisions with rapidity $|y| < 2.8$ compared to the data measured by the ATLAS collaboration [238]. The top panel shows three different centrality intervals, 0-10, 20-30, and 40-50%, and the bottom panel shows two other centrality intervals, 10-20, and 30-40%.

time of $\tau_0 = 0.4$ fm. The PDF sampling in PYTHIA is carried out with an identical setup to those for $\sqrt{s_{NN}} = 2.76$ TeV collisions with CTEQ6L [113] parton distribution functions and EPS09LO [121] nuclear PDFs.

Using this model setup, we calculated the jet R_{AA} for 5.02 TeV Pb+Pb collisions as shown in Fig. 6.10. We show the jet R_{AA} at 0-10, 20-30, and 40-50% centrality intervals in the top figure, and 10-20 and 30-40% centrality intervals in the bottom figure. The reconstructed jets contain inclusive final state particles determined using the anti-k_T algorithm with $R = 0.4$. For each centrality result, we made comparisons with the corresponding ATLAS measurements [238].

We observe a general trend of the increasing jet R_{AA} with jet p_T from the ATLAS measurements at all the centrality intervals up to 50%. Our MARTINI results show weak p_T dependence, resulting in a deviation from the measurements especially at lower jet p_T in the 0-10% most central collisions. At higher jet p_T the discrepancy tends to diminish. This insensitivity to p_T shown in the calculations implies that the reconstructed jets in MARTINI are more collimated within the jet radius than the measured jets. Determining the jet energy is sensitive to the spatial distribution of final-state particles in the pseudorapidity η and azimuthal ϕ space. In MARTINI, this distribution is affected by the elastic collisions and consequently sampled recoils (and holes), whose energies are of the same order as the temperature of the QGP. Examination of the soft constituents of the reconstructed jets would give a better understanding of the discrepancy we observed from the jet R_{AA} analysis in 5.02 TeV Pb+Pb collisions.

6.5 Medium recoils and jet modifications

In our previous analyses, we presented the predictions with the implementation of thermal recoils. In this section, we discuss the effects of thermal recoils and their role in studying jet quenching in heavy-ion collisions. Thermal recoils, originating from a thermal medium, are scattered by energetic jet partons through elastic scattering processes. As a result, a certain amount of jet energy is transferred to those thermal recoils, which then evolve in the thermal medium. Since momentum broadening plays an important

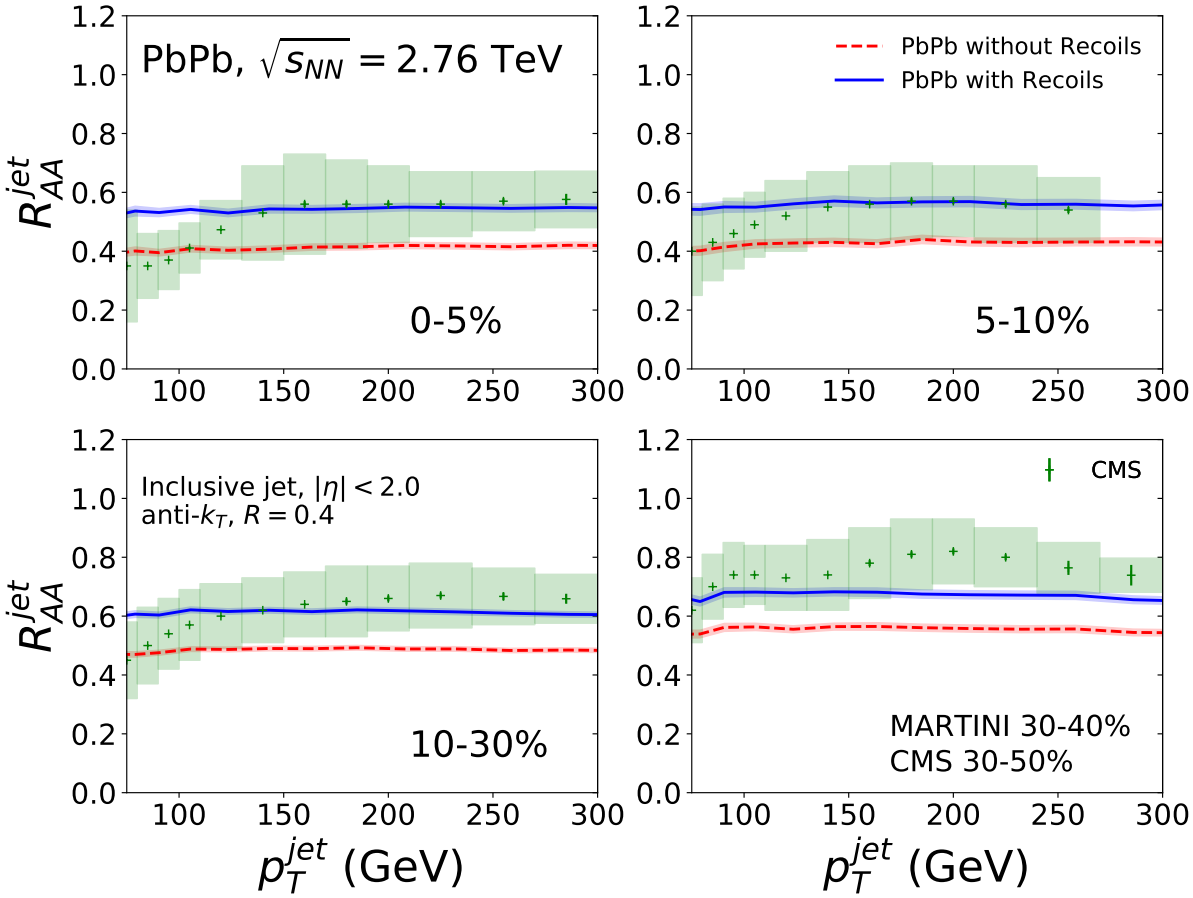

Figure 6.11: Inclusive jet R_{AA} for $\sqrt{s_{NN}} = 2.76$ TeV Pb+Pb collisions at four different centrality bins, compared to the CMS measurements [116]. We plot the results with recoils and holes in red and without them in green.

role in energy loss of fully reconstructed jets, exploring the effect of thermal recoils would give us plenty of valuable information on how jets lose energy in the medium.

To quantify the effect of recoils in the jet observables, we made comparisons between two sets of jets; i) one reconstructed by inclusive partons including hard partons, recoils, and holes and ii) by hard partons only. In Fig. 6.11, we show the jet R_{AA} for $\sqrt{s_{NN}} = 2.76$ TeV Pb+Pb collisions obtained from MARTINI simulations with and without thermal recoils. In all the centrality intervals, we observe a clear separation between jets with recoils and without recoils. For instance, the thermal recoils enhance the magnitudes of the jet

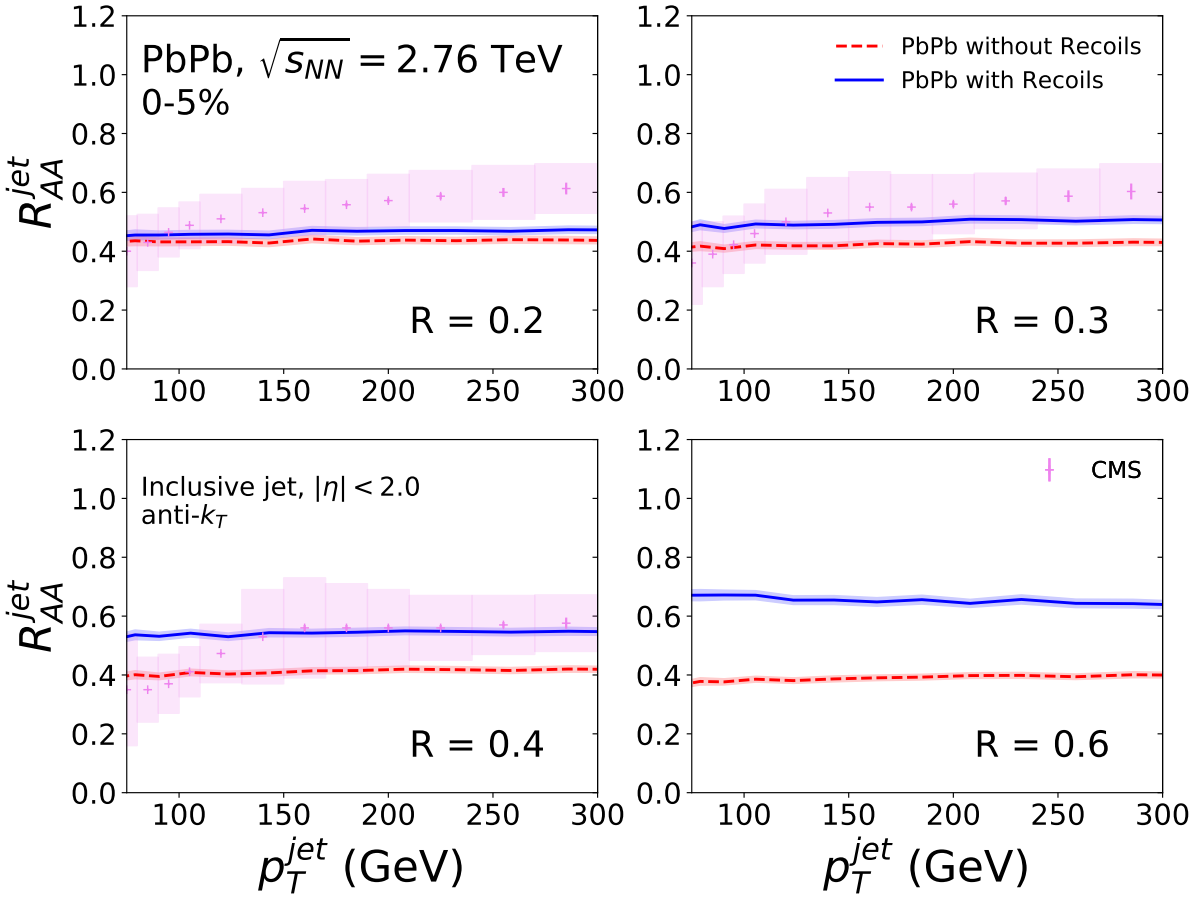

Figure 6.12: Inclusive jet R_{AA} for 0-5% Pb+Pb collisions at $\sqrt{s_{NN}} = 2.76$ TeV with recoils and holes (red) and without them (green). Each panel shows four different sizes of the jet radius parameter, compared to the CMS measurements [116].

R_{AA} by ~ 0.15 in the most central collisions (0-5%), while similar effects were observed in other centrality bins. This enhancement does not induce any jet p_T dependence.

In Fig. 6.12, we show the comparisons with and without thermal recoils using various sizes of the jet radius from $R = 0.2$ to 0.6. The difference in magnitudes between the jet R_{AA} with and without recoils is small for jets with $R = 0.2$, while the deviation becomes significant at larger R. We found more than a 50% increase in the magnitude of the jet R_{AA} with $R = 0.6$. This is because jets with a larger radius parameter are more likely to contain more recoiling particles, restoring more energies from those thermal recoils. However, the CMS measurements show the jet R_{AA} independent of the size of the jet

radius, which yields moderate discrepancy at smaller R. In the right-bottom panel, where the jet radius R is the largest, the enhancement observed at low p_T disappears when the thermal recoils and holes are excluded. This confirms the argument we made in Sec. 6.4.2 that the enhancement originates from the underestimation of holes inside the jet area, owing to the lack of re-scattering processes.

We examine the contribution of thermal recoils to reconstructed jets by analyzing differential jet observables, such as the jet shape function and jet mass. The following subsection introduces the jet-structure observables and presents our results.

6.5.1 Jet shape function

The jet shape function $\rho(r)$ describes the radial distribution of jet momentum density inside the jet area, defined as [240]

$$\rho(r) = \frac{1}{\delta r}\frac{1}{N_{jet}}\sum_{jet}\frac{\sum_{trk\in[r_a,r_b)} p_T^{trk}}{p_T^{jet}}, \tag{6.6}$$

where a given jet radius is divided by annulus bins with radial width of $\delta r = 0.05$. $r_a = r - \delta r/2$ and $r_b = r + \delta r/2$ are the inner and outer radius of each radial bin, respectively. r is the radial distance between each particle (track) and the jet axis, given by

$$r = \sqrt{(\eta_{trk} - \eta_{jet})^2 + (\phi_{trk} - \phi_{jet})^2} \leq 0.3 \tag{6.7}$$

Note that since the reconstructed jets do not always have a perfect circular shape, the particles satisfying the $r < 0.3$ condition do not coincide with the constituents of the jet.

In this analysis, we reconstructed inclusive jets using the anti-k_T algorithm with the distance parameter $R = 0.3$. We then selected jets with $p_T^{jet} > 100$ GeV and $0.3 < |\eta| < 2.0$. The mid-rapidity region, $|\eta| < 0.3$, was excluded in the analysis because of the "η-reflected" method [116,241] used by the CMS collaboration to estimate contributions from background. The jet shape function $\rho(r)$ was evaluated using charged hadrons with $p_T^{ch} >$

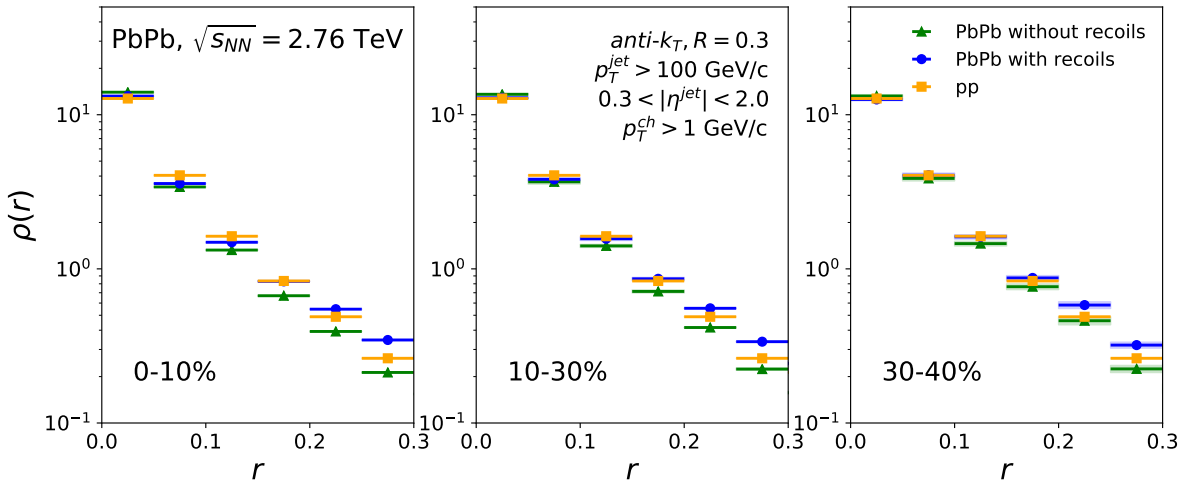

Figure 6.13: The jet shape function $\rho(r)$ for Pb+Pb collisions at $\sqrt{s_{NN}} = 2.76$ TeV with recoils and holes (blue) and without them (green). Each panel shows different centrality intervals, 0-10, 10-30, and 30-40%. The reconstructed jets are defined by the anti-k_T algorithm with the jet radius parameter of $R = 0.3$. We also plot the pp results as a reference.

1 GeV. After calculating the jet shape, the integral of jet shape over the range $0 \leq r \leq R$ is normalized to unity.

Fig. 6.13 shows the jet shape function for 2.76 TeV Pb+Pb collisions at the 3 different centrality intervals. Similar to the jet R_{AA} analysis in the previous section, we plot the results with and without the recoil feature in our MARTINI simulations to visualize the effect of recoil in our observables. We plot the pp results without the hydrodynamic medium as a reference. We notice that the jet shape density peaks at the centre of the jet and steeply falls when moving away from the jet axis. This shows that most of the energy inside a jet radius is concentrated near the jet axis. For example, more than 80% of energy in a jet from pp collisions is located within $r < 0.1$. This is further supported by the small-angle dominant vacuum and in-medium parton shower processes.

When switching from pp to Pb+Pb calculations we observe two competing effects on forming the jet shape function $\rho(r)$. On the one hand, jet energy loss mechanisms suppress the jet shape function, as shown from the green plots (the case with hydrodynamic medium and without medium recoiling particles). The density depletion is weaker at

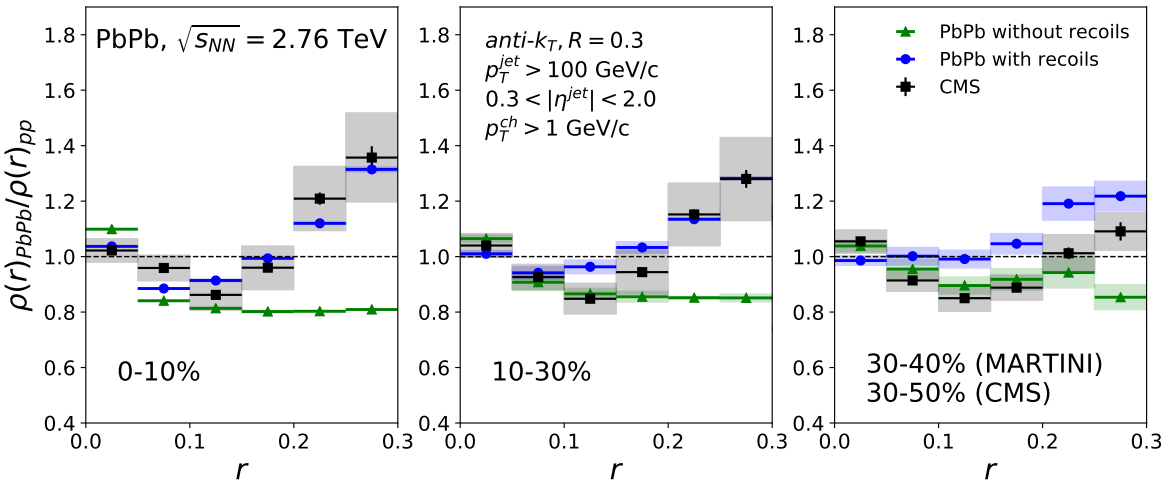

Figure 6.14: The ratio of jet shape function between Pb+Pb and pp collisions at $\sqrt{s_{NN}} = 2.76$ TeV with recoils and holes (blue) and without them (green). Each panel shows different centrality intervals, 0-10, 10-30, and 30-40%. The reconstructed jets are defined by the anti-k_T algorithm with the jet radius parameter of $R = 0.3$. We compare our results to the CMS measurements [240].

peripheral centrality intervals because of smaller medium effects. Since the jet shape is defined to be self-normalized, the decrease in density at large r leads to slight increases at the first bin, $r < 0.05$. On the other, the inclusion of recoiling particles helps to develop the jet density, especially at large r regions. Thermal recoils are dissipated by in-medium processes and they are more likely to be located at large r.

In Fig. 6.14, we plot the ratio of the jet shape function between Pb+Pb and pp collisions. Our results illustrate two competing effects: the jet energy depletion because of the medium effect (green triangles) and the density increase from the inclusion of the thermal recoils (blue circles). The role of medium recoil is significant at the high r of the ratio plot. Their contributions result in a rise of the jet shape ratio starting from $r = 0.15$. The medium effects combined with thermal recoils determine the non-monotonic ratios of the jet shape function between Pb+Pb and pp. Our full calculations with thermal recoil (blue circles) captures the general trend of the CMS measurements [240]. We found the largest contributions from thermal recoils in central collisions where the medium ef-

fects are largest. We observe a consistent behaviour of the centrality-dependent medium effects in the analysis of the jet nuclear modification factor and the jet shape function.

6.5.2 Jet mass

The mass of a reconstructed jet is defined as [242, 243]

$$M = \sqrt{E^2 - p_T^2 - p_z^2}, \tag{6.8}$$

where E is the total energy of the jet, and p_T and p_z are transverse and longitudinal momentum of the jet, respectively. Since a jet comprises particles from parton shower, the jet mass in Eq. (6.8) is closely related to the virtuality (off-shellness) of the original parton of the shower [242]. Since the four-vector of the jet is sensitive to the jet quenching in the QGP, its invariant mass provides additional information that characterizes their properties.

In the jet mass analysis, jets were constructed using charged particles with $0.15 < p_T^{ch} < 100$ GeV. We used the anti-k_T algorithm with the jet radius parameter of $R = 0.4$. Since the jet mass is related to the initial virtuality of the initial single-parton jet, we collected jets using different kinematic cuts on p_T^{jet} to examine a differential feature of the jet mass. We present our MARTINI results of the normalized jet mass distribution for 0-10% Pb+Pb collisions at $\sqrt{s_{NN}} = 2.76$ TeV in Fig. 6.15. We observe that the peak of the distribution moves toward higher jet mass as p_T of jets increase. The distribution of the jet mass with higher p_T^{jet} was broader than those with lower p_T^{jet} because of larger jet-by-jet fluctuations in the parton shower. We notice that the jet mass for pp and Pb+Pb collisions is similar to each other. This is because of the two competing effects on the shape of the jet mass distribution – loss of the jet mass because of jet quenching (green) and gain of the jet mass attributed from thermal recoils (red).

In Fig. 6.16, we show the average jet mass with and without recoils for the three different jet p_T intervals. We observe an increasing trend of the average jet mass as a function

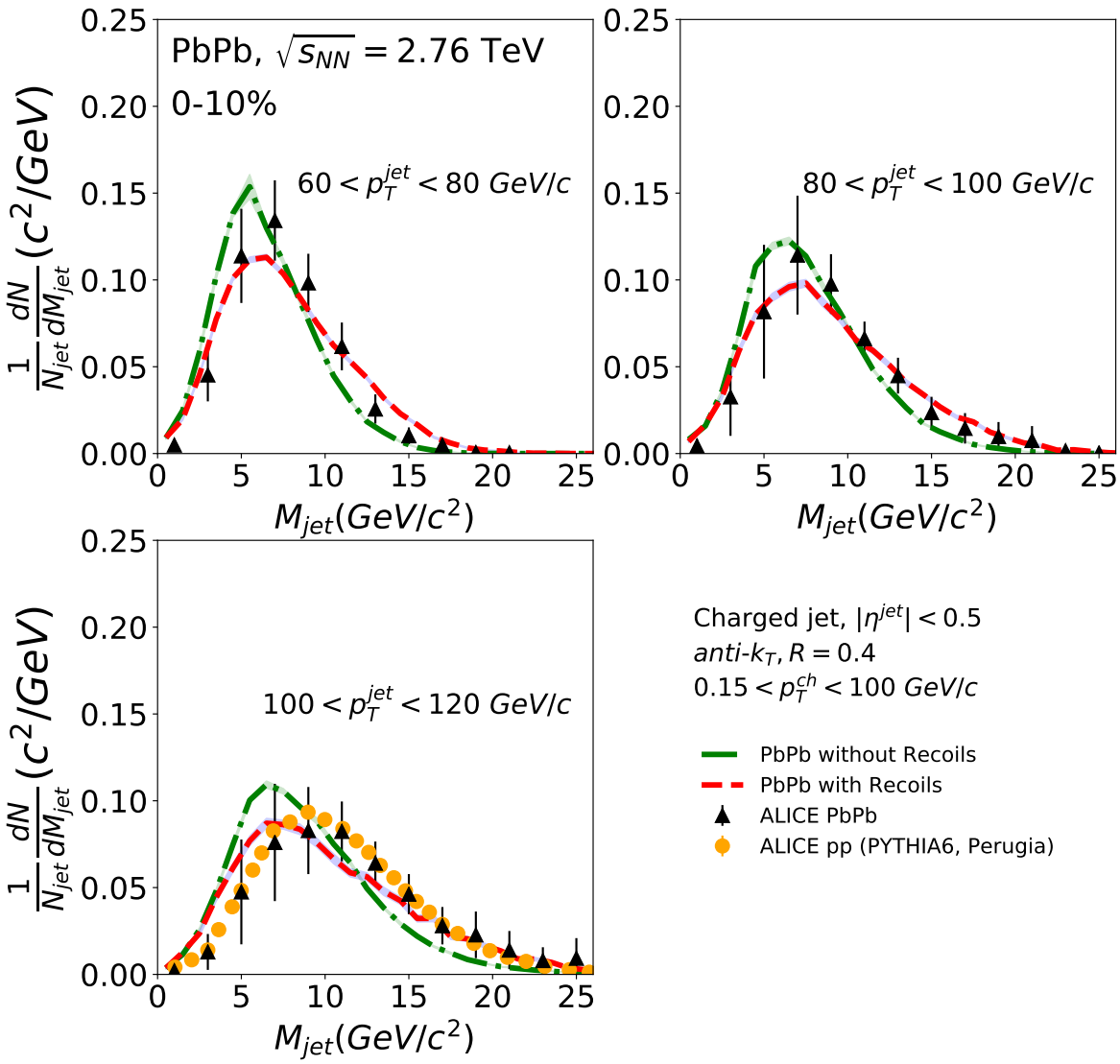

Figure 6.15: The jet mass distribution for 0-10% Pb+Pb collisions at $\sqrt{s_{NN}} = 2.76$ TeV with recoils and holes (red) and without them (green). Each panel shows different jet p_T intervals: 60-80, 80-100, and 100-120 GeV. The reconstructed jets are defined by the anti-k_T algorithm with jet radius parameter $R = 0.4$. We compare our results to ALICE measurements [243]. In the bottom-left figure, we show the PYTHIA pp results from the ALICE collaboration for the comparison purpose.

of jet p_T. Although the results underestimate the average jet mass at $100 < p_T^{jet} < 120$ GeV, thermal recoils play an essential role in describing the measured jet mass. We observed that their contributions were negligible at low jet p_T and became noticeable at high p_T.

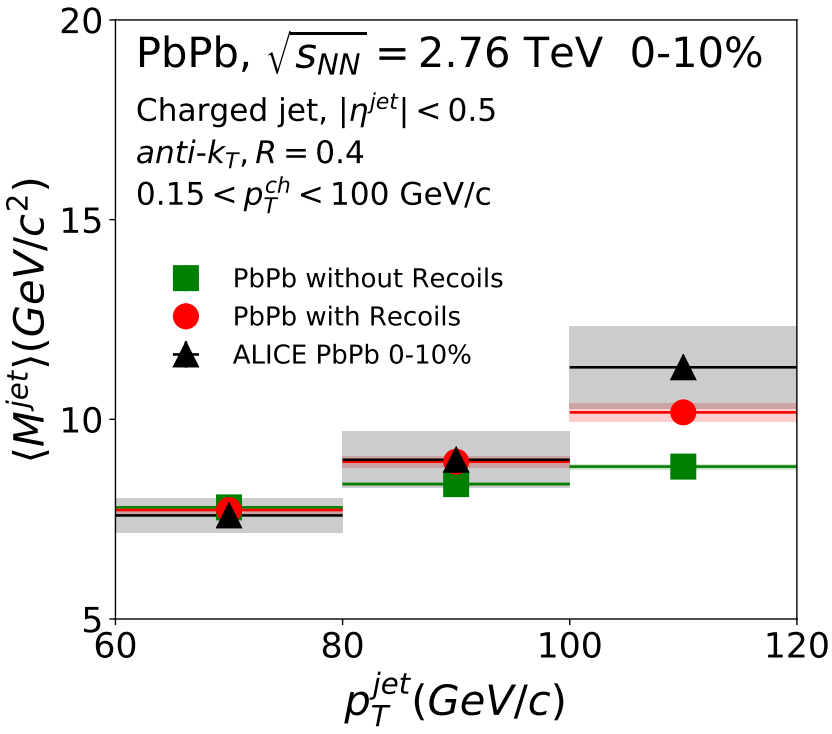

Figure 6.16: The average jet mass for 0-10% Pb+Pb collisions at $\sqrt{s_{NN}} = 2.76$ TeV with recoils and holes (red) and without them (green) as a function of jet p_T. We compare the MARTINI results to the ALICE measurements [243].

6.6 Summary

In this chapter, we have studied jet modifications caused by the QGP created in heavy-ion collisions using our Monte-Carlo event generator, MARTINI. With the AMY radiative energy loss and collisional energy loss processes implemented in MARTINI we have reproduced the jet observables measured by the experiments at the LHC. We have analyzed the sensitivity of the integrated and differential jet observables to the jet modification via jet-medium interactions. Event-by event fluctuation of the background was simulated via the $3+1$ dimensional viscous hydrodynamic model, MUSIC, together with IP-Glasma initial conditions. To achieve realistic jet production rates in PYTHIA, we applied CTEC6L [113] parton distribution functions and EPS09LO [121] nuclear PDFs. With this setup, we ob-

tained at most 20% deviation in our PYTHIA simulation from the experimental measurements of the differential charged hadron yield and jet cross-section.

The analysis of the finite formation time of radiation (5.2.1) and the QCD running coupling scheme (5.3.1) revealed that the running coupling is the dominant influence on jet quenching while both effects play essential roles in describing the nuclear modification of charged hadrons and reconstructed jets. This confirms that our MARTINI jet quenching model provides reasonable descriptions of charged hadron and jet observables in 2.76 TeV Pb+Pb collisions.

We examined jet quenching at different centrality intervals and jet radius parameters. We observed smaller quenching in the charged hadron and the jet R_{AA} at peripheral collisions compared to that at central collisions caused by the smaller size of the medium and lower peak temperatures. Larger jet radius also led to smaller suppression of the jet R_{AA}. This is because thermal recoils in our simulations partially restore jet energies. Direct comparisons between the cases with and without thermal recoils revealed that their contribution increases with larger jet radius. However, the experimental results reported that jet quenching was insensitive to the jet radius R.

The findings from our analysis of the thermal recoils are further supported by analyzing the jet intra-jet observables such as jet shape function and jet mass. By comparing our computations of the jet shape function with and without the thermal recoils, we established the results are substantially sensitive to the thermal recoils at central collisions (up to a 30% change). The non-trivial ratio of the jet shape function between Pb+Pb and pp was induced by the two competing effects: depletion by jet quenching and enhancement at large r contributed from thermal recoils. The jet mass consistently showed these competing effects, resulting in a larger jet mass. The jet mass calculations derived a similar conclusion that both effects play an essential role in describing the jet mass for higher p_T jets.

While we obtained reasonable descriptions of various jet-related observables as presented in this chapter, we also detected a minor discrepancy in our calculations when

comparing to corresponding experimental measurements. For example, we observed that our model does not show a sufficient increase in average jet mass as shown in Fig. 6.16 for the last jet p_T bin (100-120 GeV). This is a direct consequence of our implementation of the thermal recoils and holes in our MARTINI simulations. Recalling the description in Sec. 5.3.2, a hole is created together with the corresponding thermal recoil for energy-momentum conservation in the system, and they do not interact with the medium. This simplified implementation leads to an inadequate energy distribution of holes in the ϕ-η plane. Technically, a hole represents a space for the thermal parton kicked by a jet. Hence it is more reasonable to simulate their evolution hydrodynamically based on a strongly coupled approach, which is a future task.

In the next chapter, we will explore the signature of QGP creation in small systems such as p+Pb collisions using our jet quenching model. We will examine each source of jet modification in small systems and discuss the sensitivity of jet-medium interactions to describe jet observables in small systems.

Chapter 7

Search of QGP in small systems

In heavy-ion collisions, high-energy QCD jet production serves as a reliable probe of QGP created in the collisions. In the previous chapter, we analyzed how jets created at the initial stage of collisions are modified as they traverse the QGP. Specifically, we have demonstrated the performance of our MARTINI model in describing jet quenching phenomena in Pb+Pb collisions. The primary purpose of this chapter is to extend an understanding of jet modification to small systems such as p+Pb collisions to explore the possibility of QGP creation in small systems.

The study of quark-gluon plasma in small systems is puzzling because many experiments have reported diminishing jet energy loss in these colliding systems [197,244–253], while plentiful evidence of flow characteristics has also been observed at the central collisions of small systems [254,255]. Some research on small systems has argued multiple sources of bias in centrality determination [245,256]. Bias effects distort the measurements of the nuclear modification factor in central and peripheral collisions of small systems. For more details, see Sec. 4 and 5 in [245]. Thus, although small systems show collective properties at central collisions, it is not straightforward to perform theory-experiment comparisons at central collisions where the medium effects are expected to be largest.

In this chapter, we applied our framework of jet simulation to minimum bias p+Pb collisions at 5.02 TeV to study the medium effects that we have observed in Pb+Pb collisions.

We first discuss the evidence of collectivity observed in small colliding systems in Sec. 7.1. These observations suggest the possibility of QGP creation in small systems. In Sec. 7.2, we present the results of hydrodynamic simulations of p+Pb collisions with Monte-Carlo Glauber [85–87] initial conditions. Sec. 7.3 reports the results of our MARTINI jet evolution on small systems with small droplets of the QGP. We present the jet production rates at different rapidities to quantify non-monotonic nuclear effects in asymmetric colliding systems. Then we study the importance of the recoils in calculating jet observables in small systems. Sec. 7.5 summarizes our results presented in this chapter and discusses the implications in terms of QGP creation in small systems.

7.1 Collectivity in small systems

As we discussed in Sec. 4.2, collective properties arise from anisotropic thermal pressure in colliding systems and are an important signature of QGP creation. The CMS collaboration has reported that the coefficients of the elliptic flow at p+Pb collisions are comparable to those at Pb+Pb collisions [245]. Fig. 7.1 shows the elliptic flow coefficients v_2 as a function of event multiplicity N_{trk} derived using various methods from the CMS collaboration [245, 257]. The left and right panels compare those values for 2.76 TeV Pb+Pb and 5.02 TeV p+Pb collisions with an identical multiplicity range. The Pb+Pb values are consistently higher than corresponding values in p+Pb collisions, but they are qualitatively comparable to each other. This supports the collective nature of both the Pb+Pb and p+Pb collisions.

The PHENIX collaboration has conducted systematic studies in many small colliding systems at the RHIC in the small systems geometry scan [260] to pin down the source of anisotropic momentum flow in small systems. In the experiments, small nuclei with different geometric shapes, e.g., a proton, deuteron, or Helium-3, were collided with Au nuclei. The left panel of Fig. 7.2 illustrates the average spatial eccentricities ϵ_2 and ϵ_3 for small impact parameter p+Au, d+Au, and ^{3}He+Au collisions obtained from the Monte-Carlo

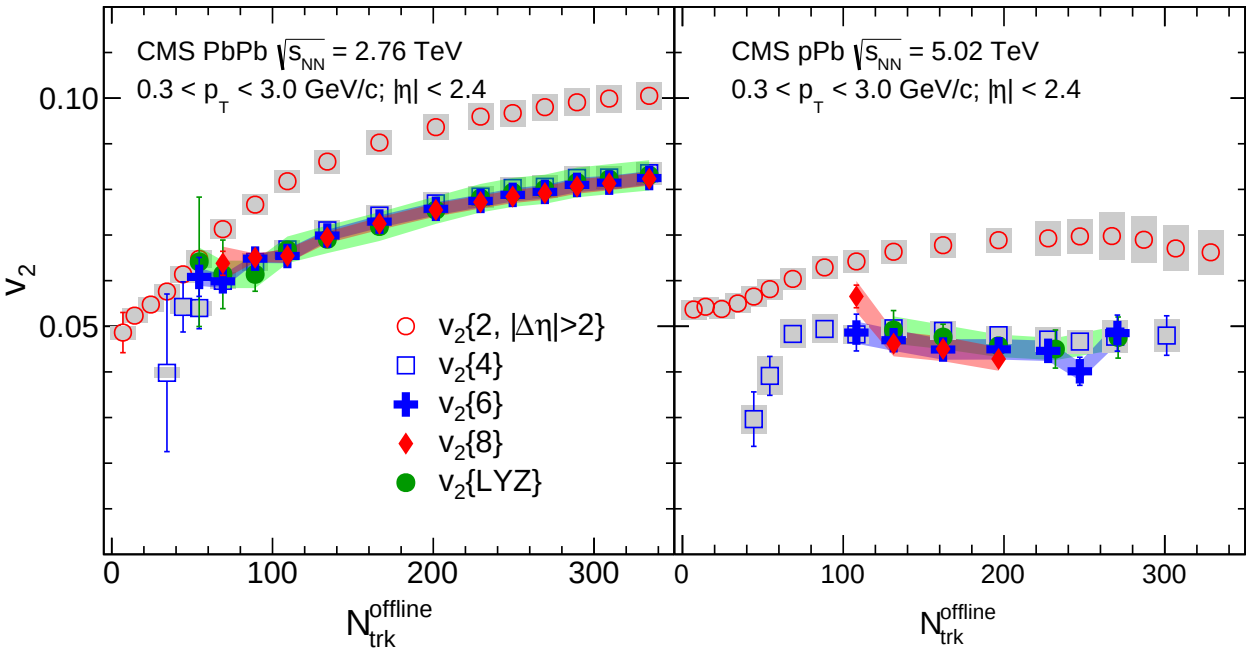

Figure 7.1: The elliptic flow coefficients v_2 measured as a function of N_{trk} obtained from the two- and four-particle cumulant methods presented in [257] are shown with open data points. The v_2 results from the six- and eight-particle cumulant methods and the LYZ method [258, 259] are displayed with solid points. The left panel shows Pb+Pb collisions at 2.76 TeV and the right panel is p+Pb collisions at $\sqrt{s_{NN}} = 5.02$ TeV. The figure is reproduced from [245].

Glauber model. According to the study, the elliptical and triangular initial geometries of d+Au and ^{3}He+Au collisions are characterized by the ϵ_2 and ϵ_3 signals, while the values in p+Au collisions are purely driven by fluctuations. As shown in the left panel of Fig. 7.2, the PHENIX measurements reported the largest ϵ_2 and ϵ_3 from d+Au and ^{3}He+Au collisions, respectively. The sizable values of ϵ_2 and ϵ_3 in p+Au collisions indicate that initial geometric fluctuations have a significant effect in determining the spatial eccentricities. The right panel of Fig. 7.2 shows the measured v_2 and v_3 as a function of p_T in the 0-5% most central collisions of p+Au, d+Au, and ^{3}He+Au systems at $\sqrt{s_{NN}} = 200$ GeV. This confirms that the colliding system ordering of eccentricities is directly translated into the

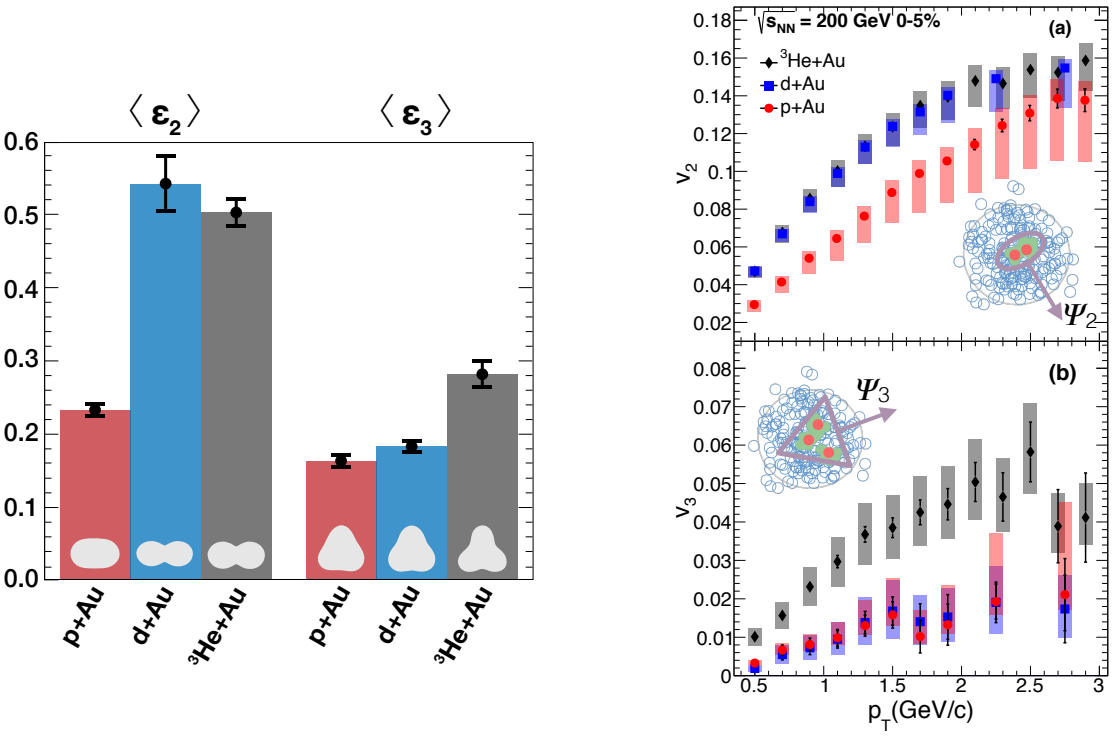

Figure 7.2: (Left panel) Average spatial eccentricities ϵ_2 and ϵ_3 for p+Au, d+Au, and ^{3}He+Au colliding systems from a Monte Carlo Glauber model. (Right panel) Measured elliptic and triangular harmonic flow coefficients v_2 (Right top) and v_3 (Right bottom) as a function of p_T in the 0-5% central collisions of the three small colliding systems at $\sqrt{s_{NN}} = 200$ GeV. A Monte-Carlo Glauber model depicting an elliptical (ψ_2) and a triangular (ψ_3) symmetric plane angle is inserted in the top and bottom panels, respectively [260].

anisotropic harmonic flow coefficients in those systems as follows:

$$v_2^{\text{p+Au}} < v_2^{\text{d+Au}} \approx v_2^{^3\text{He+Au}} \tag{7.1}$$

$$v_3^{\text{p+Au}} \approx v_3^{\text{d+Au}} < v_3^{^3\text{He+Au}} \tag{7.2}$$

The results in Fig. 7.2 support the strong correlations between spatial geometries of the colliding systems and the final-state momentum anisotropies.

Given the apparent source of the momentum anisotropic flows, Fig. 7.3 compares the experimental measurements to the two different hydrodynamic simulations [4, 261]. Al-

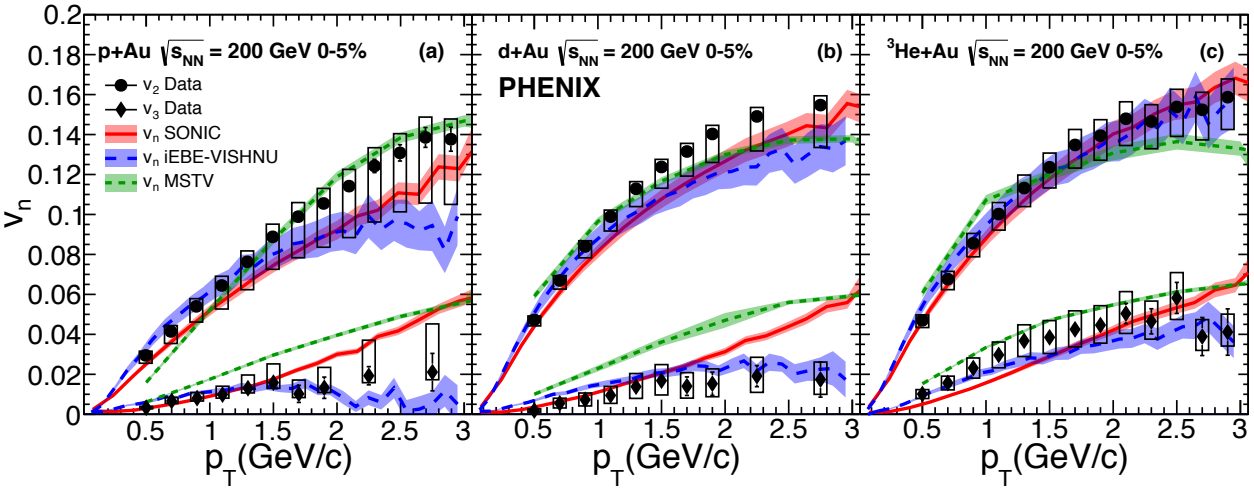

Figure 7.3: The v_2 and v_3 measurements as a function of p_T for charged hadrons in 0-5% central ^{3}He+Au collisions at $\sqrt{s_{NN}} = 200$ GeV compared with various theoretical calculations [260].

though the two hydrodynamic models have their own implementations of treating fluctuations in the initial geometry, their predictions are consistent with the v_2 measurements and the magnitude separation between v_2 and v_3. The comparison of results in Fig. 7.3 confirms the reliability of hydrodynamic approaches in predicting final-state momentum anisotropic flow[1].

7.2 Initial conditions and hydrodynamic modelling

In this section, we present the results of hydrodynamic simulations for p+Pb collisions as an ingredient of our jet evolution scheme. As discussed in the previous section, the final-state flow properties are largely caused by initial geometries and fluctuating configurations of the colliding systems. To take initial eccentricities into account in our simulation, we have used the Monte-Carlo Glauber model for the initial condition.

[1]The reliability argument of hydrodynamics in small systems is valid only for high multiplicity events, $N_{trk} \gtrsim 70$, and the extension to low multiplicities leaves challenging issues. This originates from a large deviation from equilibrium and short-lived evolution. For more details, see Ref. [262] and references therein. The validity of fluid dynamics in small systems has been discussed and qualitatively estimated. See Appendix A in [4]

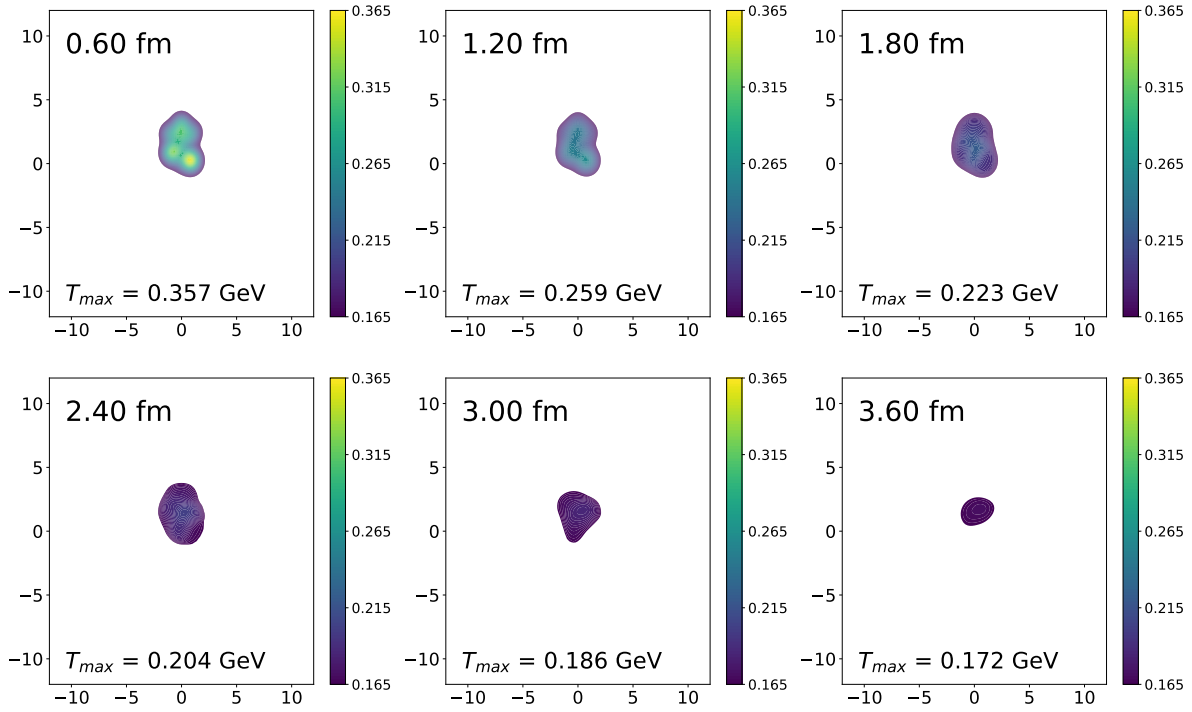

Figure 7.4: Temperature distributions in the transverse plane at mid-rapidity at different times obtained by MUSIC [100] simulations with Monte-Carlo Glauber initial conditions in 0-5% Pb+Pb collisions at $\sqrt{s_{NN}} = 2.76$ TeV. The initialization time of the hydrodynamic simulation is $\tau = 0.6$ fm and the freeze-out temperature of the system is $T_c = 0.165$ GeV. The freeze-out time of the evolution is estimated as $\tau \sim 3.6$ fm.

Fig. 7.4 depicts the temperature distributions in the transverse plane at mid-rapidity for 0-5% p+Pb collisions at $\sqrt{s_{NN}} = 5.02$ TeV. We chose the initialization time of the hydrodynamic medium in p+Pb collisions to be $\tau_0 = 0.6$ fm and the chemical freeze-out temperature is set to $T_c = 0.165$ GeV. In central p+Pb collisions, all the fluid cells reach the freeze-out hyper-surface at ~ 3.6 fm, which is a much shorter time than that for 0-5% Pb+Pb collisions at $\sqrt{s_{NN}} = 2.76$ TeV as shown in Fig. 6.2. The maximum temperature at τ_0, $T_{max}(\tau_0) = 0.357$ GeV, is estimated to be half of the peak temperature in Pb+Pb collisions.

The asymmetric nature of p+Pb collisions is well represented by the pseudorapidity distributions of charged hadron multiplicity, as shown in Fig. 7.5. Note that the negative η

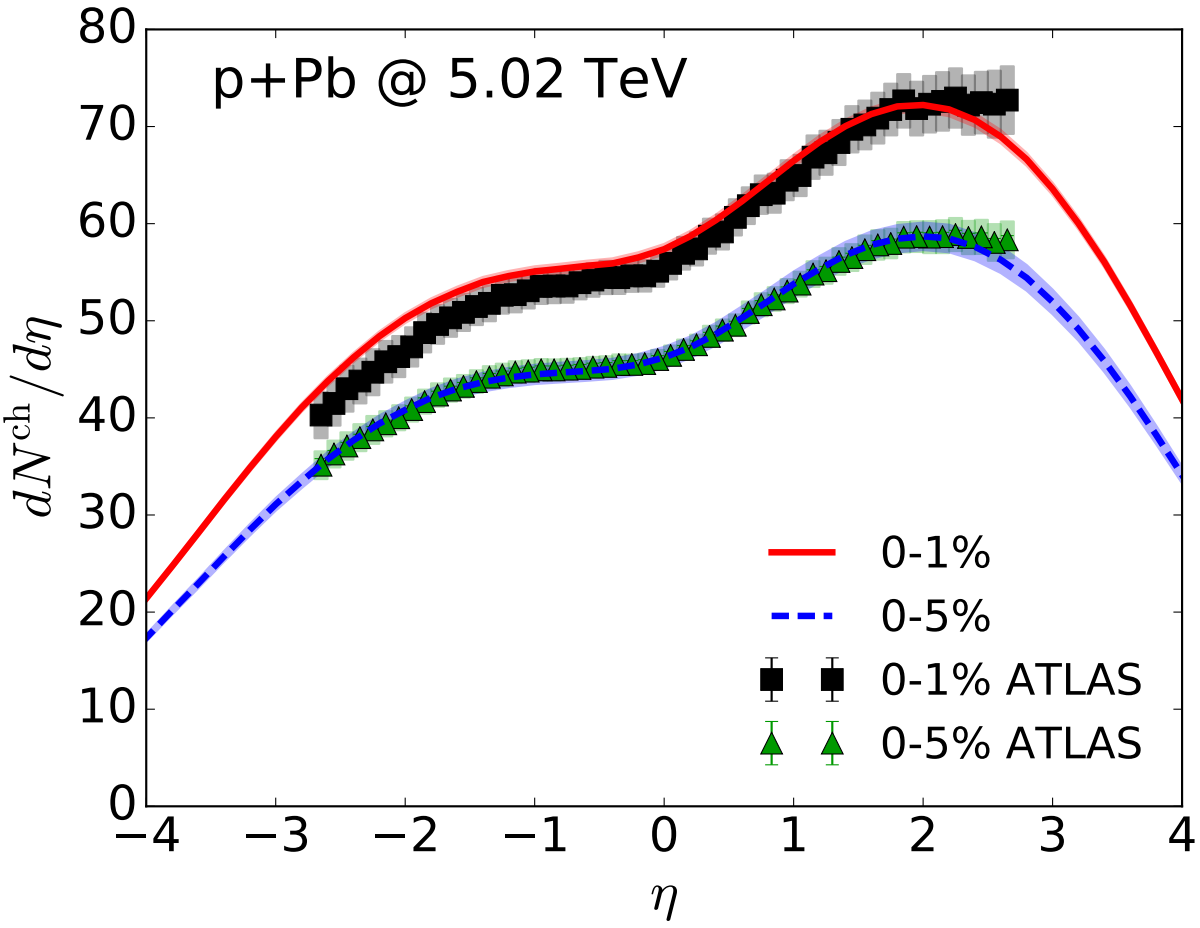

Figure 7.5: Pseudorapidity dependence of charged hadron multiplicity for 0-1% and 0-5% centrality collisions of p+Pb systems at $\sqrt{s_{NN}} = 5.02$ TeV obtained from MUSIC hydrodynamic simulations [4]. We compare our simulation results to the ATLAS measurements for corresponding centrality intervals [263]. Note that the rapidity convention in this plot is opposite to that used in the ATLAS analysis.

in the picture represents the p-going side and the positive η is the Pb-going side, which is opposite to the convention that we use in this analysis. The strong pseudorapidity dependence of final-state charged hadron yields clearly shows a violation of boost-invariance in the region away from the mid-rapidity. The MUSIC hydrodynamic calculations agree fairly well with the ATLAS measurements within a broad range of pseudorapidity intervals.

7.3 Rapidity-dependent jet production

In the previous section, we described the properties of our hydrodynamic simulations by MUSIC for asymmetric p+Pb colliding systems. Using the results of hydrodynamic simulations, we study rapidity-dependent jet production rates in p+Pb collisions. In Sec. 7.1, we discussed the sizable collectivity observed in various small systems and the validity of hydrodynamic modelling. If these small systems also exhibit jet quenching phenomena in the jet production rates, it would constitute robust evidence of the creation of strongly coupled QCD matter. This analysis quantifies the jet modification in small systems to explore signatures of jet quenching in small systems. We used CTEQ6L [113] parton distribution functions and EPS09LO [121] nuclear PDFs for the PDF sampling in our p+Pb study. The convention used in this analysis is that the Pb beam is going in the $-z$ direction and the proton beam is going in the $+z$ direction.

Fig. 7.6 shows the inclusive jet cross-section in minimum bias p+Pb collisions at $\sqrt{s_{NN}} = 5.02$ TeV as a function of jet p_T. The differential jet cross-sections are normalized by the one obtained in the mid-rapidity range, $|\eta| < 1$, to examine the relative jet production rates in the pseudorapidity space. We observed that the p_T differential jet cross-section in p+Pb collisions peaked at mid-rapidity (purple). The jet production rates become lower and narrower as absolute values of rapidity increase. We observed significant reductions in the jet production rates far from mid-rapidity for high jet p_T because of kinematic constraints in those regions. The jet production rates were symmetric in pseudorapidity within slight variations contributed from nuclear PDF effects in Pb nuclei. We obtained good agreement with the CMS measurements [251] across the pseudorapidity intervals.

In Fig. 7.7, we present the ratio between minimum bias p+Pb and pp di-jet production rates as a function of di-jet pseudorapidity, $\eta_{dijet} = (\eta_1 + \eta_2)/2$, at $\sqrt{s_{NN}} = 5.02$ TeV. The four panels correspond to the four different kinematic ranges of average di-jet p_T. We compared the preliminary CMS data to our MARTINI calculations with (dashed green) and without (solid blue) the hydrodynamic medium. Unlike the results in Fig. 7.6

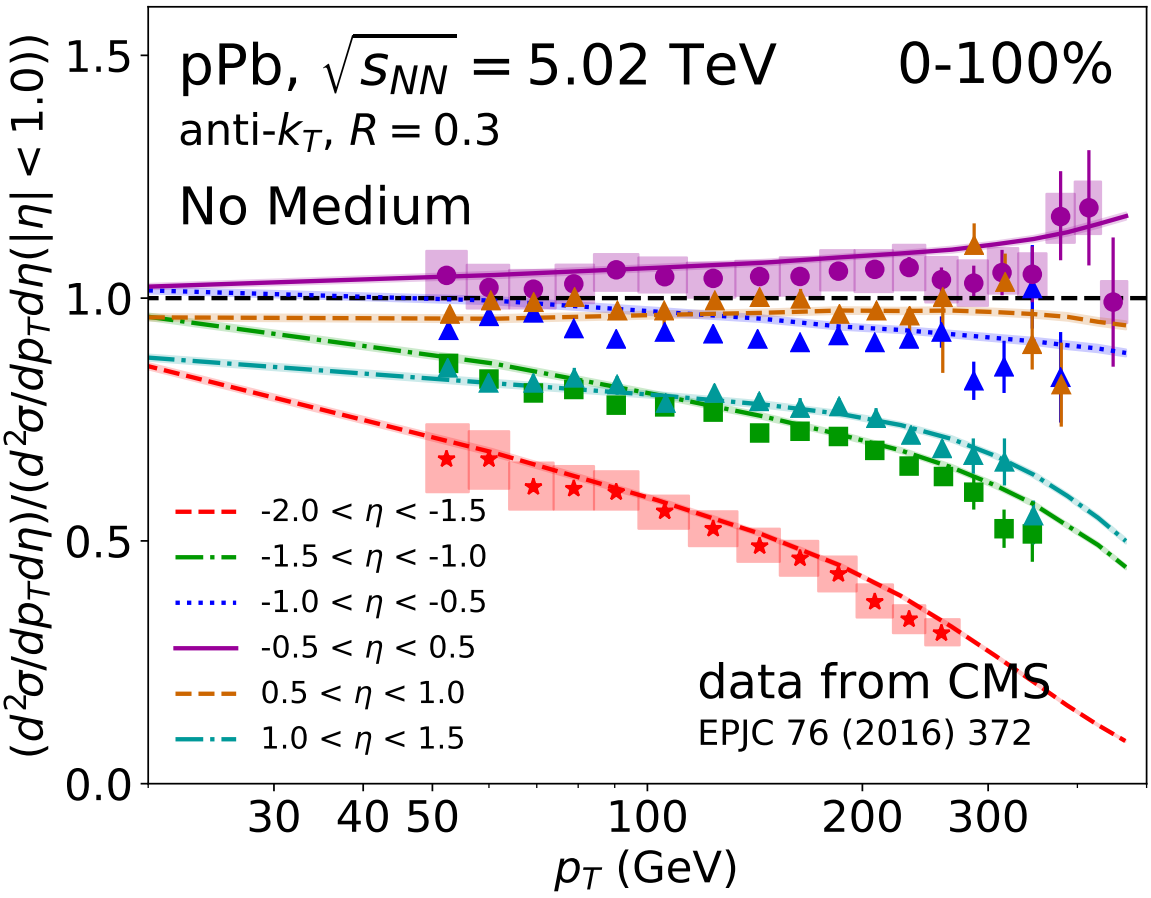

Figure 7.6: The inclusive differential jet cross-section in minimum bias p+Pb collisions at $\sqrt{s_{NN}} = 5.02$ TeV as a function of jet p_T normalized to that at mid-rapidity ($|\eta| < 1$). The shaded bands around the lines indicate the statistical uncertainties. Jets are reconstructed with the anti-k_T algorithm with $R = 0.3$. We present our results corresponding to various pseudorapidity intervals with different colour schemes and compare to the corresponding CMS measurements [251].

where the p+Pb jet production rates are normalized by the one with the same colliding system, the di-jet ratio results in Fig. 7.7 show the anti-shadowing and shadowing effects in pseudorapidity space. We observed the significant shadowing effects at forward di-jet pseudorapidity (p-going side) where the momentum fraction from Pb nuclei x_{Pb} contributing to the initial hard collisions is small. This corresponds to the suppression of R_i^{Pb} at $x_{Pb} \lesssim 0.04$ shown in Fig. 4.7. At backward di-jet pseudorapidity (Pb-going side), we

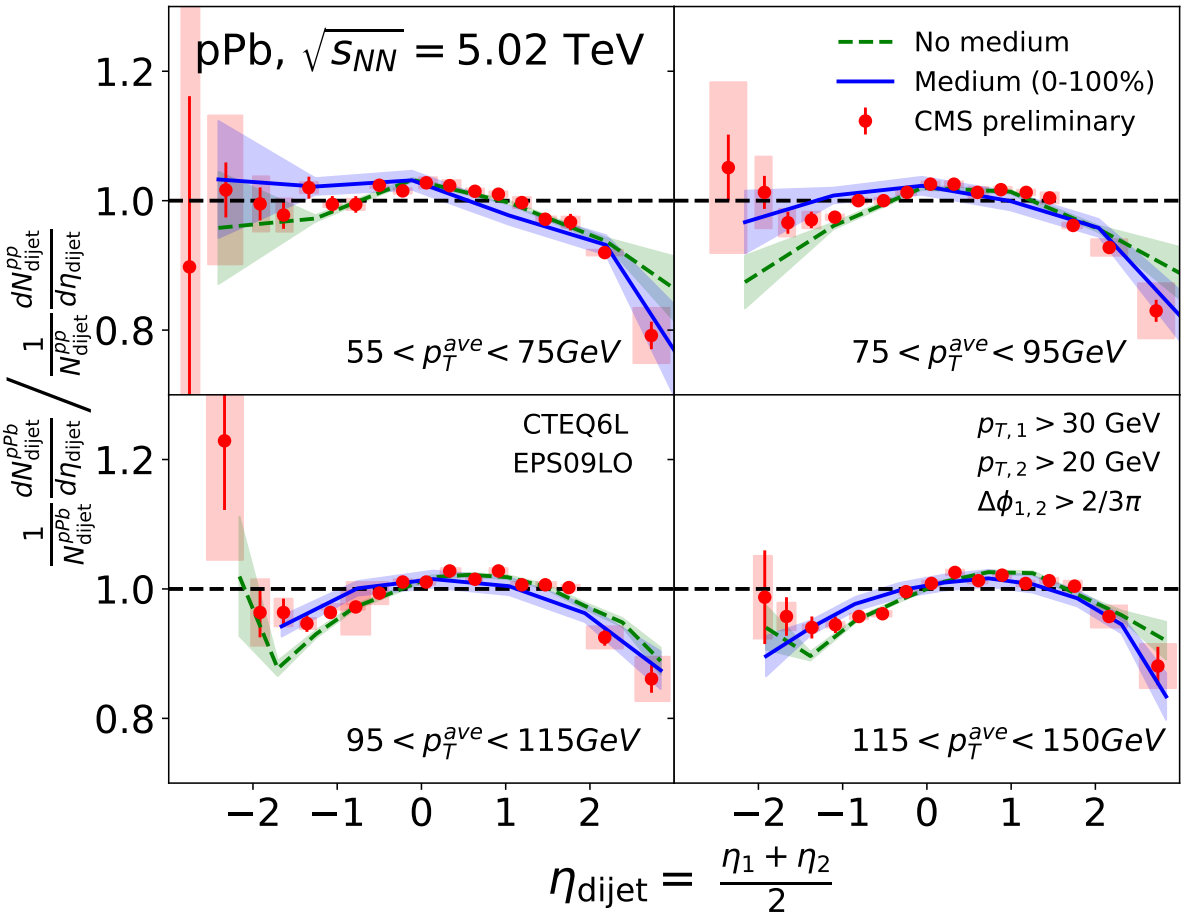

Figure 7.7: The ratio of the di-jet production rates as a function of di-jet pseudorapidity between minimum bias p+Pb and pp collisions at $\sqrt{s_{NN}} = 5.02$ TeV. Each panel shows four different averaged di-jet p_T intervals. MARTINI calculations with (blue solid) and without (green dashed) the hydrodynamic medium are compared to preliminary data from the CMS collaboration [264]. The shaded bands around the lines denote the statistical uncertainties.

observed the EMC effect with large uncertainties caused by the steep decrease of jet production rates that we have observed in Fig. 7.6. We found the peaks of the pseudorapidity distributions in-between those regions with depletion effects. These peaks correspond to the anti-shadowing effects where $0.04 \lesssim x_{Pb} \lesssim 0.2$ and the peak moves to forward di-jet pseudorapidity with the increasing average di-jet p_T as expected from the Fig. 4.7.

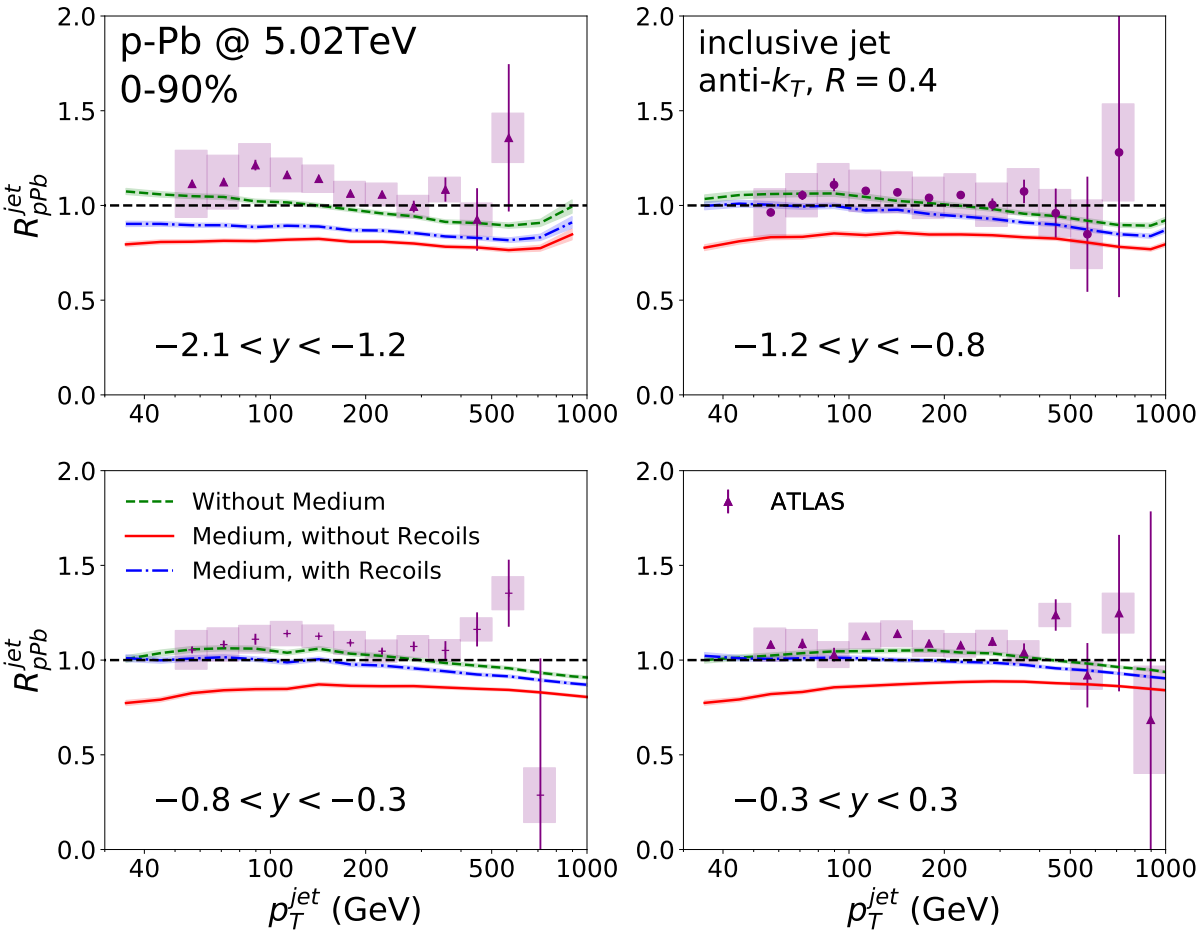

Figure 7.8: Inclusive jet R_{pPb} in 0-90% p+Pb collisions at $\sqrt{s_{NN}} = 5.02$ TeV with recoils and holes (blue) and without them (red). The reconstructed jets are defined by the anti-k_T algorithm with the jet radius parameter of $R = 0.4$. Each panel shows four different rapidity intervals on the Pb-going side. The green lines represent our results without the hydrodynamic medium. We compare MARTINI results to the corresponding ATLAS measurements [244].

The MARTINI results with and without the hydrodynamic medium show slight divergences at forward and backward di-jet pseudorapidity, but the results are statistically indistinguishable. We obtained reasonable agreement between the preliminary CMS data and our MARTINI calculations.

In Fig. 7.8 and Fig. 7.9, we show our R_{pPb} results for 0-90% p+Pb collisions at 5.02 TeV. Each panel shows different rapidity intervals between $-2.1 < y < 2.8$. The green

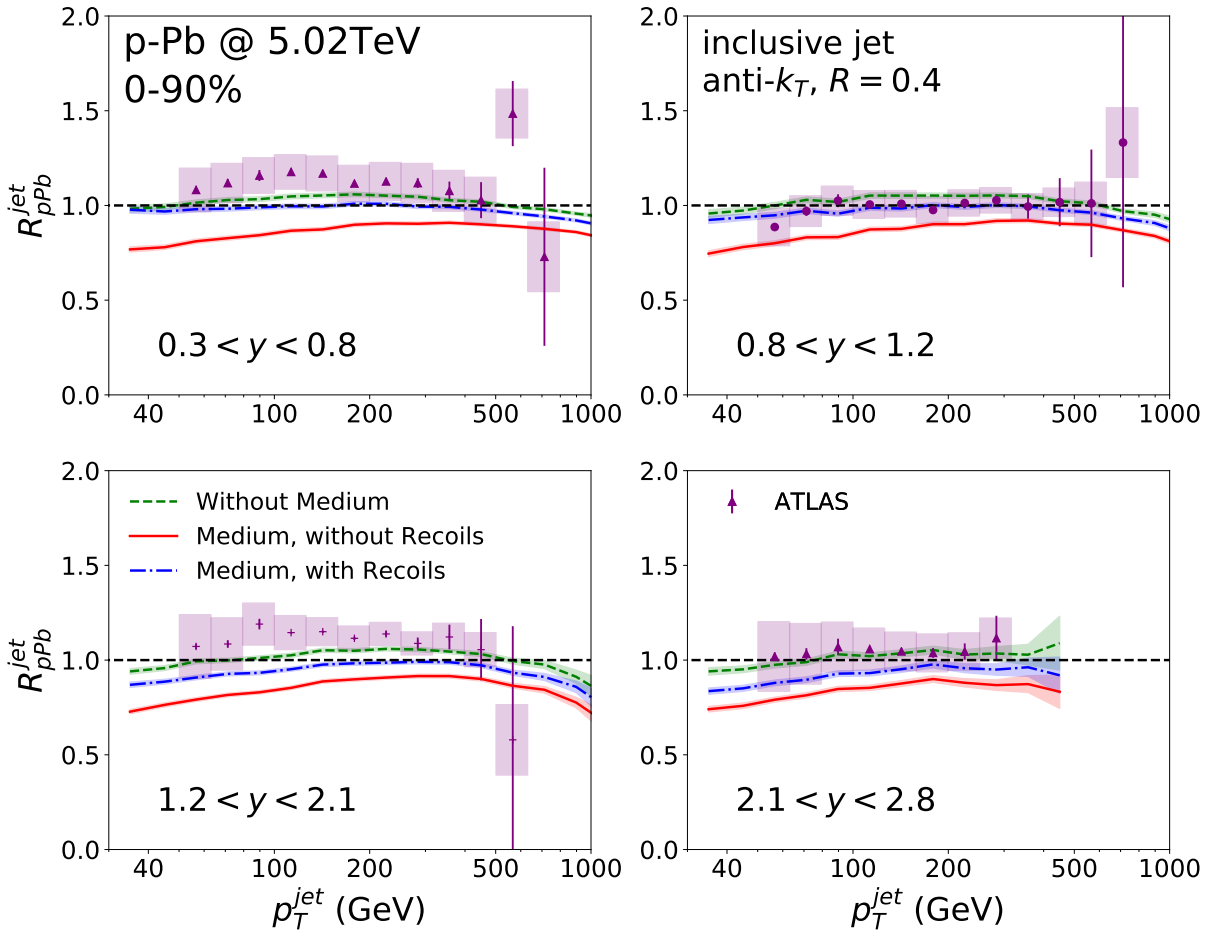

Figure 7.9: Same as Fig. 7.8 with four different rapidity intervals on the p-going side [244].

lines show our result without the hydrodynamic medium, including the nuclear PDF effects, i.e., EPS09LO. We observed slight modification caused by nuclear effects such as shadowing, anti-shadowing, and the EMC effect.

With these results as the baseline, we made comparisons to the scenario with jet quenching. We performed MARTINI simulations with (blue) and without (red) the thermal recoil implementation, as shown in Fig. 7.8 and Fig. 7.9. In small systems, jet modification contributed from radiative processes is expected to be small since the formation time of radiation is comparable to the size of the colliding zone. This implies that jet quenching in p+Pb collisions would be dominated by the elastic processes. Comparing to the baseline calculations (green), the quenching scenario without thermal recoils (red) shows

sizable suppression up to 25%. The suppression was largely recovered when jets contained thermal recoils (blue). This implies that the elastic scattering processes still play a significant role in jet quenching in p+Pb systems. We observed a negligible deviation between the scenario with thermal recoils (blue) and the baseline (green) except in large rapidity regions.

The MARTINI results are compared to the ATLAS measurements. The data shows a slight enhancement from unity, exhibiting no apparent evidence of jet quenching across the rapidity space within the systematic uncertainties. The scenario without jet quenching (green) is favoured by the measurements. The jet R_{pPb}, however, shows a weak discriminating power between the scenarios with and without jet quenching because of negligible medium effects.

Although the measured jet R_{pPb} do not exhibit an obvious signature of jet quenching, they were comparable to the MARTINI results with the jet quenching prescription. This leaves room for a possibility of probing the jet quenching effects in p+Pb collisions. In the next section, we analyze anisotropic harmonic flows of high p_T particles to explore evidence of path-length dependent jet quenching in the small systems.

7.4 Path-length dependent jet quenching

The anisotropic flow coefficients for high p_T particles are a powerful indicator to detect QGP. Jets are produced through binary collisions without preferred initial directions to propagate. In pp collisions, isotropic jet production is preserved, resulting in vanishing harmonic flow coefficients in the final stage. Under the condition that a strongly coupled medium is present, the isotropy of jet production is distorted depending on the length of the medium a jet propagates though. The path-length dependence of jet quenching develops anisotropic flow coefficients v_n for high p_T particles. In Sec. 7.1, we discussed large fluctuations of the initial geometry in p+Au collisions contributing to sizable initial spatial eccentricities. Geometric fluctuations of the colliding zone in small systems have

a high potential to yield non-zero values of v_n for high p_T particles, given that a strongly coupled QCD medium is created in the systems. The hydrodynamic models consistent with the measurements endorse the formation of a QGP as shown in Fig. 7.3.

The analysis of harmonic flow coefficients for high-energy particles explores how a QGP distorts the isotropic jet production during jet evolution. Harmonic flow observables for high p_T particles have several advantages over the nuclear modification factor R_{pA} in search of a signature of QGP in small systems. First, when calculating R_{pA}, one must deal with the normalization factor T_{pA}, which accounts for the number of binary collisions in the corresponding centrality interval of p+A collisions. In theoretical approaches, this can be circumvented by randomly sampling a single binary collision in p+A collisions. However, experimentalists must estimate T_{pA} through the Glauber model [87], which makes it harder to perform a theory-experiment comparison. The anisotropic flow coefficients, however, are purely data-driven observables, which are accessible without further model estimation or requirements of the pp baseline.

Second, R_{pA} is mostly affected by cold nuclear matter and the QGP. The modification of R_{pPb} in small systems is not as prominent as that in large systems and the effect of cold nuclear matter becomes comparable to the jet quenching effect. Given these subtleties of small systems, quantifying the medium effects largely depends on the choice of the nuclear PDFs and their uncertainties. On the other hand, v_n for high-energy particles are driven almost entirely by medium effects because the cold medium effects emerge at the early time of the collisions. These unique features of the anisotropic flow coefficients allow us to differentiate the precise effects of jet quenching from cold nuclear matter effects in search of QGP creation in small systems.

In the analysis of anisotropic flow coefficients contributed from jet particles, we propagated jets through high-multiplicity events of p+Pb collisions. To determine the centrality of the collisions, minimum bias events are sorted according to their initial total entropy density at mid-rapidity. The initial entropy density of the system is a good proxy for centrality determination based on final charged hadron multiplicity [265].

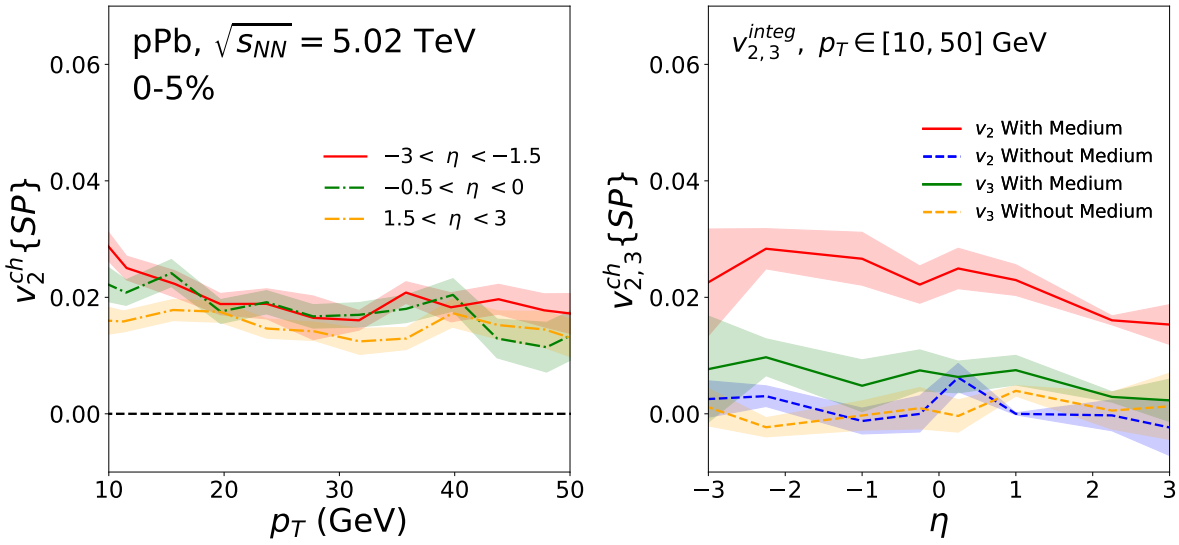

Figure 7.10: (Left panel) p_T distribution of high p_T charged hadron v_2 calculated using the scalar product method [266–268] for 0-5% p+Pb collisions at 5.02 TeV. The v_2 values from the three rapidity intervals are shown up to 50 GeV. The reference flow information is obtained from hydrodynamic simulations. (Right panel) integrated high p_T charged hadron v_2 and v_3 in the rapidity plain. The v_2 and v_3 values are integrated over the p_T range from 10 to 50 GeV compared to our calculations without the medium effects.

The anisotropic flow coefficients of jet particles are calculated using the scalar product method [266–268].

$$v_n(p_T)\{SP\} = \frac{\langle v_n(p_T) v_n^{ref} \cos[n(\phi_n(p_T) - \Psi_n^{ref}]\rangle}{\sqrt{\langle (v_n^{ref})^2 \rangle}}, \tag{7.3}$$

where v_n^{ref} and Ψ_n^{ref} respectively denote the flow coefficients and event plain angle of the reference events. The reference events were constructed from charged hadrons from $p_T = 0.3$ to 3 GeV [4].

The left panel of Fig. 7.10 shows p_T differential charged hadron v_2 for 0-5% central p+Pb collisions at 5.02 TeV at the three different rapidity intervals. We obtained moderately decreasing charged hadron v_2 regardless of the rapidity intervals. We observed 2% of the elliptic flow coefficients for charged hadrons up to 50 GeV. The v_2 and v_3 integrated

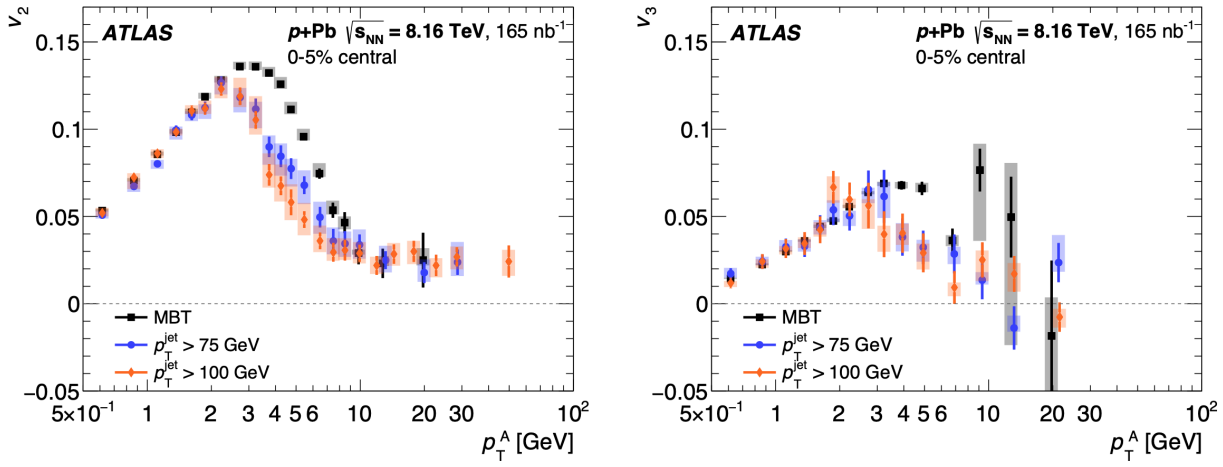

Figure 7.11: Recent v_2 (left panel) and v_3 (right panel) measurements from the ATLAS collaboration for 0-5% central p+Pb collisions at 8.16 TeV. The measurements are obtained using two-particle correlations, measured separately for minimum-bias triggered (MBT) events and events requiring a jet with jet p_T greater than either 75 GeV or 100 GeV [269].

from $p_T = 10$ to 50 GeV as a function of rapidity are shown in the right panel of Fig. 7.10. Those without the hydrodynamic medium are compared to visualize the medium effects from our results. We found vanishing elliptic and triangular flow coefficients when the hydrodynamic background is absent. The non-zero elliptic flow coefficients for high p_T particles became apparent when jet quenching is present. We argue that p+Pb collisions create a strongly coupled QGP with fluctuating shapes, resulting in path-length dependent jet quenching. The values of v_3 with the hydrodynamic medium are less than 1% with larger uncertainties.

Although experimental measurements of v_n for high p_T hadrons are not available at 5.02 TeV, the ATLAS collaboration has performed a similar analysis in p+Pb collisions at higher centre-of-mass energy. Fig. 7.11 shows the measurements of the high p_T hadron v_2 (left panel) and v_3 (right panel) in 0-5% centrality p+Pb collisions at 8.16 TeV. The v_2 measurements show the non-zero values of the elliptic flow coefficients for high p_T hadrons up to 50 GeV within the uncertainty bars. The v_3 values have large fluctuations, approaching zero at $p_T \sim 20$ GeV. We believe that the consistent behaviours of v_2 and v_3 for high-

energy particles at two different centre-of-mass energies serve as meaningful evidence of jet quenching in small systems.

7.5 Summary

In this chapter, we have explored the signatures of QGP creation in small systems such as p+Pb collisions. This work was motivated by the study of azimuthal momentum anisotropies in three different small colliding systems conducted by the RHIC. The key findings from this analysis are i) the initial eccentricities in small systems are driven by the intrinsic geometry and fluctuations in the spatial configuration of each colliding system and ii) the initial eccentricities are highly correlated with the azimuthal momentum anisotropies of the final-state particles. This analysis explained that sizable elliptic flow coefficients in p+Au collisions originate purely from fluctuations in the configurations of colliding nucleons in the Au nuclei, predicting a path-length dependent jet quenching signal. A remarkable agreement of v_n between hydrodynamic models and data justified the reliability of hydrodynamic simulations in studying jet quenching in small systems.

To explore the hint of jet quenching induced by QGP in small systems, we have employed the MARTINI jet evolution scheme, identical to that used in the previous chapter for Pb+Pb collisions. MUSIC, the $3+1$ dimensional viscous hydrodynamic model, simulated the strongly coupled QCD medium in p+Pb collisions event-by-event. The initial conditions for both the positions of produced jets and hydrodynamic simulations were provided by the Glauber model [85–87]. We observed that the QCD medium in p+Pb collisions at 5.02 TeV has a shorter lifetime, less than 4 fm in central cases, and has a lower maximum temperature than that in Pb+Pb collisions. As p+Pb systems are the collisions of two species with different sizes, we found the asymmetric pseudorapidity distributions of charged hadron multiplicity for central p+Pb collisions. Our results show good agreements with the ATLAS measurements in a broad range of pseudorapidity.

In Fig. 7.6, we obtained the maximum inclusive jet cross-section at mid-rapidity, while the jet cross-section decreased at higher absolute values of rapidity. This trend was even stronger at higher jet p_T because of kinematic limitations. However, we did not find a strong asymmetry of the jet production rates in rapidity space in p+Pb collisions. Our results reproduce the CMS measurements well. The nuclear PDF effects are noticeable in the ratio of di-jet production rates between p+Pb and pp collisions as a function of di-jet rapidity. We observed the strong depletion of the ratio at forward rapidity caused by the shadowing effect and the moderate EMC effect at backward rapidity. The anti-shadowing region in mid-rapidity shifted toward forward-rapidity as the di-jet p_T interval increased. While the jet quenching effect slightly modified the ratio, both cases show reasonable agreements with the CMS measurements.

The jet R_{Pbp} calculations with various rapidity intervals show no strong modification in 0-90% p+Pb collisions at 5.02 TeV (Fig. 7.8 and Fig. 7.9). We noticed that thermal recoils still play a critical role in determining the magnitude of the jet R_{pPb}. The medium effects including thermal recoils yielded slight jet quenching, but no convincing evidence of the QGP creation is discovered from the comparison between our results and the data.

The analysis of the path-length dependent jet quenching suggested a hint of the QGP existence in central p+Pb colliding systems. We obtained non-zero charged hadron elliptic flow coefficients from $p_T = 10$ to 50 GeV, which essentially vanish when turning off the medium effects (Fig. 7.10). The azimuthal momentum anisotropies for high p_T particles are driven by different amounts of jet quenching in different jet directions. Because this anisotropic signal is not influenced by the nuclear PDF effects at the jet evolution stage, we believe that this can be a smoking gun of the formation of QGP in small systems. The recent measurements of the harmonic flow coefficients in 0-5% central p+Pb collisions at 8.16 TeV reported similar values of v_2 at high p_T, which reinforces our conclusion of the strongly coupled QCD medium in small systems.

Chapter 8

Conclusion

Jets are 'hard probes', moving quickly and strongly interacting in the QGP. Since the first evidence of heavy-ion-collision jets in 2003 in the STAR and PHENIX experiments, they have been a powerful tool to reveal the properties of the QGP. The study of jet quenching phenomena requires theoretical and experimental efforts from the heavy-ion community. Its quantitative understanding is necessary for the precise characterization of the QGP. The basic methodology to theoretically study jet quenching is to understand the processes through which jets and the QCD medium strongly interact during the jet evolution. In the view of jet quenching models, their interaction can be described in terms of radiative energy loss and collisional energy loss. Several formalisms, developed to describe the jet quenching phenomena, have achieved remarkable successes in contributing to our current understanding of the QGP.

In this dissertation, We have focused on developing an integrated model framework, the MARTINI code package, for precise phenomenological studies of jet quenching. The MARTINI framework encompasses the two energy loss models – the AMY radiative formalism and the leading order elastic scattering rates, both of which are based on high-temperature plasma approximations where the coupling g is weak. The early form of MARTINI already showed promising performance in describing the charged hadron nuclear modification factor R_{AA} at the top RHIC energy.

We implemented an improved treatment of the QCD running coupling constant and the formation time of radiation in the AMY formalism to capture underlying physics emerging at the LHC energy scales. These realistic features effectively reduce jet quenching for higher energy particles due to smaller coupling constant and longer formation time of a radiative process. We also developed an algorithm to simulate thermal recoils and medium response to the jet quenching based on the weakly-coupled approach. Although thermal recoils are mostly soft, they contribute remarkably to the integrated and differential jet observables in small and large colliding systems. The systematic investigations on thermal recoils revealed their importance in describing various jet measurements.

The phenomenological studies of jet quenching in Pb+Pb collisions at 2.76 and 5.02 TeV using the MARTINI framework helped us to understand the mechanism of jet-medium interplay, leading to strong jet modification in heavy-ion collisions. Jet showers consisting of partons experience radiations and elastic scatterings through strong interaction with the medium, but their energies transferred to the medium play an essential role in reconstructing full jet objects in the final state. We obtained simultaneous descriptions of single hadron and jet observables using the MARTINI jet quenching model.

Our attempt to search the QGP in small colliding systems was motivated by the measurements of the elliptic and triangular harmonic flow coefficients at various small systems. We found that the nuclear PDF effects are quantitatively comparable to the medium effects in small systems. The overall jet modification in small systems was found to be negligible and hardly distinguishable by the measurements within their uncertainty. However, the analysis of anisotropic flow coefficients for high p_T particles discovered evidence of path-length dependent jet quenching due to fluctuating-shaped QGP in central p+Pb collisions at 5.02 TeV.

In conclusion, the MARTINI framework, based on perturbative QCD, with hydrodynamic medium obtained by MUSIC allows us to investigate sophisticated mechanisms of jet quenching in heavy-ion collisions. The novel features newly implemented in MARTINI

play an essential role in describing single hadron and jet observables measured at the LHC. Exploration of the model parameters is still a necessary task for improvements to our current results and descriptions of high-precision measurements from future heavy-ion programs. Although numerous experimental measurements can be described by adequate modelling of jet quenching, there is no shortage of exciting adventures to explore in the community of jet physics in heavy-ion collisions.

Bibliography

[1] Bjoern Schenke, Charles Gale, and Sangyong Jeon. MARTINI: An Event generator for relativistic heavy-ion collisions. *Phys. Rev.*, C80:054913, 2009.

[2] Clint Young, Björn Schenke, Sangyong Jeon, and Charles Gale. Realistic modelling of jets in heavy-ion collisions. *Nucl. Phys.*, A910-911:494–497, 2013.

[3] Scott McDonald, Chun Shen, Francois Fillion-Gourdeau, Sangyong Jeon, and Charles Gale. Hydrodynamic predictions for Pb+Pb collisions at 5.02 TeV. *Phys. Rev.*, C95(6):064913, 2017.

[4] Chun Shen, Jean-François Paquet, Gabriel S. Denicol, Sangyong Jeon, and Charles Gale. Collectivity and electromagnetic radiation in small systems. *Phys. Rev. C*, 95(1):014906, 2017.

[5] Matt Crawford and David N. Schramm. Spontaneous Generation of Density Perturbations in the Early Universe. *Nature*, 298:538–540, 1982.

[6] Edward Witten. Cosmic Separation of Phases. *Phys. Rev. D*, 30:272–285, 1984.

[7] J.H. Applegate and C.J. Hogan. Relics of Cosmic Quark Condensation. *Phys. Rev. D*, 31:3037–3045, 1985.

[8] J.H. Applegate, C.J. Hogan, and R.J. Scherrer. Cosmological Baryon Diffusion and Nucleosynthesis. *Phys. Rev. D*, 35:1151–1160, 1987.

[9] Hannu Kurki-Suonio, Richard A. Matzner, Keith A. Olive, and David N. Schramm. Big Bang Nucleosynthesis and the Quark - Hadron Transition. *Astrophys. J.*, 353:406–410, 1990.

[10] G.M. Fuller, G.J. Mathews, and C.R. Alcock. The Quark - Hadron Phase Transition in the Early Universe: Isothermal Baryon Number Fluctuations and Primordial Nucleosynthesis. *Phys. Rev. D*, 37:1380, 1988.

[11] B.S. Meyer, C.R. Alcock, G.J. Mathews, and G.M. Fuller. Spectrum of QCD nucleation site separations and primordial nucleosynthesis. *Phys. Rev. D*, 43:1079–1086, 1991.

[12] Zoltan Fodor. QCD thermodynamics. *PoS*, LATTICE2007:011, 2007.

[13] A. Bazavov et al. Equation of state and QCD transition at finite temperature. *Phys. Rev.*, D80:014504, 2009.

[14] Y. Aoki, S. Borsanyi, S. Durr, Z. Fodor, S. D. Katz, S. Krieg, and K. K. Szabo. QCD transition temperature: Approaching the continuum on the lattice. *Nucl. Phys.*, A830:805C–808C, 2009.

[15] Sourendu Gupta, Xiaofeng Luo, Bedangadas Mohanty, Hans Georg Ritter, and Nu Xu. Scale for the Phase Diagram of Quantum Chromodynamics. *Science*, 332:1525–1528, 2011.

[16] I. Arsene et al. Quark gluon plasma and color glass condensate at RHIC? The Perspective from the BRAHMS experiment. *Nucl. Phys. A*, 757:1–27, 2005.

[17] B.B. Back et al. The PHOBOS perspective on discoveries at RHIC. *Nucl. Phys. A*, 757:28–101, 2005.

[18] John Adams et al. Experimental and theoretical challenges in the search for the quark gluon plasma: The STAR Collaboration's critical assessment of the evidence from RHIC collisions. *Nucl. Phys. A*, 757:102–183, 2005.

[19] K. Adcox et al. Formation of dense partonic matter in relativistic nucleus-nucleus collisions at RHIC: Experimental evaluation by the PHENIX collaboration. *Nucl. Phys. A*, 757:184–283, 2005.

[20] Murray Gell-Mann. A Schematic Model of Baryons and Mesons. *Phys. Lett.*, 8:214–215, 1964.

[21] G. Zweig. An SU(3) model for strong interaction symmetry and its breaking. Version 1. 1964.

[22] G. Zweig. An SU(3) model for strong interaction symmetry and its breaking. Version 2. In D.B. Lichtenberg and Simon Peter Rosen, editors, *DEVELOPMENTS IN THE QUARK THEORY OF HADRONS. VOL. 1. 1964 - 1978*, pages 22–101. 1964.

[23] Ernst Carl Gerlach Stueckelberg de Breidenbach and Andreas Petermann. Normalization of constants in the quanta theory. *Helv. Phys. Acta*, 26:499–520, 1953.

[24] K. Symanzik. Small distance behavior in field theory and power counting. *Commun. Math. Phys.*, 18:227–246, 1970.

[25] Jr. Callan, Curtis G. Broken scale invariance in scalar field theory. *Phys. Rev. D*, 2:1541–1547, 1970.

[26] A. Peterman. Renormalization Group and the Deep Structure of the Proton. *Phys. Rept.*, 53:157, 1979.

[27] David J. Gross and Frank Wilczek. Ultraviolet Behavior of Nonabelian Gauge Theories. *Phys. Rev. Lett.*, 30:1343–1346, 1973.

[28] H.David Politzer. Reliable Perturbative Results for Strong Interactions? *Phys. Rev. Lett.*, 30:1346–1349, 1973.

[29] I.B. Khriplovich. Green's functions in theories with non-abelian gauge group. *Sov. J. Nucl. Phys.*, 10:235–242, 1969.

[30] *Proceedings, Colloquium on Renormalization of Yang-Mills Fields, Marseille, June 19-23, 1972*, 1972.

[31] M. Tanabashi et al. Review of Particle Physics. *Phys. Rev.*, D98(3):030001, 2018.

[32] Roel Aaij et al. Amplitude analysis of $B^+ \to J/\psi\phi K^+$ decays. *Phys. Rev. D*, 95(1):012002, 2017.

[33] Roel Aaij et al. Observation of $J/\psi\phi$ structures consistent with exotic states from amplitude analysis of $B^+ \to J/\psi\phi K^+$ decays. *Phys. Rev. Lett.*, 118(2):022003, 2017.

[34] T. Aaltonen et al. Observation of the $Y(4140)$ Structure in the $J/\psi\phi$ Mass Spectrum in $B^\pm \to J/\psi\phi K^\pm$ Decays. *Mod. Phys. Lett. A*, 32(26):1750139, 2017.

[35] Serguei Chatrchyan et al. Observation of a Peaking Structure in the $J/\psi\phi$ Mass Spectrum from $B^\pm \to J/\psi\phi K^\pm$ Decays. *Phys. Lett. B*, 734:261–281, 2014.

[36] Medina Ablikim et al. Precise measurement of the $e^+e^- \to \pi^+\pi^- J/\psi$ cross section at center-of-mass energies from 3.77 to 4.60 GeV. *Phys. Rev. Lett.*, 118(9):092001, 2017.

[37] Medina Ablikim et al. Evidence of Two Resonant Structures in $e^+e^- \to \pi^+\pi^- h_c$. *Phys. Rev. Lett.*, 118(9):092002, 2017.

[38] K. Chilikin et al. Observation of an alternative $\chi_{c0}(2P)$ candidate in $e^+e^- \to J/\psi D\bar{D}$. *Phys. Rev. D*, 95:112003, 2017.

[39] M. Ablikim et al. Measurement of $e^+e^- \to \pi^+\pi^-\psi(3686)$ from 4.008 to 4.600 GeV and observation of a charged structure in the $\pi^\pm\psi(3686)$ mass spectrum. *Phys. Rev. D*, 96(3):032004, 2017. [Erratum: Phys.Rev.D 99, 019903 (2019)].

[40] Roel Aaij et al. Evidence for an $\eta_c(1S)\pi^-$ resonance in $B^0 \to \eta_c(1S)K^+\pi^-$ decays. *Eur. Phys. J. C*, 78(12):1019, 2018.

[41] J. Cleymans, S. Wheaton, H. Oeschler, and K. Redlich. Comparison of chemical freeze-out criteria in heavy-ion collisions. *PoS*, CPOD2006:035, 2006.

[42] Jonah E. Bernhard, J. Scott Moreland, and Steffen A. Bass. Bayesian estimation of the specific shear and bulk viscosity of quark–gluon plasma. *Nature Phys.*, 15(11):1113–1117, 2019.

[43] Shinji Ejiri. Canonical partition function and finite density phase transition in lattice QCD. *Phys. Rev.*, D78:074507, 2008.

[44] E. Scott Bowman and Joseph I. Kapusta. Critical Points in the Linear Sigma Model with Quarks. *Phys. Rev.*, C79:015202, 2009.

[45] L. Adamczyk et al. Beam Energy Dependence of the Third Harmonic of Azimuthal Correlations in Au+Au Collisions at RHIC. *Phys. Rev. Lett.*, 116(11):112302, 2016.

[46] Grazyna Odyniec. Beam Energy Scan Program at RHIC (BES I and BES II) – Probing QCD Phase Diagram with Heavy-Ion Collisions. *PoS*, CORFU2018:151, 2019.

[47] T. Ablyazimov et al. Challenges in QCD matter physics –The scientific programme of the Compressed Baryonic Matter experiment at FAIR. *Eur. Phys. J. A*, 53(3):60, 2017.

[48] Edward Shuryak. Physics of Strongly coupled Quark-Gluon Plasma. *Prog. Part. Nucl. Phys.*, 62:48–101, 2009.

[49] Szabocls Borsanyi, Zoltan Fodor, Christian Hoelbling, Sandor D. Katz, Stefan Krieg, and Kalman K. Szabo. Full result for the QCD equation of state with 2+1 flavors. *Phys. Lett. B*, 730:99–104, 2014.

[50] A. Bazavov et al. Equation of state in (2+1)-flavor QCD. *Phys. Rev.*, D90:094503, 2014.

[51] Sz. Borsanyi et al. Calculation of the axion mass based on high-temperature lattice quantum chromodynamics. *Nature*, 539(7627):69–71, 2016.

[52] Claudia Ratti. Lattice QCD and heavy ion collisions: a review of recent progress. *Rept. Prog. Phys.*, 81(8):084301, 2018.

[53] Scott Pratt, Evan Sangaline, Paul Sorensen, and Hui Wang. Constraining the Eq. of State of Super-Hadronic Matter from Heavy-Ion Collisions. *Phys. Rev. Lett.*, 114:202301, 2015.

[54] Roger Dashen, Shang-Keng Ma, and Herbert J. Bernstein. S Matrix formulation of statistical mechanics. *Phys. Rev.*, 187:345–370, 1969.

[55] R. Venugopalan and M. Prakash. Thermal properties of interacting hadrons. *Nucl. Phys.*, A546:718–760, 1992.

[56] Elliott D. Bloom et al. High-Energy Inelastic e p Scattering at 6-Degrees and 10-Degrees. *Phys. Rev. Lett.*, 23:930–934, 1969.

[57] Martin Breidenbach, Jerome I. Friedman, Henry W. Kendall, Elliott D. Bloom, D.H. Coward, H.C. DeStaebler, J. Drees, Luke W. Mo, and Richard E. Taylor. Observed Behavior of Highly Inelastic electron-Proton Scattering. *Phys. Rev. Lett.*, 23:935–939, 1969.

[58] W. Albrecht, F.W. Brasse, H. Dorner, W. Flauger, K. Frank, Joerg Gayler, H. Hultschig, J. May, and E. Ganssauge. Inelastic electron proton scattering at high momentum transfers. *Phys. Lett. B*, 28:225–228, 1968.

[59] F.W. Brasse et al. Analysis of photo and electroproduction data against omega(w). *Nucl. Phys. B*, 39:421–431, 1972.

[60] H. Deden et al. Experimental Study of Structure Functions and Sum Rules in Charge Changing Interactions of Neutrinos and anti-neutrinos on Nucleons. *Nucl. Phys. B*, 85:269–288, 1975.

[61] L.W. Whitlow, E.M. Riordan, S. Dasu, Stephen Rock, and A. Bodek. Precise measurements of the proton and deuteron structure functions from a global analysis of

the SLAC deep inelastic electron scattering cross-sections. *Phys. Lett. B*, 282:475–482, 1992.

[62] A.C. Benvenuti et al. A High Statistics Measurement of the Proton Structure Functions F(2) (x, Q**2) and R from Deep Inelastic Muon Scattering at High Q**2. *Phys. Lett. B*, 223:485–489, 1989.

[63] M. Arneodo et al. Measurement of the proton and deuteron structure functions, F2(p) and F2(d), and of the ratio sigma-L / sigma-T. *Nucl. Phys. B*, 483:3–43, 1997.

[64] L.W. Whitlow, Stephen Rock, A. Bodek, E.M. Riordan, and S. Dasu. A Precise extraction of R = sigma-L / sigma-T from a global analysis of the SLAC deep inelastic e p and e d scattering cross-sections. *Phys. Lett. B*, 250:193–198, 1990.

[65] C. Adloff et al. Determination of the longitudinal proton structure function F(L) (x, Q**2) at low x. *Phys. Lett. B*, 393:452–464, 1997.

[66] K. Abe et al. Measurements of R = σ(L) / σ(T) for 0.03 ¡ x ¡ 0.1 and fit to world data. *Phys. Lett. B*, 452:194–200, 1999.

[67] F.D. Aaron et al. Measurement of the Inclusive e$\pm$p Scattering Cross Section at High Inelasticity y and of the Structure Function F_L. *Eur. Phys. J. C*, 71:1579, 2011.

[68] R.P. Feynman. The behavior of hadron collisions at extreme energies. *Conf. Proc. C*, 690905:237–258, 1969.

[69] Richard P. Feynman. Very high-energy collisions of hadrons. *Phys. Rev. Lett.*, 23:1415–1417, 1969.

[70] Guido Altarelli and G. Parisi. Asymptotic Freedom in Parton Language. *Nucl. Phys.*, B126:298–318, 1977.

[71] Yuri L. Dokshitzer. Calculation of the Structure Functions for Deep Inelastic Scattering and e+ e- Annihilation by Perturbation Theory in Quantum Chromodynamics. *Sov. Phys. JETP*, 46:641–653, 1977. [Zh. Eksp. Teor. Fiz.73,1216(1977)].

[72] V. N. Gribov and L. N. Lipatov. Deep inelastic e p scattering in perturbation theory. *Sov. J. Nucl. Phys.*, 15:438–450, 1972. [Yad. Fiz.15,781(1972)].

[73] Michael H. Seymour. Quantum chromodynamics. In *2004 European School of High-Energy Physics*, pages 49–94, 5 2005.

[74] B. Geyer, D. Robaschik, and E. Wieczorek. Theory of Deep Inelastic Lepton-Hadron Scattering. 1. *Fortsch. Phys.*, 27:75, 1979.

[75] Johannes Blumlein and Avtandil Tkabladze. Target mass corrections for polarized structure functions and new sum rules. *Nucl. Phys. B*, 553:427–464, 1999.

[76] M. Tanabashi, K. Hagiwara, K. Hikasa, K. Nakamura, Y. Sumino, F. Takahashi, J. Tanaka, K. Agashe, G. Aielli, C. Amsler, M. Antonelli, D. M. Asner, H. Baer, Sw. Banerjee, R. M. Barnett, T. Basaglia, C. W. Bauer, J. J. Beatty, V. I. Belousov, J. Beringer, S. Bethke, A. Bettini, H. Bichsel, O. Biebel, K. M. Black, E. Blucher, O. Buchmuller, V. Burkert, M. A. Bychkov, R. N. Cahn, M. Carena, A. Ceccucci, A. Cerri, D. Chakraborty, M.-C. Chen, R. S. Chivukula, G. Cowan, O. Dahl, G. D'Ambrosio, T. Damour, D. de Florian, A. de Gouvêa, T. DeGrand, P. de Jong, G. Dissertori, B. A. Dobrescu, M. D'Onofrio, M. Doser, M. Drees, H. K. Dreiner, D. A. Dwyer, P. Eerola, S. Eidelman, J. Ellis, J. Erler, V. V. Ezhela, W. Fetscher, B. D. Fields, R. Firestone, B. Foster, A. Freitas, H. Gallagher, L. Garren, H.-J. Gerber, G. Gerbier, T. Gershon, Y. Gershtein, T. Gherghetta, A. A. Godizov, M. Goodman, C. Grab, A. V. Gritsan, C. Grojean, D. E. Groom, M. Grünewald, A. Gurtu, T. Gutsche, H. E. Haber, C. Hanhart, S. Hashimoto, Y. Hayato, K. G. Hayes, A. Hebecker, S. Heinemeyer, B. Heltsley, J. J. Hernández-Rey, J. Hisano, A. Höcker, J. Holder, A. Holtkamp, T. Hyodo, K. D. Irwin, K. F. Johnson, M. Kado, M. Karliner, U. F. Katz, S. R. Klein, E. Klempt, R. V. Kowalewski, F. Krauss, M. Kreps, B. Krusche, Yu. V. Kuyanov, Y. Kwon, O. Lahav, J. Laiho, J. Lesgourgues, A. Liddle, Z. Ligeti, C.-J. Lin, C. Lippmann, T. M. Liss, L. Littenberg, K. S. Lugovsky, S. B. Lugovsky, A. Lusiani, Y. Makida, F. Maltoni, T. Mannel, A. V. Manohar, W. J. Marciano, A. D. Mar-

tin, A. Masoni, J. Matthews, U.-G. Meißner, D. Milstead, R. E. Mitchell, K. Mönig, P. Molaro, F. Moortgat, M. Moskovic, H. Murayama, M. Narain, P. Nason, S. Navas, M. Neubert, P. Nevski, Y. Nir, K. A. Olive, S. Pagan Griso, J. Parsons, C. Patrignani, J. A. Peacock, M. Pennington, S. T. Petcov, V. A. Petrov, E. Pianori, A. Piepke, A. Pomarol, A. Quadt, J. Rademacker, G. Raffelt, B. N. Ratcliff, P. Richardson, A. Ringwald, S. Roesler, S. Rolli, A. Romaniouk, L. J. Rosenberg, J. L. Rosner, G. Rybka, R. A. Ryutin, C. T. Sachrajda, Y. Sakai, G. P. Salam, S. Sarkar, F. Sauli, O. Schneider, K. Scholberg, A. J. Schwartz, D. Scott, V. Sharma, S. R. Sharpe, T. Shutt, M. Silari, T. Sjöstrand, P. Skands, T. Skwarnicki, J. G. Smith, G. F. Smoot, S. Spanier, H. Spieler, C. Spiering, A. Stahl, S. L. Stone, T. Sumiyoshi, M. J. Syphers, K. Terashi, J. Terning, U. Thoma, R. S. Thorne, L. Tiator, M. Titov, N. P. Tkachenko, N. A. Törnqvist, D. R. Tovey, G. Valencia, R. Van de Water, N. Varelas, G. Venanzoni, L. Verde, M. G. Vincter, P. Vogel, A. Vogt, S. P. Wakely, W. Walkowiak, C. W. Walter, D. Wands, D. R. Ward, M. O. Wascko, G. Weiglein, D. H. Weinberg, E. J. Weinberg, M. White, L. R. Wiencke, S. Willocq, C. G. Wohl, J. Womersley, C. L. Woody, R. L. Workman, W.-M. Yao, G. P. Zeller, O. V. Zenin, R.-Y. Zhu, S.-L. Zhu, F. Zimmermann, P. A. Zyla, J. Anderson, L. Fuller, V. S. Lugovsky, and P. Schaffner. Review of particle physics. *Phys. Rev. D*, 98:030001, Aug 2018.

[77] J.D. Bjorken. Asymptotic Sum Rules at Infinite Momentum. *Phys. Rev.*, 179:1547–1553, 1969.

[78] Richard D. Ball et al. Parton distributions for the LHC Run II. *JHEP*, 04:040, 2015.

[79] Jr. Callan, Curtis G. and David J. Gross. High-energy electroproduction and the constitution of the electric current. *Phys. Rev. Lett.*, 22:156–159, 1969.

[80] David J. Gross and Chris H. Llewellyn Smith. High-energy neutrino - nucleon scattering, current algebra and partons. *Nucl. Phys. B*, 14:337–347, 1969.

[81] C. Chang et al. Observed Deviations from Scale Invariance in High-Energy Muon Scattering. *Phys. Rev. Lett.*, 35:901, 1975.

[82] Mateusz Ploskon. Heavy-ion collisions - hot QCD in a lab. In *14th International Workshop on Hadron Physics (Hadron Physics 2018) Florianopolis, Santa Catarina, Brazil, March 18-23, 2018*, 2018.

[83] Yuri Kharlov. Recent results from ALICE. *PoS*, IHEP-LHC-2011:013, 2011.

[84] CW De Jager. Atom. data nucl. data tabl. 14, 479 (1974). cw de jager, h. de vries and c. de vries. *Atom. Data Nucl. Data Tabl*, 36:495, 1987.

[85] R. J. Glauber. Cross-sections in deuterium at high-energies. *Phys. Rev.*, 100:242–248, 1955.

[86] R. J. Glauber and G. Matthiae. High-energy scattering of protons by nuclei. *Nucl. Phys.*, B21:135–157, 1970.

[87] Michael L. Miller, Klaus Reygers, Stephen J. Sanders, and Peter Steinberg. Glauber modeling in high energy nuclear collisions. *Ann. Rev. Nucl. Part. Sci.*, 57:205–243, 2007.

[88] Kenneth Aamodt et al. Centrality dependence of the charged-particle multiplicity density at mid-rapidity in Pb-Pb collisions at $\sqrt{s_{NN}} = 2.76$ TeV. *Phys. Rev. Lett.*, 106:032301, 2011.

[89] Roman Pasechnik and Michal ˇ Sumbera. Phenomenological Review on Quark–Gluon Plasma: Concepts vs. Observations. *Universe*, 3(1):7, 2017.

[90] Peter Braun-Munzinger and Benjamin Dönigus. Loosely-bound objects produced in nuclear collisions at the LHC. *Nucl. Phys.*, A987:144–201, 2019.

[91] A. K. Chaudhuri. *A short course on Relativistic Heavy Ion Collisions*. IOPP, 2014.

[92] Nicolas Borghini, Phuong Mai Dinh, and Jean-Yves Ollitrault. Flow analysis from multiparticle azimuthal correlations. *Phys. Rev.*, C64:054901, 2001.

[93] K. Aamodt et al. Higher harmonic anisotropic flow measurements of charged particles in Pb-Pb collisions at $\sqrt{s_{NN}}$=2.76 TeV. *Phys. Rev. Lett.*, 107:032301, 2011.

[94] Bjoern Schenke, Sangyong Jeon, and Charles Gale. Anisotropic flow in $\sqrt{s} = 2.76$ TeV Pb+Pb collisions at the LHC. *Phys. Lett.*, B702:59–63, 2011.

[95] L. P. Csernai. *Introduction to relativistic heavy ion collisions*. 1994.

[96] Ramona Vogt. *Ultrarelativistic heavy-ion collisions*. Elsevier, 2007.

[97] K. Yagi, T. Hatsuda, and Y. Miake. Quark-gluon plasma: From big bang to little bang. *Camb. Monogr. Part. Phys. Nucl. Phys. Cosmol.*, 23:1–446, 2005.

[98] Bjorn Schenke, Sangyong Jeon, and Charles Gale. Elliptic and triangular flow in event-by-event (3+1)D viscous hydrodynamics. *Phys. Rev. Lett.*, 106:042301, 2011.

[99] Bjorn Schenke, Sangyong Jeon, and Charles Gale. Higher flow harmonics from (3+1)D event-by-event viscous hydrodynamics. *Phys. Rev.*, C85:024901, 2012.

[100] Bjoern Schenke, Sangyong Jeon, and Charles Gale. (3+1)D hydrodynamic simulation of relativistic heavy-ion collisions. *Phys. Rev.*, C82:014903, 2010.

[101] Huichao Song, Steffen A. Bass, and Ulrich Heinz. Viscous QCD matter in a hybrid hydrodynamic+Boltzmann approach. *Phys. Rev.*, C83:024912, 2011.

[102] Sangwook Ryu, Jean-François Paquet, Chun Shen, Gabriel Denicol, Björn Schenke, Sangyong Jeon, and Charles Gale. Effects of bulk viscosity and hadronic rescattering in heavy ion collisions at energies available at the BNL Relativistic Heavy Ion Collider and at the CERN Large Hadron Collider. *Phys. Rev.*, C97(3):034910, 2018.

[103] Huichao Song, Steffen A. Bass, and Ulrich Heinz. Elliptic flow in 200 A GeV Au+Au collisions and 2.76 A TeV Pb+Pb collisions: insights from viscous hydrodynamics

+ hadron cascade hybrid model. *Phys. Rev.*, C83:054912, 2011. [Erratum: Phys. Rev.C87,no.1,019902(2013)].

[104] Ryan D. Weller and Paul Romatschke. One fluid to rule them all: viscous hydrodynamic description of event-by-event central p+p, p+Pb and Pb+Pb collisions at $\sqrt{s} = 5.02$ TeV. *Phys. Lett.*, B774:351–356, 2017.

[105] HH Thorne, S Chapman, and TG Cowling. The mathematical theory of non-uniform gases. 1952.

[106] Ingo Muller. Zum Paradoxon der Warmeleitungstheorie. *Z. Phys.*, 198:329–344, 1967.

[107] W. Israel. Nonstationary irreversible thermodynamics: A Causal relativistic theory. *Annals Phys.*, 100:310–331, 1976.

[108] W. Israel and J. M. Stewart. Transient relativistic thermodynamics and kinetic theory. *Annals Phys.*, 118:341–372, 1979.

[109] E. Molnar, H. Niemi, and D.H. Rischke. Numerical tests of causal relativistic dissipative fluid dynamics. *Eur. Phys. J. C*, 65:615–635, 2010.

[110] G.S. Denicol, H. Niemi, E. Molnar, and D.H. Rischke. Derivation of transient relativistic fluid dynamics from the Boltzmann equation. *Phys. Rev. D*, 85:114047, 2012. [Erratum: Phys.Rev.D 91, 039902 (2015)].

[111] G.S. Denicol, T. Koide, and D.H. Rischke. Dissipative relativistic fluid dynamics: a new way to derive the equations of motion from kinetic theory. *Phys. Rev. Lett.*, 105:162501, 2010.

[112] B. Jager, A. Schafer, M. Stratmann, and W. Vogelsang. Next-to-leading order QCD corrections to high p(T) pion production in longitudinally polarized pp collisions. *Phys. Rev.*, D67:054005, 2003.

[113] J. Pumplin, D. R. Stump, J. Huston, H. L. Lai, Pavel M. Nadolsky, and W. K. Tung. New generation of parton distributions with uncertainties from global QCD analysis. *JHEP*, 07:012, 2002.

[114] Georges Aad et al. Measurements of the Nuclear Modification Factor for Jets in Pb+Pb Collisions at $\sqrt{s_{\mathrm{NN}}} = 2.76$ TeV with the ATLAS Detector. *Phys. Rev. Lett.*, 114(7):072302, 2015.

[115] Jaroslav Adam et al. Measurement of jet suppression in central Pb-Pb collisions at $\sqrt{s_{\mathrm{NN}}}$ = 2.76 TeV. *Phys. Lett.*, B746:1–14, 2015.

[116] Vardan Khachatryan et al. Measurement of inclusive jet cross sections in pp and PbPb collisions at $\sqrt{s_{NN}} =$ 2.76 TeV. *Phys. Rev.*, C96(1):015202, 2017.

[117] Karen M. Burke et al. Extracting the jet transport coefficient from jet quenching in high-energy heavy-ion collisions. *Phys. Rev.*, C90(1):014909, 2014.

[118] Jiechen Xu, Alessandro Buzzatti, and Miklos Gyulassy. Azimuthal jet flavor tomography with CUJET2.0 of nuclear collisions at RHIC and LHC. *JHEP*, 08:063, 2014.

[119] Shanshan Cao and Abhijit Majumder. Nuclear modification of leading hadrons and jets within a virtuality ordered parton shower. *Phys. Rev.*, C101(2):024903, 2020.

[120] Yayun He, Shanshan Cao, Wei Chen, Tan Luo, Long-Gang Pang, and Xin-Nian Wang. Interplaying mechanisms behind single inclusive jet suppression in heavy-ion collisions. *Phys. Rev.*, C99(5):054911, 2019.

[121] K. J. Eskola, H. Paukkunen, and C. A. Salgado. EPS09: A New Generation of NLO and LO Nuclear Parton Distribution Functions. *JHEP*, 04:065, 2009.

[122] Michele Arneodo. Nuclear effects in structure functions. In *15th International Warsaw Meeting on Elementary Particle Physics: Quest for Links to New Physics Kazimierz, Poland, May 25-29*, pages 412–428. World Scientific, 1992.

[123] Donald F Geesaman, Koichi Saito, and Anthony W Thomas. The nuclear emc effect. *Annual Review of Nuclear and Particle Science*, 45(1):337–390, 1995.

[124] Michele Arneodo. Nuclear effects in structure functions. *Phys. Rept.*, 240:301–393, 1994.

[125] Donald F. Geesaman, K. Saito, and Anthony William Thomas. The nuclear EMC effect. *Ann. Rev. Nucl. Part. Sci.*, 45:337–390, 1995.

[126] P. Amaudruz et al. A Reevaluation of the nuclear structure function ratios for D, He, Li-6, C and Ca. *Nucl. Phys. B*, 441:3–11, 1995.

[127] M. Arneodo et al. The Structure Function ratios F2(li) / F2(D) and F2(C) / F2(D) at small x. *Nucl. Phys. B*, 441:12–30, 1995.

[128] M. Arneodo et al. The A dependence of the nuclear structure function ratios. *Nucl. Phys. B*, 481:3–22, 1996.

[129] M.R. Adams et al. Saturation of shadowing at very low $x_{\rm BJ}$. *Phys. Rev. Lett.*, 68:3266–3269, 1992.

[130] M.R. Adams et al. Shadowing in inelastic scattering of muons on carbon, calcium and lead at low x(Bj). *Z. Phys. C*, 67:403–410, 1995.

[131] R.G. Arnold et al. Measurements of the a-Dependence of Deep Inelastic electron Scattering from Nuclei. *Phys. Rev. Lett.*, 52:727, 1984.

[132] M. Arneodo et al. Shadowing in Deep Inelastic Muon Scattering from Nuclear Targets. *Phys. Lett. B*, 211:493–499, 1988.

[133] M. Arneodo et al. Measurements of the nucleon structure function in the range $0.002 - \mathrm{GeV}^2 < x < 0.17 - \mathrm{GeV}^2$ and $0.2 - GeV^2 < q^2 < 8 - GeV^2$ in deuterium, carbon and calcium. *Nucl. Phys. B*, 333:1–47, 1990.

[134] K. Kovarik et al. nCTEQ15 - Global analysis of nuclear parton distributions with uncertainties in the CTEQ framework. *Phys. Rev.*, D93(8):085037, 2016.

[135] Kari J. Eskola, Petja Paakkinen, Hannu Paukkunen, and Carlos A. Salgado. EPPS16: Nuclear parton distributions with LHC data. *Eur. Phys. J.*, C77(3):163, 2017.

[136] Nestor Armesto. Nuclear shadowing. *J. Phys.*, G32:R367–R394, 2006.

[137] A. Bodek and J.L. Ritchie. Fermi Motion Effects in Deep Inelastic Lepton Scattering from Nuclear Targets. *Phys. Rev. D*, 23:1070, 1981.

[138] A. Bodek and J.L. Ritchie. Further Studies of Fermi Motion Effects in Lepton Scattering from Nuclear Targets. *Phys. Rev. D*, 24:1400, 1981.

[139] J.J. Aubert et al. The ratio of the nucleon structure functions $F2_n$ for iron and deuterium. *Phys. Lett. B*, 123:275–278, 1983.

[140] K. Rith. The Emc Effect - Status and Perspectives. *Z. Phys. C*, 38:317–324, 1988.

[141] P.R. Norton. The EMC effect. *Rept. Prog. Phys.*, 66:1253–1297, 2003.

[142] Leo Stodolsky. Hadron-like behavior of gamma, neutrino nuclear cross-sections. *Phys. Rev. Lett.*, 18:135–137, 1967.

[143] D. Schildknecht. ON SHADOWING IN PHOTOPRODUCTION AND INELASTIC ELECTRON SCATTERING FROM COMPLEX NUCLEI. *Nucl. Phys. B*, 66:398–411, 1973.

[144] Graham Shaw. Shadowing in the Scaling Region. *Phys. Lett. B*, 228:125–128, 1989.

[145] Sergey A. Kulagin, G. Piller, and W. Weise. Shadowing, binding and off-shell effects in nuclear deep inelastic scattering. *Phys. Rev. C*, 50:1154–1169, 1994.

[146] Jan Kwiecinski and Barbara Maria Badelek. Unified Description of Nuclear Shadowing of Virtual Photons. *Phys. Lett. B*, 208:508–512, 1988.

[147] L.L. Frankfurt and M.I. Strikman. Shadowing and Enhancement of Quark Distributions in Nuclei at Small X. *Nucl. Phys. B*, 316:340–354, 1989.

[148] Stanley J. Brodsky and Hung Jung Lu. Shadowing and Antishadowing of Nuclear Structure Functions. *Phys. Rev. Lett.*, 64:1342, 1990.

[149] Nikolai N. Nikolaev and B.G. Zakharov. Color transparency and scaling properties of nuclear shadowing in deep inelastic scattering. *Z. Phys. C*, 49:607–618, 1991.

[150] V. Barone, M. Genovese, Nikolai N. Nikolaev, E. Predazzi, and B.G. Zakharov. Structure functions of bound nucleons: From the EMC effect to nuclear shadowing. *Z. Phys. C*, 58:541–558, 1993.

[151] Boris Kopeliovich and Bogdan Povh. Scaling variable for nuclear shadowing in deep inelastic scattering. *Phys. Lett. B*, 367:329–334, 1996.

[152] N. Armesto and M.A. Braun. The EMC effect at low x in perturbative QCD. *Z. Phys. C*, 76:81–90, 1997.

[153] Zheng Huang, Hung Jung Lu, and Ina Sarcevic. Partonic picture of nuclear shadowing at small x. *Nucl. Phys. A*, 637:79–106, 1998.

[154] N. Armesto. A Simple model for nuclear structure functions at small x in the dipole picture. *Eur. Phys. J. C*, 26:35–43, 2002.

[155] Boris Z. Kopeliovich, Andreas Schafer, and Alexander V. Tarasov. Nonperturbative effects in gluon radiation and photoproduction of quark pairs. *Phys. Rev. D*, 62:054022, 2000.

[156] Boris Z. Kopeliovich, Jorg Raufeisen, and Alexander V. Tarasov. Nuclear shadowing and coherence length for longitudinal and transverse photons. *Phys. Rev. C*, 62:035204, 2000.

[157] J. Nemchik. Nuclear shadowing in DIS: Numerical solution of evolution equation for the green function. *Phys. Rev. C*, 68:035206, 2003.

[158] A. Capella, A. Kaidalov, C. Merino, D. Pertermann, and J. Tran Thanh Van. Structure functions of nuclei at small x and diffraction at HERA. *Eur. Phys. J. C*, 5:111–117, 1998.

[159] L. Frankfurt, V. Guzey, M. McDermott, and M. Strikman. Nuclear shadowing in deep inelastic scattering on nuclei: Leading twist versus eikonal approaches. *JHEP*, 02:027, 2002.

[160] L. Frankfurt, V. Guzey, and M. Strikman. Leading twist nuclear shadowing: Uncertainties, comparison to experiments, and higher twist effects. *Phys. Rev. D*, 71:054001, 2005.

[161] N. Armesto, A. Capella, A.B. Kaidalov, J. Lopez-Albacete, and C.A. Salgado. Nuclear structure functions at small x from inelastic shadowing and diffraction. *Eur. Phys. J. C*, 29:531–540, 2003.

[162] Alfred H. Mueller and Jian-wei Qiu. Gluon Recombination and Shadowing at Small Values of x. *Nucl. Phys. B*, 268:427–452, 1986.

[163] Jian-wei Qiu. Nuclear Shadowing at Small Values of x. *Nucl. Phys. B*, 291:746–764, 1987.

[164] Edmond L. Berger and Jian-wei Qiu. A-dependence in the Shadowing Region of Deep Inelastic Scattering. *Phys. Lett. B*, 206:141–145, 1988.

[165] F.E. Close and R.G. Roberts. A-dependence of Shadowing and the Small X Emc Data. *Phys. Lett. B*, 213:91–94, 1988.

[166] Jian-wei Qiu and Ivan Vitev. Resummed QCD power corrections to nuclear shadowing. *Phys. Rev. Lett.*, 93:262301, 2004.

[167] Paolo Castorina. Nucleon correlations and higher twist effects in nuclear structure functions. *Phys. Rev. D*, 72:097503, 2005.

[168] R. Baier, Yuri L. Dokshitzer, Alfred H. Mueller, S. Peigne, and D. Schiff. Radiative energy loss of high-energy quarks and gluons in a finite volume quark - gluon plasma. *Nucl. Phys.*, B483:291–320, 1997.

[169] R. Baier, Yuri L. Dokshitzer, Alfred H. Mueller, S. Peigne, and D. Schiff. Radiative energy loss and p(T) broadening of high-energy partons in nuclei. *Nucl. Phys.*, B484:265–282, 1997.

[170] B. G. Zakharov. Fully quantum treatment of the Landau-Pomeranchuk-Migdal effect in QED and QCD. *JETP Lett.*, 63:952–957, 1996.

[171] Miklos Gyulassy, Peter Levai, and Ivan Vitev. Jet quenching in thin quark gluon plasmas. 1. Formalism. *Nucl. Phys.*, B571:197–233, 2000.

[172] M. Gyulassy, P. Levai, and I. Vitev. NonAbelian energy loss at finite opacity. *Phys. Rev. Lett.*, 85:5535–5538, 2000.

[173] Magdalena Djordjevic and Ulrich W. Heinz. Radiative energy loss in a finite dynamical QCD medium. *Phys. Rev. Lett.*, 101:022302, 2008.

[174] Urs Achim Wiedemann. Gluon radiation off hard quarks in a nuclear environment: Opacity expansion. *Nucl. Phys.*, B588:303–344, 2000.

[175] Urs Achim Wiedemann. Jet quenching versus jet enhancement: A Quantitative study of the BDMPS-Z gluon radiation spectrum. *Nucl. Phys.*, A690:731–751, 2001.

[176] Xiao-feng Guo and Xin-Nian Wang. Multiple scattering, parton energy loss and modified fragmentation functions in deeply inelastic e A scattering. *Phys. Rev. Lett.*, 85:3591–3594, 2000.

[177] Xin-Nian Wang and Xiao-feng Guo. Multiple parton scattering in nuclei: Parton energy loss. *Nucl. Phys.*, A696:788–832, 2001.

[178] Abhijit Majumder. Hard collinear gluon radiation and multiple scattering in a medium. *Phys. Rev.*, D85:014023, 2012.

[179] Peter Brockway Arnold, Guy D. Moore, and Laurence G. Yaffe. Photon emission from quark gluon plasma: Complete leading order results. *JHEP*, 12:009, 2001.

[180] Peter Brockway Arnold, Guy D. Moore, and Laurence G. Yaffe. Photon emission from ultrarelativistic plasmas. *JHEP*, 11:057, 2001.

[181] Peter Brockway Arnold, Guy D. Moore, and Laurence G. Yaffe. Photon and gluon emission in relativistic plasmas. *JHEP*, 06:030, 2002.

[182] Peter Brockway Arnold, Guy D. Moore, and Laurence G. Yaffe. Effective kinetic theory for high temperature gauge theories. *JHEP*, 01:030, 2003.

[183] M. M. Aggarwal et al. Transverse mass distributions of neutral pions from Pb-208 induced reactions at 158-A-GeV. *Eur. Phys. J.*, C23:225–236, 2002.

[184] David G. d'Enterria. Indications of suppressed high p(T) hadron production in nucleus - nucleus collisions at CERN-SPS. *Phys. Lett.*, B596:32–43, 2004.

[185] Betty Abelev et al. Centrality Dependence of Charged Particle Production at Large Transverse Momentum in Pb–Pb Collisions at $\sqrt{s_{\rm NN}} = 2.76$ TeV. *Phys. Lett.*, B720:52–62, 2013.

[186] Georges Aad et al. Measurement of charged-particle spectra in Pb+Pb collisions at $\sqrt{s_{\rm NN}} = 2.76$ TeV with the ATLAS detector at the LHC. *JHEP*, 09:050, 2015.

[187] Serguei Chatrchyan et al. Study of high-pT charged particle suppression in PbPb compared to pp collisions at $\sqrt{s_{NN}} = 2.76$ TeV. *Eur. Phys. J.*, C72:1945, 2012.

[188] A. Adare et al. Neutral pion production with respect to centrality and reaction plane in Au+Au collisions at $\sqrt{s_{NN}}$=200 GeV. *Phys. Rev.*, C87(3):034911, 2013.

[189] J. Adams et al. Transverse momentum and collision energy dependence of high p(T) hadron suppression in Au+Au collisions at ultrarelativistic energies. *Phys. Rev. Lett.*, 91:172302, 2003.

[190] C. Alt et al. High Transverse Momentum Hadron Spectra at s(NN)**(1/2) = 17.3-GeV, in Pb+Pb and p+p Collisions, Measured by CERN-NA49. *Phys. Rev.*, C77:034906, 2008.

[191] Yang-Ting Chien, Alexander Emerman, Zhong-Bo Kang, Grigory Ovanesyan, and Ivan Vitev. Jet Quenching from QCD Evolution. *Phys. Rev.*, D93(7):074030, 2016.

[192] Jorge Casalderrey-Solana, Doga Can Gulhan, José Guilherme Milhano, Daniel Pablos, and Krishna Rajagopal. A Hybrid Strong/Weak Coupling Approach to Jet Quenching. *JHEP*, 10:019, 2014. [Erratum: JHEP09,175(2015)].

[193] Evan Bianchi, Jacob Elledge, Amit Kumar, Abhijit Majumder, Guang-You Qin, and Chun Shen. The x and Q^2 dependence of $\hat{q}$, quasi-particles and the JET puzzle. 2017.

[194] Jiechen Xu, Jinfeng Liao, and Miklos Gyulassy. Bridging Soft-Hard Transport Properties of Quark-Gluon Plasmas with CUJET3.0. *JHEP*, 02:169, 2016.

[195] Carlota Andrés, Néstor Armesto, Matthew Luzum, Carlos A. Salgado, and Pía Zurita. Energy versus centrality dependence of the jet quenching parameter $\hat{q}$ at RHIC and LHC: a new puzzle? *Eur. Phys. J.*, C76(9):475, 2016.

[196] Jacquelyn Noronha-Hostler, Barbara Betz, Jorge Noronha, and Miklos Gyulassy. Event-by-event hydrodynamics + jet energy loss: A solution to the $R_{AA} \otimes v_2$ puzzle. *Phys. Rev. Lett.*, 116(25):252301, 2016.

[197] Vardan Khachatryan et al. Charged-particle nuclear modification factors in PbPb and pPb collisions at $\sqrt{s_{\mathrm{N\,N}}} = 5.02$ TeV. *JHEP*, 04:039, 2017.

[198] Torbjörn Sjöstrand, Stefan Ask, Jesper R. Christiansen, Richard Corke, Nishita Desai, Philip Ilten, Stephen Mrenna, Stefan Prestel, Christine O. Rasmussen, and Peter Z. Skands. An Introduction to PYTHIA 8.2. *Comput. Phys. Commun.*, 191:159–177, 2015.

[199] Peter Richardson and Alexandra Wilcock. Monte Carlo Simulation of Hard Radiation in Decays in Beyond the Standard Model Physics in Herwig++. *Eur. Phys. J.*, C74:2713, 2014.

[200] Frank E. Paige, Serban D. Proto pescu, Howard Baer, and Xerxes Tata. ISAJET 7.40: A Monte Carlo event generator for p p, anti-p p, and e+ e- reactions. 1998.

[201] Enrico Bothmann et al. Event Generation with Sherpa 2.2. *SciPost Phys.*, 7(3):034, 2019.

[202] Christian Bierlich, Gösta Gustafson, Leif Lönnblad, and Harsh Shah. The Angantyr model for Heavy-Ion Collisions in PYTHIA8. *JHEP*, 10:134, 2018.

[203] Bjoern Schenke, Charles Gale, and Guang-You Qin. The Evolving distribution of hard partons traversing a hot strongly interacting plasma. *Phys. Rev.*, C79:054908, 2009.

[204] L. D. Landau and I. Pomeranchuk. Limits of applicability of the theory of bremsstrahlung electrons and pair production at high-energies. *Dokl. Akad. Nauk Ser. Fiz.*, 92:535–536, 1953.

[205] L. D. Landau and I. Pomeranchuk. Electron cascade process at very high-energies. *Dokl. Akad. Nauk Ser. Fiz.*, 92:735–738, 1953.

[206] A. B. Migdal. Bremsstrahlung and pair production in condensed media at high-energies. *Phys. Rev.*, 103:1811–1820, 1956.

[207] Simon Turbide, Charles Gale, Sangyong Jeon, and Guy D. Moore. Energy loss of leading hadrons and direct photon production in evolving quark-gluon plasma. *Phys. Rev.*, C72:014906, 2005.

[208] Sangyong Jeon and Guy D. Moore. Energy loss of leading partons in a thermal QCD medium. *Phys. Rev.*, C71:034901, 2005.

[209] P. Aurenche, F. Gelis, and H. Zaraket. A Simple sum rule for the thermal gluon spectral function and applications. *JHEP*, 05:043, 2002.

[210] Simon Caron-Huot and Charles Gale. Finite-size effects on the radiative energy loss of a fast parton in hot and dense strongly interacting matter. *Phys. Rev.*, C82:064902, 2010.

[211] Nikolai N. Nikolaev and B. G. Zakharov. The Pomeron in diffractive deep inelastic scattering. *J. Exp. Theor. Phys.*, 78:598–618, 1994. [Zh. Eksp. Teor. Fiz.105,1117(1994)].

[212] Chanwook Park. Jet energy loss with finite-size effects and running coupling in martini. Master's thesis, McGill University, 8 2015.

[213] Eric Braaten and Markus H Thoma. Energy loss of a heavy fermion in a hot qed plasma. *Physical Review D*, 44(4):1298, 1991.

[214] Eric Braaten and Markus H. Thoma. Energy loss of a heavy quark in the quark - gluon plasma. *Phys. Rev. D*, 44(9):2625, 1991.

[215] Eric Braaten and Robert D. Pisarski. Resummation and Gauge Invariance of the Gluon Damping Rate in Hot QCD. *Phys. Rev. Lett.*, 64:1338, 1990.

[216] Eric Braaten and Robert D. Pisarski. Soft Amplitudes in Hot Gauge Theories: A General Analysis. *Nucl. Phys.*, B337:569–634, 1990.

[217] Chanwook Park, Chun Shen, Sangyong Jeon, and Charles Gale. Rapidity-dependent jet energy loss in small systems with finite-size effects and running coupling. *Nucl. Part. Phys. Proc.*, 289-290:289–292, 2017.

[218] Horst Stoecker. Collective flow signals the quark gluon plasma. *Nucl. Phys. A*, 750:121–147, 2005.

[219] J. Casalderrey-Solana, E.V. Shuryak, and D. Teaney. Conical flow induced by quenched QCD jets. *J. Phys. Conf. Ser.*, 27:22–31, 2005.

[220] Jorg Ruppert and Berndt Muller. Waking the colored plasma. *Phys. Lett. B*, 618:123–130, 2005.

[221] L.M. Satarov, Horst Stoecker, and I.N. Mishustin. Mach shocks induced by partonic jets in expanding quark-gluon plasma. *Phys. Lett. B*, 627:64–70, 2005.

[222] Thorsten Renk and Jorg Ruppert. Mach cones in an evolving medium. *Phys. Rev. C*, 73:011901, 2006.

[223] A.K. Chaudhuri. Conical flow due to partonic jets in central Au + Au collisions. *Phys. Rev. C*, 75:057902, 2007.

[224] S. Zhang et al. Transverse momentum and pseudorapidity dependences of 'Mach-like' correlations for central Au + Au collisions at s(NN)**(1/2) = 200-GeV. *Phys. Rev. C*, 76:014904, 2007.

[225] Yayun He, Tan Luo, Xin-Nian Wang, and Yan Zhu. Linear Boltzmann Transport for Jet Propagation in the Quark-Gluon Plasma: Elastic Processes and Medium Recoil. *Phys. Rev. C*, 91:054908, 2015. [Erratum: Phys.Rev.C 97, 019902 (2018)].

[226] Guilherme Milhano, Urs Achim Wiedemann, and Korinna Christine Zapp. Sensitivity of jet substructure to jet-induced medium response. *Phys. Lett. B*, 779:409–413, 2018.

[227] Yasuki Tachibana, Ning-Bo Chang, and Guang-You Qin. Full jet in quark-gluon plasma with hydrodynamic medium response. *Phys. Rev. C*, 95(4):044909, 2017.

[228] Tan Luo, Shanshan Cao, Yayun He, and Xin-Nian Wang. Multiple jets and γ-jet correlation in high-energy heavy-ion collisions. *Phys. Lett. B*, 782:707–716, 2018.

[229] S. Cao et al. Multistage Monte-Carlo simulation of jet modification in a static medium. *Phys. Rev.*, C96(2):024909, 2017.

[230] Matteo Cacciari and Gavin P. Salam. Dispelling the N^3 myth for the k_t jet-finder. *Phys. Lett.*, B641:57–61, 2006.

[231] Matteo Cacciari, Gavin P. Salam, and Gregory Soyez. FastJet User Manual. *Eur. Phys. J.*, C72:1896, 2012.

[232] Pasi Huovinen and Pter Petreczky. QCD Equation of State and Hadron Resonance Gas. *Nucl. Phys.*, A837:26–53, 2010.

[233] Stefano Catani, Bryan R Webber, Yu L Dokshitzer, and Michael H Seymour. Longitudinally-invariant $k_\perp$-clustering algorithms for hadron-hadron collisions. *Nucl. Phys. B*, 406(CERN-TH-6775-93):187–224, 1993.

[234] Stephen D. Ellis and Davison E. Soper. Successive combination jet algorithm for hadron collisions. *Phys. Rev.*, D48:3160–3166, 1993.

[235] Yuri L. Dokshitzer, G. D. Leder, S. Moretti, and B. R. Webber. Better jet clustering algorithms. *JHEP*, 08:001, 1997.

[236] M. Wobisch and T. Wengler. Hadronization corrections to jet cross-sections in deep inelastic scattering. In *Monte Carlo generators for HERA physics. Proceedings, Workshop, Hamburg, Germany, 1998-1999*, pages 270–279, 1998.

[237] Matteo Cacciari, Gavin P. Salam, and Gregory Soyez. The anti-k_t jet clustering algorithm. *JHEP*, 04:063, 2008.

[238] Morad Aaboud et al. Measurement of the nuclear modification factor for inclusive jets in Pb+Pb collisions at $\sqrt{s_{\rm NN}} = 5.02$ TeV with the ATLAS detector. *Phys. Lett.*, B790:108–128, 2019.

[239] Panagiota Foka and Małgorzata Anna Janik. An overview of experimental results from ultra-relativistic heavy-ion collisions at the CERN LHC: Bulk properties and dynamical evolution. *Rev. Phys.*, 1:154–171, 2016.

[240] Serguei Chatrchyan et al. Modification of jet shapes in PbPb collisions at $\sqrt{s_{NN}} = 2.76$ TeV. *Phys. Lett.*, B730:243–263, 2014.

[241] Serguei Chatrchyan et al. Measurement of jet fragmentation into charged particles in pp and PbPb collisions at $\sqrt{s_{NN}} = 2.76$ TeV. *JHEP*, 10:087, 2012.

[242] A. Majumder and J. Putschke. Mass depletion: a new parameter for quantitative jet modification. *Phys. Rev.*, C93(5):054909, 2016.

[243] S. Acharya et al. First measurement of jet mass in Pb–Pb and p–Pb collisions at the LHC. *Phys. Lett.*, B776:249–264, 2018.

[244] Georges Aad et al. Centrality and rapidity dependence of inclusive jet production in $\sqrt{s_{\mathrm{NN}}} = 5.02$ TeV proton-lead collisions with the ATLAS detector. *Phys. Lett. B*, 748:392–413, 2015.

[245] Jaroslav Adam et al. Centrality dependence of particle production in p-Pb collisions at $\sqrt{s_{\mathrm{NN}}}$= 5.02 TeV. *Phys. Rev. C*, 91(6):064905, 2015.

[246] Serguei Chatrchyan et al. Studies of dijet transverse momentum balance and pseudorapidity distributions in pPb collisions at $\sqrt{s_{\mathrm{NN}}} = 5.02$ TeV. *Eur. Phys. J. C*, 74(7):2951, 2014.

[247] Vardan Khachatryan et al. Transverse momentum spectra of inclusive b jets in pPb collisions at $\sqrt{s_{NN}} = 5.02$ TeV. *Phys. Lett. B*, 754:59, 2016.

[248] Jaroslav Adam et al. Measurement of charged jet production cross sections and nuclear modification in p-Pb collisions at $\sqrt{s_{\mathrm{NN}}} = 5.02$ TeV. *Phys. Lett. B*, 749:68–81, 2015.

[249] Georges Aad et al. Transverse momentum, rapidity, and centrality dependence of inclusive charged-particle production in $\sqrt{s_{NN}} = 5.02$ TeV p + Pb collisions measured by the ATLAS experiment. *Phys. Lett. B*, 763:313–336, 2016.

[250] Albert M Sirunyan et al. Measurements of the charm jet cross section and nuclear modification factor in pPb collisions at $\sqrt{s_{NN}}$ = 5.02 TeV. *Phys. Lett. B*, 772:306–329, 2017.

[251] Vardan Khachatryan et al. Measurement of inclusive jet production and nuclear modifications in pPb collisions at $\sqrt{s_{\mathrm{NN}}} = 5.02$ TeV. *Eur. Phys. J. C*, 76(7):372, 2016.

[252] Shreyasi Acharya et al. Constraints on jet quenching in p-Pb collisions at $\sqrt{\mathbf{s_{NN}}}$ = 5.02 TeV measured by the event-activity dependence of semi-inclusive hadron-jet distributions. *Phys. Lett. B*, 783:95–113, 2018.

[253] Shreyasi Acharya et al. Measurement of prompt D^0, D^+, D^{*+}, and $\mathrm{D_S^+}$ production in p–Pb collisions at $\sqrt{\mathrm{s_{NN}}}$ = 5.02 TeV. *JHEP*, 12:092, 2019.

[254] Vardan Khachatryan et al. Evidence for Collective Multiparticle Correlations in p-Pb Collisions. *Phys. Rev. Lett.*, 115(1):012301, 2015.

[255] A. Adare et al. Measurements of elliptic and triangular flow in high-multiplicity ^{3}He+Au collisions at $\sqrt{s_{NN}} = 200$ GeV. *Phys. Rev. Lett.*, 115(14):142301, 2015.

[256] Michael Kordell and Abhijit Majumder. Jets in d(p)-A Collisions: Color Transparency or Energy Conservation. *Phys. Rev. C*, 97(5):054904, 2018.

[257] Serguei Chatrchyan et al. Multiplicity and Transverse Momentum Dependence of Two- and Four-Particle Correlations in pPb and PbPb Collisions. *Phys. Lett. B*, 724:213–240, 2013.

[258] R.S. Bhalerao, N. Borghini, and J.Y. Ollitrault. Analysis of anisotropic flow with Lee-Yang zeroes. *Nucl. Phys. A*, 727:373–426, 2003.

[259] N. Borghini, R.S. Bhalerao, and J.Y. Ollitrault. Anisotropic flow from Lee-Yang zeroes: A Practical guide. *J. Phys. G*, 30:S1213–S1216, 2004.

[260] C. Aidala et al. Creation of quark–gluon plasma droplets with three distinct geometries. *Nature Phys.*, 15(3):214–220, 2019.

[261] M. Habich, J.L. Nagle, and P. Romatschke. Particle spectra and HBT radii for simulated central nuclear collisions of C + C, Al + Al, Cu + Cu, Au + Au, and Pb + Pb from $\sqrt{s} = 62.4$ - 2760 GeV. *Eur. Phys. J. C*, 75(1):15, 2015.

[262] Michael Strickland. Small system studies: A theory overview. *Nucl. Phys. A*, 982:92–98, 2019.

[263] Georges Aad et al. Measurement of the centrality dependence of the charged-particle pseudorapidity distribution in proton–lead collisions at $\sqrt{s_{\mathrm{NN}}} = 5.02$ TeV with the ATLAS detector. *Eur. Phys. J. C*, 76(4):199, 2016.

[264] The CMS Collaboration. Dijet pseudorapidity in pp and pPb collisions at $\sqrt{s_{\mathrm{NN}}} = 5.02\ \mathrm{TeV}$ with the CMS detector. Technical Report CMS-PAS-HIN-16-003, 7 2016.

[265] Chun Shen, Zhi Qiu, and Ulrich Heinz. Shape and flow fluctuations in ultracentral Pb + Pb collisions at the energies available at the CERN Large Hadron Collider. *Phys. Rev. C*, 92(1):014901, 2015.

[266] AM Poskanzer and SA Voloshin. Lbnl annual report http://ie. lbl. gov/nsd1999/rnc. *RNC. htm*, 34, 1998.

[267] C. Adler et al. Elliptic flow from two and four particle correlations in Au+Au collisions at s(NN)**(1/2) = 130-GeV. *Phys. Rev. C*, 66:034904, 2002.

[268] Matthew Luzum and Jean-Yves Ollitrault. Eliminating experimental bias in anisotropic-flow measurements of high-energy nuclear collisions. *Phys. Rev. C*, 87(4):044907, 2013.

[269] Georges Aad et al. Transverse momentum and process dependent azimuthal anisotropies in $\sqrt{s_{\mathrm{NN}}} = 8.16$ TeV p+Pb collisions with the ATLAS detector. *Eur. Phys. J. C*, 80(1):73, 2020.